

Mars is a mirror – Understanding the Pahrump Hills mudstones from a perspective of Earth analogues

JUERGEN SCHIEBER*, KEVIN M. BOHACS†, MAX COLEMAN‡, DAVID BISH§,
MARK H REED¶, LUCY THOMPSON**, WILLIAM RAPIN†† and ZALMAI YAWAR*

*Department of Geological Sciences, Indiana University, 1001 E 10th Str, Bloomington, IN, 47405, USA
(E-mail: jschiebe@indiana.edu)

†KMBohacs GEOconsulting, 10018 Sugar Hill Drive, Houston, TX, 77042, USA

‡NASA Jet Propulsion Laboratory, California Institute of Technology, M/S 300-123G, 4800 Oak Grove Drive, Pasadena, CA, 91109, USA

§Indiana University Molecular Structure Center, 800 E. Kirkwood Ave, Bloomington, IN, 47405, USA

¶Department of Earth Sciences, 1272 University of Oregon, Eugene, OR, 97403, USA

**Department of Earth Sciences, University of New Brunswick, 2 Bailey Dr., Fredericton, NB, E3B5A3, Canada

††IRAP – CNRS, University of Toulouse, 2 avenue du Colonel Roche, BP 44346 31028, Toulouse Cedex 4, France

Associate Editor – Kevin Taylor

ABSTRACT

Mudstone-dominated lacustrine strata in the Pahrump Hills area of Gale Crater, Mars, have the most extensive data set of physical and geochemical observations yet collected. Although sparse by Earth standards, a source-to-sink portrayal of the sedimentary system that differs substantially from previous work has been extracted by integrating sedimentology, stratigraphy, mineral and elemental analyses, geochemical modelling, laboratory experiments and Earth analogues in a sequence-stratigraphic and palaeogeographical framework. Approximately 3.5 Ga, these 15 m thick strata contain five facies that range from fine to coarse detrital mudstone with abundant sediment-incorporative evaporite pseudomorphs. The section is dominated by first-cycle grains of minimally weathered primary igneous minerals but with four distinct compositions. Bedding in the mudstones comprises planar-parallel beds, current ripples and wave-induced structures, with common and widespread truncation. The absence of primary desiccation and synaeresis cracks is probably due to minimal clay-mineral content, as supported by laboratory experiments. Evaporite minerals formed on and within detrital muds shortly after accumulation by evapoconcentration and cooling. The succession contains 16 parasequences in five depositional sequences with all the sequence-stratigraphic elements known from terrestrial strata. Two of the sequence boundaries are unconformities that record significant shifts in the behaviour and palaeogeographical configuration of the fluvio-lacustrine system. This contrasts with the previous view that all facies are genetically related. Most of the variability in rock composition can be attributed to stratigraphic changes in provenance that integrate changing drainage basin configurations, type of exposed bedrock and changes in weathering regime. These strata are interpreted as evaporative lake deposits that accumulated in an underfilled lake basin with closed surface hydrography but through-flowing groundwater. Lake waters were saline to hypersaline, and

lake levels, shorelines and salinities fluctuated greatly at various temporal scales.

Keywords Environmental analysis, evaporite, Gale Crater, geochemistry, Mars, mudstone, provenance, sequence stratigraphy.

... "but there they go, off to Mars, just for the ride, thinking that they will find a planet like a seer's crystal, in which to read a magnificent future. What they will find, instead, is the somewhat shopworn image of themselves. Mars is a mirror, not a crystal."

Ray Bradbury (1950)

INTRODUCTION

Overview

Twenty-seven months after landing on Mars on 6 August 2012, the Curiosity rover (NASA's Mars Science Laboratory mission, MSL) arrived at a mudstone exposure (Pahrump Hills) in the foothills of Aeolis Mons (Mt. Sharp). The exposure comprises *ca* 15 m of a mudstone-dominated section with intercalated lenses of sandstone and a sandstone cap (Figs 1 and 2). The rover collected a detailed record of sedimentary structures and textures, as well as compositional and mineralogical variability (Grotzinger *et al.*, 2015). This study integrates these data from a perspective of processes active in terrestrial lacustrine systems (Gierlowski-Kordesch & Kelts, 1994, 2000; Bohacs *et al.*, 2000; Cohen, 2003).

The Pahrump strata have been interpreted as: (i) evaporitic-lacustrine (Schieber *et al.*, 2015) comparable to the Eocene Green River Formation of the USA (Bradley, 1964; Smith & Carroll, 2015); (ii) a shallow lake that intermittently evaporated to dryness (Kah *et al.*, 2018); or as (iii) down-dip extensions of a fluvial-deltaic system with river-generated hyperpycnal flows (Grotzinger *et al.*, 2015; Stack *et al.*, 2019). Whereas the latter studies envision a freshwater lake depositional setting, the authors of this study consider it an underfilled, generally saline, lake system that records significant variations in lake level and water body salinity.

The environmental setting of the Pahrump Hills strata was constrained by evaluating source area conditions, likely transport systems, processes of sediment accumulation and diagenetic overprints. This study presents an in-depth interpretation of the sedimentary geology of the first extensive mudstone exposure encountered on Mars through systematic re-examination of

data and images, extensive comparison with potential Earth analogues and incorporation of insights from experimental work in mudstone sedimentology.

Geological background

Gale Crater, approximately 150 km in diameter, is located slightly south of the Martian equator (Fig. 1) and contains a central mound (Aeolis Mons) that exposes about 5.5 km of sedimentary rocks (Malin & Edgett, 2000). The studied strata occur at the base of this mound and as such must have been buried under several kilometres of overburden before being re-exposed. The crater-forming impact occurred during the Late Noachian or Early Hesperian (3.6 to 3.8 Bya; Thomson *et al.*, 2011; Le Deit *et al.*, 2013). Sediment accumulation in the crater commenced shortly thereafter, extended through most of the Hesperian and possibly into the Early Amazonian (Grant *et al.*, 2014; Palucis *et al.*, 2014). Sediment accumulation was interrupted multiple times by erosive interludes (Malin & Edgett, 2000; Anderson & Bell III, 2010; Milliken *et al.*, 2010), some driven by aeolian processes that are still active today (Day & Kocurek, 2016; Ewing *et al.*, 2017; Schieber *et al.*, 2020). Sedimentary rocks of the crater plains (Fig. 1), assigned to the Bradbury group, are interstratified mudstones, sandstones and conglomerates (Fig. 2) interpreted as fluvial to deltaic sediments with finer grained lacustrine intercalations (e.g. Williams *et al.*, 2013; Grotzinger *et al.*, 2015; Schieber *et al.*, 2017; Edgar *et al.*, 2018).

Pahrump Hills is a continuous mudstone-dominated exposure of lowermost Mt. Sharp strata and has been assigned to the Murray formation (Fig. 2), whose members are differentiated on the basis of differences in composition and sedimentary facies (e.g. Fedo *et al.*, 2018).

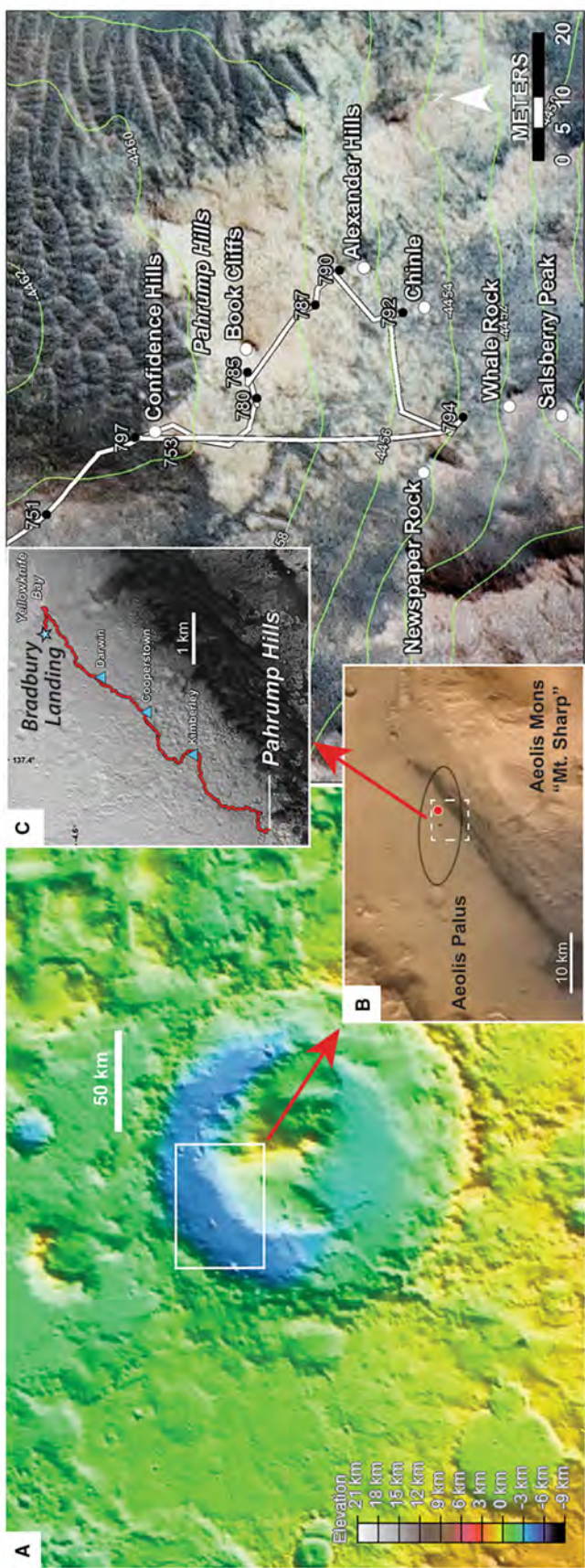


Fig. 1. Gale Crater locations and rover track at Pahrump (north at top of each image). (A) Elevation map of Gale Crater. White rectangle is the location of the enlarged inset (B). (B) Inset shows the landing site (red dot). Aeolis Palus is the name for the low-relief crater floor area, and Aeolis Mons (informally called Mt. Sharp) is the central mound of strata in the crater. The white dashed rectangle is the location of inset (C). Inset (C) shows the rover traverse from the landing site (Bradbury Landing), key study sites along the traverse and location of the Pahrump Hills outcrop. The right half of the figure shows an orbital view of the Pahrump area with an overlay of the first reconnaissance rover track and landmarks mentioned in the manuscript. Black dots are rover locations with arrival Sol (for example, 751 means that the rover arrived there at Sol 751), white dots are landmarks mentioned in the text and other figures. Green lines are 2 m contour lines. (Credit for component images: NASA/JPL/GSFC/Arizona State University.)

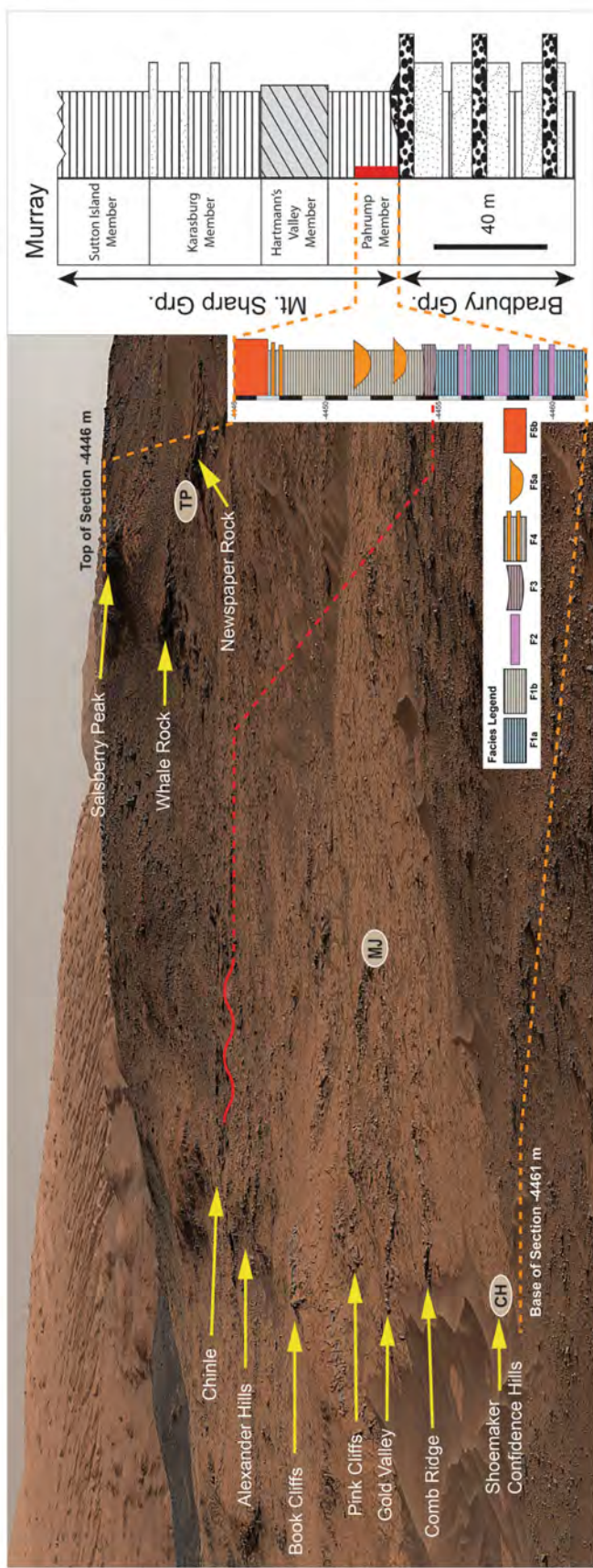


Fig. 2. Overview image of Pahrump Hills outcrop (ML_mciam03229, taken from the Sol 751 vantage point, Fig. 1). Yellow arrows indicate geological features described and discussed in the text. Oval markers show the approximate location of drill holes Confidence Hills (CH), Mojave (M) and Telegraph Peak (TP). The orange dashed lines show the bottom and top of the exposure and relate this 15 m stratigraphic interval to a generalized partial stratigraphic column of Gale Crater (at right). The red wavy line marks an erosional surface designated as the Chinle unconformity. The Pahrump Hills strata represent the lowermost Murray formation and the base of the Mt. Sharp Group; they are thought to overlie the interbedded mudstones, sandstones and conglomerates of the Bradbury group (Groizinger et al., 2015).

Table 1. Instruments on Curiosity rover used in this study.

Instrument	Category	Attributes (resolution/detection limits)	Main use	Limitations
M100 MastCam (right Mast Camera, MR)	Visual	Image size: 1600 × 1200 pixels; image resolution: 148 µm pixel ⁻¹ at 2 m distance, 7.7 cm pixel ⁻¹ at 1 km	Geomorphology, stratigraphy, sedimentology	Discontinuous coverage; limited points of view
M34 MastCam (left Mast Camera, ML)	Visual	Image size: 1600 × 1200 pixels; image resolution: 444 µm pixel ⁻¹ at 2 m distance, 22 cm pixel ⁻¹ at 1 km	Geomorphology, stratigraphy, sedimentology	Discontinuous coverage; limited points of view
MARDI (Mars Descent Imager)	Visual	Image size: 1600 × 1200 pixels; image resolution: ca 1.5 mm pixel ⁻¹	Stratigraphy, sedimentology	Nadir pointing
MAHLI (Mars Hand Lens Imager)	Visual	Image size: 1600 × 1200 pixels; best case image resolution: 15 µm pixel ⁻¹	Sedimentology, grain size	Targets ≤2.5 m of rover; practical resolution limit is ca 20 µm
CheMin (Chemistry and Mineralogy)	Mineral	X-ray diffraction and fluorescence instrument; detection limits dependent on counting statistics	Mineralogy, contact instrument	Powdered sample; up to 10 h analysis time, multiple Sols
APXS (Alpha Particle X-Ray Spectrometer)	Chemical	Sampled area ca 1.7 cm diameter; 10 min suffice for a quick look at major elements, up to 3 h required for all elements	Bulk rock major and trace element composition; contact instrument	Measurements take 2 to 3 h to show all elements, including small amounts of trace elements
ChemCam (Chemistry and Camera)	Chemical	Laser-induced breakdown spectrometer (LIBS), remote micro-imager; target size <1 mm	Chemical composition	Targets within ca 3 to 4 m of rover

At Pahrump, the combination of an excellent exposure with multiple rover traverses (534 m cumulative travel distance), high density of image and analytical data, as well as observations made during the approach to Pahrump, provide a unique opportunity for in-depth investigation of Martian mudstone sedimentology. The nadir pointing Mars Descent Imager (MARDI) camera collected photographic logs of the lower 9 m of the outcrop in ‘sidewalk’ mode (Minitti *et al.*, 2019), confirming that rock characteristics can be traced laterally (Minitti *et al.*, 2019), and that more erosion resistant rocks are laterally extensive horizons with enhanced cementation (Yawar *et al.*, 2018). To date, Pahrump Hills is the best location along the Curiosity traverse to assemble a stratigraphic column approaching ‘Earth standards’.

Approaches taken

‘Rover geology’ differs from Earth-based field geology because even simple tasks require elaborate planning and ‘cost’ much more time (Schieber *et al.*, 2017). At Pahrump, a mere 15 m of strata were examined over a 60 m by 80 m area for a total of 206 Earth days. For a geologist on Earth, a day or two would have sufficed to collect a comparable (or better) data set. A further drawback of rover geology is that there rarely are ‘second chances’ – once the rover leaves a site, additional data cannot be collected.

A range of imaging and analytical instruments provided the information and are listed in Table 1. Mineral compositions were measured directly and also inferred from chemical analyses, then related to provenance, weathering,

Table 2. CheMin mineral abundances, wt. %, (standard deviation).

	Mineralogy, normalized Confidence Hills CH	Mineralogy, normalized Mojave MJ	Mineralogy, normalized Telegraph Peak TP
ΣPlagioclase	24	25	23
Andesine	20 (2)	22 (1)	20 (2)
Oligoclase	4 (2)	2.8 (4)	
Albite			3 (1)
Anorthoclase			7 (3)
Sanidine	4.0 (4)		
Forsterite	1.5 (4)	1.6 (4)	2.1 (7)
Augite	7.0 (6)	2.7 (5)	0.0
Hedenbergite			1.6 (6)
Pigeonite	5.4 (7)	3.4 (6)	6 (1)
Orthopyroxene	1.8 (7)		
Maghemite	3.7 (3)	4.2 (3)	9 (1)
Haematite	7.3 (5)	3.5 (2)	1.3 (4)
Quartz	0.4 (1)	0.5 (1)	0.5 (3)
Cristobalite			8 (1)
Tridymite			1 (1)
Opal-CT	1.8 (6)	2.1 (9)	1.4 (7)
Kerolite	2.4 (5)	0.8 (4)	2.7 (4)
Phyllo/smectite	1.5 (6)	2.6 (9)	
Apatite		1.2 (2)	0.5 (5)
Anhydrite	0.4 (1)		0.8 (2)
Bassanite			0.1 (1)
Gypsum			0.3 (2)
Ilmenite	1.2 (3)		
Parabutlerite		0.6 (1)	0.3 (2)
Rozenite	0.2 (2)		
Jarosite	0.9 (2)	2.6 (3)	1.2 (4)
Pyrite	0.5 (2)	1.4 (3)	0.5 (3)
Shortite	0.5 (2)		1.1 (6)
Thenardite			0.7 (5)
Kieserite	0.4 (2)	0.2 (2)	0.2 (3)
SO ₃ (wt. %)*	4.9	6.3	2.5
Amorphous	36	48	31

Amorphous concentration corrected for phyllo + opal-CT, *APXS SO₃ concentrations. Lithologies of Drill Samples: Confidence Hills = F1a, Mojave = F2, Telegraph Peak = F1b. Blank field = not detected.

transport, deposition and diagenesis. Ideally, CheMin (Chemistry and Mineralogy) compositions (Table 2) would be compared with potential source rocks. Whereas mineral analyses of likely basalt sources are not available, fortuitously encountered igneous float rocks were examined for texture and composition by ChemCam (Chemistry and Camera; Cousin *et al.*, 2017). Geochemical modelling was an important tool because it supported a number of crucial observations and provided a thermodynamically constrained understanding of likely processes, thereby rounding out the conception of the full development of the Pahrump sediments as they are now found. It served as an alternative for deciphering authigenic and paragenetic factors

usually worked out with thin-section examination and analyses.

Having inputs from multiple instruments and geoscience disciplines requires an iterative approach to the evaluation of data sets. The underlying process of discovery, hypothesis testing, reconciliation and iteration is summarized in Fig. 3, a flow chart of the process.

METHODS

Physical attributes

Observations of physical attributes (grain size, bedding, sedimentary structures, stratigraphy

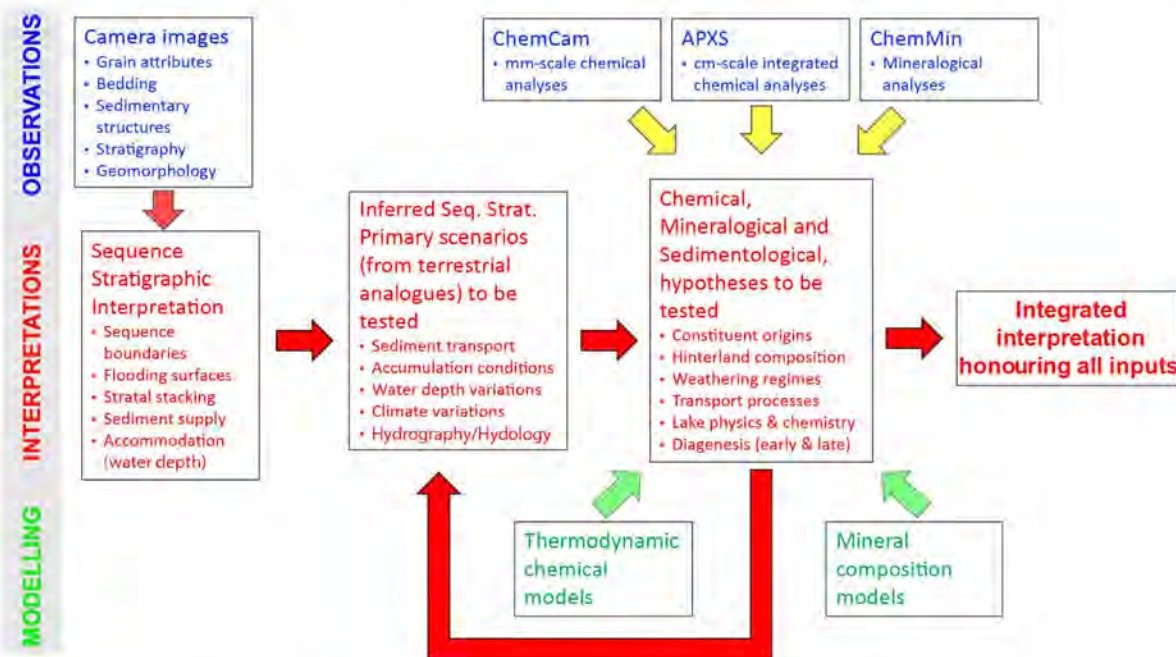


Fig. 3. Research plan and workflow adopted for this study.

and geomorphology) relied mainly on the left Mast Camera (M34 MastCam), right Mast Camera (M100 MastCam), Mars Descent Imager (MARDI) and Mars Hand Lens Imager (MAHLI) cameras (Table 1). Source information for the images in the various figures is listed in Appendix S1.

Compositional attributes were collected by the CheMin, Alpha Particle X-Ray Spectrometer (APXS) and ChemCam instruments (Table 1). The rover carries a stainless-steel-bristle rotary brush (Dust Removal Tool or DRT; Davis *et al.*, 2012) to remove dust and loose sediment. DRT interactions with the rock surface also serve as an indication of bedrock hardness. The areal coverage of analyses varies by instrument (Table 1). CheMin, APXS and DRT are ‘contact’ tools. They require the target to be ≤ 2.5 m from the rover and analyses cluster around areas where the rover remained stationary for multiple days. ChemCam can analyse targets up to *ca* 4 m from the rover and thus has better vertical data coverage.

It was not the objective of the initial rover investigation to conduct a systematic stratigraphic investigation of the geochemistry of these rocks, so data collected at Pahrump Hills is a punctuated and irregular spaced set of geochemical analyses that is quite sparse relative to the scale of variation of the rocks. Even without the added complication of surface dust that negatively affects the accuracy of analyses (Thompson

et al., 2020), on Earth such a data set would be considered subpar for the detection of the vertical geochemical trends that are inherent to the depositional model presented here. Nonetheless, a concerted effort was made, aided by judicious integration of independent data sets, to parse the data according to the character of the analysed exposure, with the aim to ‘see through’ to the original depositional character of these rocks.

Capabilities and operations of cameras and instruments have been described in other MSL publications, and the reader is referred to those publications and references therein for further information (e.g. Maurice *et al.*, 2012; Wiens *et al.*, 2012; Gellert *et al.*, 2015; Schieber *et al.*, 2017; Minitti *et al.*, 2019; Thompson *et al.*, 2020). Appendix S2A provides further information on specific technical issues, including grain size and layer thickness. Rock and bedding nomenclature follows Lazar *et al.* (2015): ‘mudstone’ and ‘sandstone’ are defined strictly on grain size; laminae and beds are defined by stratal geometry, not arbitrary thickness.

Method for comparing CheMin mineral data with those calculated from chemical analyses

Idealized mineral compositions were calculated as CIPW normative mineral proportions from chemical analyses (Cross *et al.*, 1902).

Calculations for each separate analysis in selected groups, as classified by Cousin *et al.* (2017), gave mineral abundance uncertainties.

The objectives for making these mineralogical comparisons were: (i) to identify the provenance of the components of the different sediments; and (ii) to assess the extent of weathering that the parent material experienced *in situ* and possibly also during transport (more detail in Appendix S2B). This approach offered identification of likely basalt sources and a measure of the kinetically-controlled loss of olivine and extent of weathering.

Geochemical modelling methods

Evaporite crystal casts in Pahrump mudstones suggest intermittent evaporation in the lake basin (Schieber *et al.*, 2015; Kah *et al.*, 2018). Methods for computational modelling of dissolved components entering the lake and evaporite accumulation using the CHIM-XPT program are detailed in Appendix S2A.

Integrative method

This investigation includes comprehensive review of all available images (Fig. 3), stepwise integration of fundamental lamina-scale features (millimetres to centimetres) with rover location-scale (decimetres to metres) observations and the outcrop characteristics as seen tens of metres to the left and right of the rover traverse (Fig. 4; Appendix S3). This facilitated a comprehensive view of the exposed strata across the lamina to depositional sequence continuum. Because compositional data (CheMin, APXS and ChemCam) are integrated with the analysis of sediment origins and what happened to them as they were deposited in the lake, an overview of compositional data and their implications is provided prior to describing and discussing physical sedimentary aspects.

COMPOSITIONAL DATA AND INFERENCES

This section summarizes compositional data from the CheMin, ChemCam and APXS instruments (additional detail can be found in Appendix S2B). CheMin X-ray diffraction (XRD) data for Pahrump come from three sites (Fig. 2; Table 2), Confidence Hills (CH; -4460.5 m), Mojave (MJ; -4459.4 m) and Telegraph Peak

(TP; -4453 m). All analyses show a significant proportion of amorphous material (Table 2). Figure 5 shows a subset of the APXS data (Thompson *et al.*, 2020; Appendix S4 contains full data set and details). ChemCam data are shown in Figs 6 and 7.

ChemCam and APXS analysed multiple bedrock targets of mudstone and sandstone, and analyses were grouped into four categories: below, at and above Chinle (Figs 2 and 5) as well as targets acquired on float from the Whale Rock and Salsberry Peak sandstones. In the interval below Chinle, ChemCam and APXS also analysed diagenetic features, such as dendrites (VanBommel *et al.*, 2016), concretions and erosion-resistant bedrock ridges. The compositional diversity of bedrock compositions is illustrated with bivariate and stratigraphic plots (Figs 5 to 7).

Mineral components

Table 2 shows CheMin results and estimated standard deviations for the samples drilled at Pahrump (normalized to 100% after inclusion of amorphous component). Minor and occasionally significant differences exist between this analysis and the results by Rampe *et al.* (2017, 2020). Differences include interpretations of the occurrences of silica phases, phyllosilicates and Ca-sulphate minerals, among others, as discussed below (additional details on mineral identification can be found in Appendix S2B).

Feldspars are the most abundant and mafic minerals the second most abundant mineral group and comprise 33 to 44 wt. % of the crystalline materials. All CheMin samples contain haematite and maghemite (rather than magnetite), ranging from 7.7 to 11.0 wt. %. The maghemite shows 40 to 50% oxidation towards end-member maghemite based on refined unit-cell parameters. Use of a crystal structure with maghemite stoichiometry rather than end-member magnetite significantly improved the fit, lending further credence to the identification of maghemite.

All CheMin samples contain quartz and opal-CT at *ca* 0.4% and *ca* 2.0%, respectively (Table 2). Telegraph Peak also contained cristobalite and possibly tridymite. In contrast, Rampe *et al.* (2020) reported an absence of opal-CT, tridymite and cristobalite in CH and MJ. The differences between observed and model diffraction scans, however, support the presence of *ca* 2% opal-CT at CH and at MJ. Rampe *et al.* (2020) reported the presence of opal-CT and cristobalite in TP. Re-evaluation of the data confirms that the

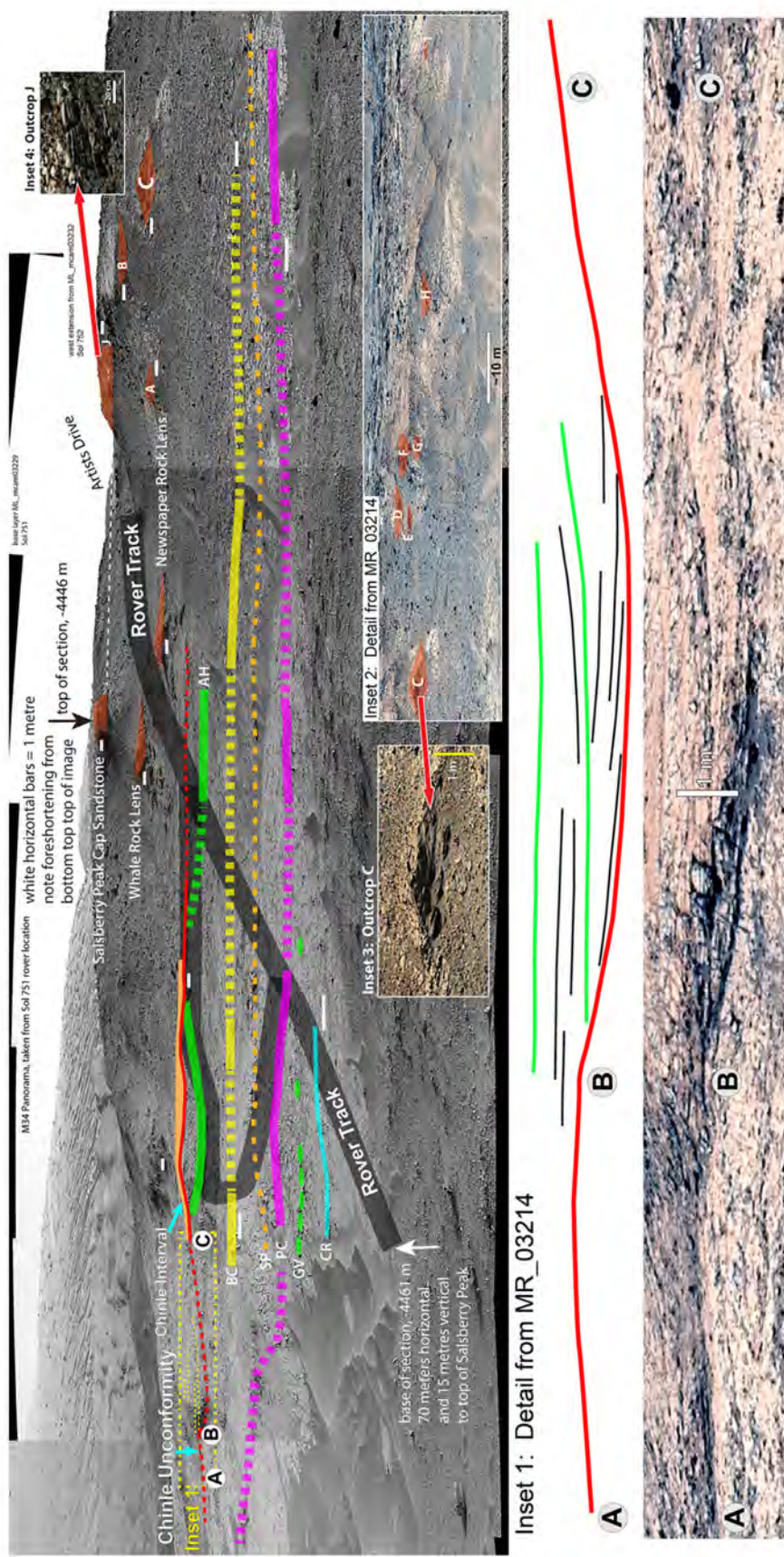


Fig. 4. The broader context of the observations made with the Curiosity rover in the Pahrump Hills area, looking south from the Sol 751 rover location. The dark ribbon labelled ‘rover track’ marks the places traversed and examined by the rover. The colour-coded quasi-horizontal lines mark intervals of more erosion resistant strata. Their extension away from the rover traverse (solid lines for presumed outcrop, dashed lines denoting correlation) is based on elevation measurements and the assumption that beds are approximately horizontal. Two letter abbreviations are: CR = Comb Ridge; GV = Gold Valley; PC = Pink Cliffs; SP = Saddle Peak; BC = Book Cliffs; AH = Alexander Hills (includes Carnivore Canyon). These abbreviations are also used in successive figures. The image illustrates the contrast between the lower (resistant horizons) and upper half (sandstone lenses, some identified with letters, and sandstone cap) of the succession, divided by a red line (partly dashed) that marks the Chinle unconformity, a major break in stratigraphic continuity. Inset 1 (upper left) shows details of stratification (stratal onlap) above this unconformity. Inset 2 (lower right) shows likely sandstone lenses (and their letter codes) further to the right from the main image (there is overlap of the images at sandstone lens C). Inset 3 (centre bottom) shows cross-stratification in sandstone lens C. Inset 4 (upper right) shows bedding in outcrop J, a lateral equivalent of the Salsberry Peak cap sandstone. Field of view is approximately 100 m wide. Appendix S3 is a higher resolution version of this figure.

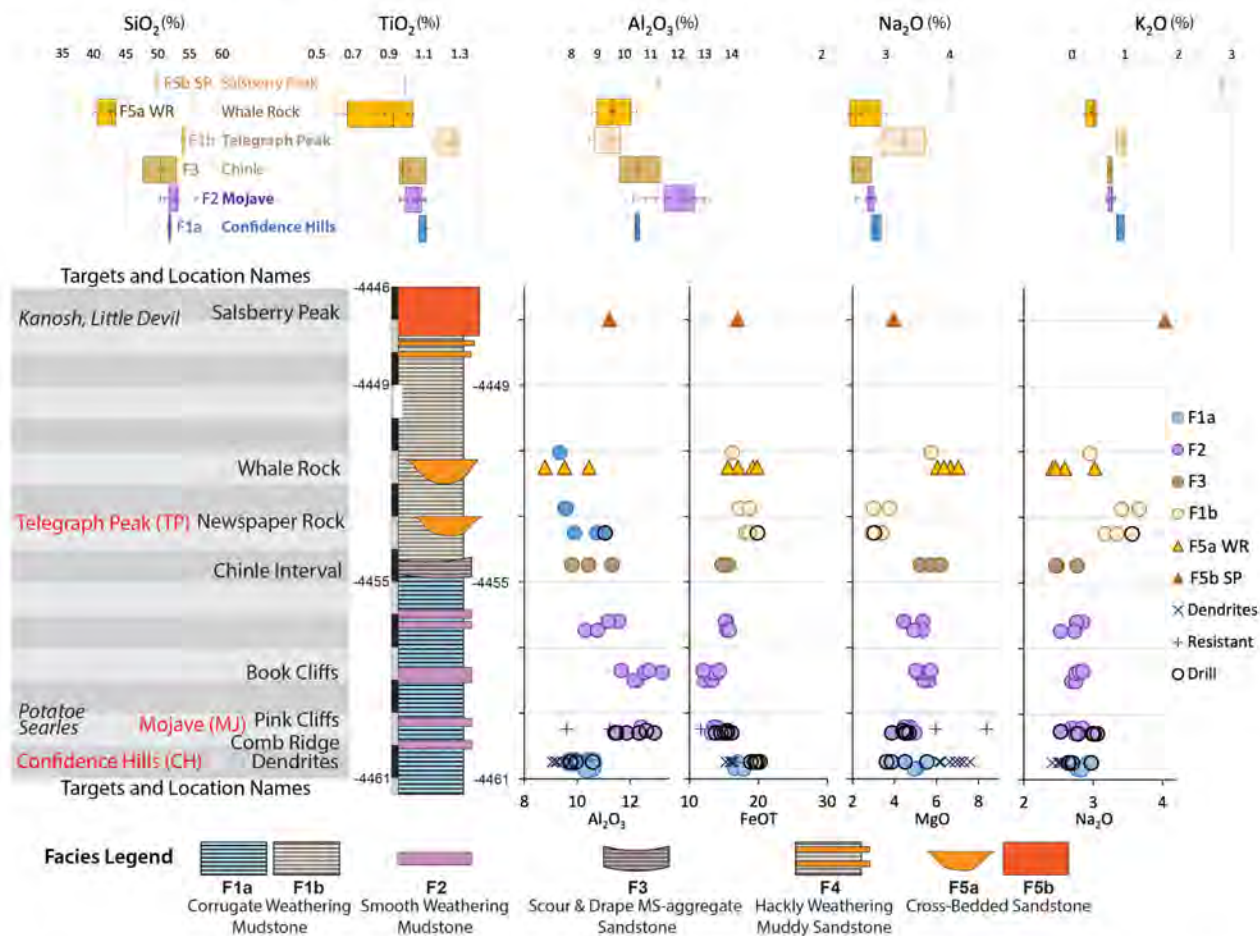


Fig. 5. Key APXS observations for the Pahrump Hill study site. Top row shows box & whisker plots of the abundances of detrital-hosted oxides SiO_2 , TiO_2 , Al_2O_3 , Na_2O and K_2O in the context of the facies shown in the summary stratigraphic column at the lower left and in Fig. 2. Box-and-whisker plots show data plotted with increasing elevation upward. X = mean, vertical line = median, left and right extent of boxes = interquartile range, whiskers = minimum and maximum. A complete set of APXS plots is available in Appendix S4. The bottom row of plots shows oxide abundances versus stratigraphic elevation, plotted to match the stratigraphic column at left. Data for F5a WR (Whale Rock) and F5b SP (Salsberry Peak) were acquired on float blocks but are plotted at the elevation of the source outcrop. The grey shaded block at the lower left shows locations and analysis targets mentioned in the text at their respective elevations in the outcrop.

diffraction pattern is clearly inconsistent with the presence of *only* opal-CT. Cristobalite fits well, refining to 11.2 (1.2%) and 12.7 (1%), with and without opal-CT, respectively (on an amorphous-free basis). The best fit is achieved when tridymite is considered in addition, even though it is not statistically significant [2.1 (1.9%)]. Crystallite size and strain parameters for tridymite and cristobalite indicate very small crystallites (*ca* 50 nm) and highly strained material, although values for tridymite are statistically unreliable due to the insignificant amount.

Phyllosilicate in both CH and MJ is indicated by a broad peak near 10 Å and minor

scattering above background near 10 Å in TP. It was modelled as kerolite [Brindley *et al.*, 1977; $\text{Mg}_3\text{Si}_4\text{O}_{10}(\text{OH})_2 \cdot n\text{H}_2\text{O}$], a talc-like (trioctahedral) 10 Å phyllosilicate. The kerolite model proved to be superior to any smectite models, and the bulk of the 10 Å phyllosilicate diffraction signature was attributed to kerolite. ChemCam analyses of erosion-resistant ridges show correlated MgO and Al_2O_3 enrichments (Fig. 6C), suggestive of an increased presence of Mg-bearing and Al-bearing authigenic phases (Appendix S2B). This observation is consistent with CheMin identification of kerolite and also points to the possible

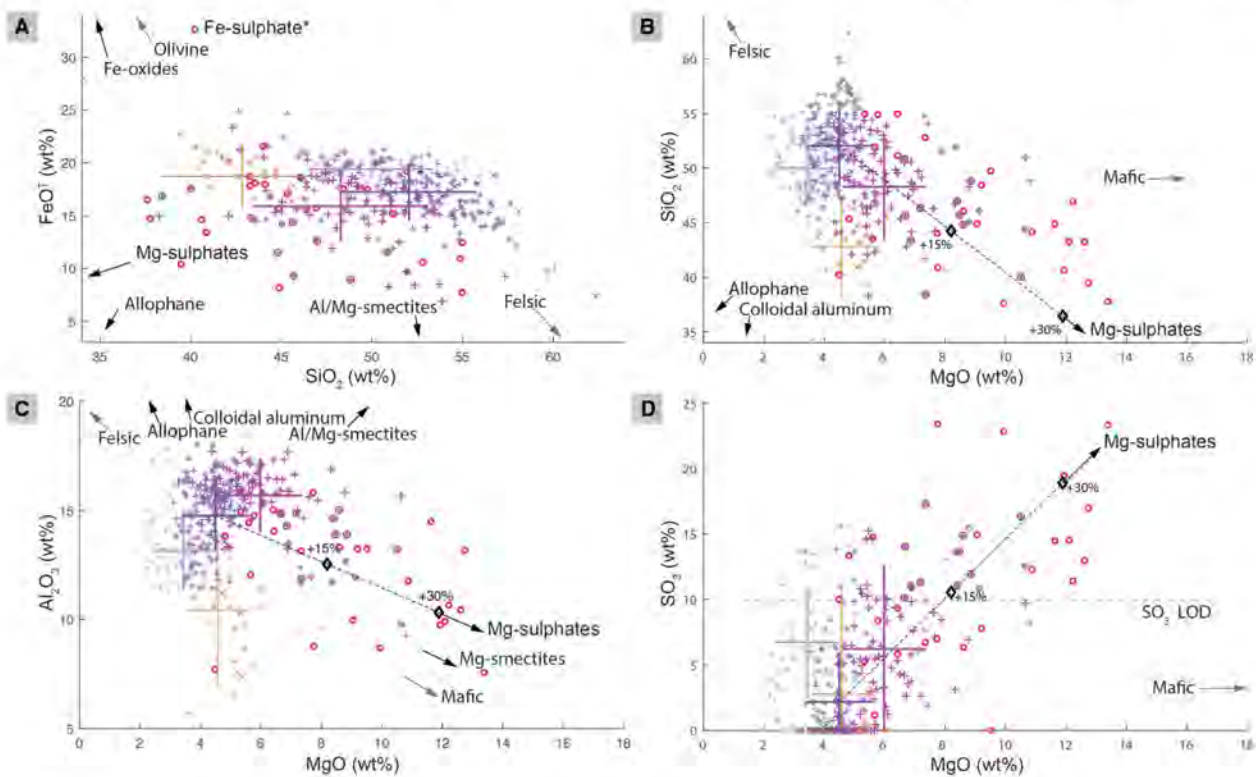


Fig. 6. ChemCam data on: (A) FeOT versus SiO₂; (B) SiO₂ versus MgO; (C) variability of Al₂O₃ relative to MgO, and possible implications with regard to Mg-smectites; and (D) enrichments in MgO content in bedrock that are associated with SO₃ enrichment, possibly an indication of Mg-sulphate minerals in the rock matrix. For explanation of symbols see legend in Fig. 7. Crosses indicate average composition and standard deviation for all bedrock groups, colour coding follows legend in Fig. 7. Arrows mark compositional trends for minerals implicated in discussion of data plot. The highest measured MgO contents near 13 wt. % could correspond to up to a ca 30 wt. % Mg-sulphate mixture with Pahrump mudstone locally. In (D) the horizontal line SO₃ LOD marks the ChemCam limit of detection (LOD) for sulphur.

presence of colloidal alumino-silicates like allophane and imogolite. In the lower part of the section there is also an indication of cyclic upward increase of MgO content towards strongly cemented mudstone intervals (Fig. 7).

Iron-bearing sulphates occur in all CheMin samples, along with pyrite. Calcium sulphate minerals occur in small amounts in CH and TP but not in MJ. Although Rampe *et al.* (2020) do not report Ca-sulphates in the Pahrump Hills CheMin samples, minor intensity discrepancies suggest their presence. Most Pahrump Hills mudstone APXS targets do not fit well on a CaSO₄ addition trend line in a CaO – SO₃ plot (Appendix S4), consistent with the presence of only minor CaSO₄ phases in the CheMin data (Table 2). Magnesium sulphates may be present in CH as well as in concretions and dendrites. Mg-sulphates kieserite (MgSO₄), sanderite

(MgSO₄•2H₂O), starkeyite (MgSO₄•4H₂O), hexahydrite (MgSO₄•6H₂O) and epsomite (MgSO₄•7H₂O) were evaluated for potential presence, but all except kieserite refined to 0% with large errors. Kieserite refined to 0.4 (2)% at CH and was statistically insignificant at MJ [0.2 (2)%] and TP [0.3 (3)%]. Its inclusion visually affected the fit in two regions for the CH X-ray diffraction (XRD) data, supporting its presence, whereas its inclusion did not visually affect the fit for MJ and TP. ChemCam analyses show scattered MgO enrichment in bedrock (up to 15 wt. %) that are associated with SO₃ enrichment, considered consistent with the presence of Mg-sulphates (Fig. 6D). High point-to-point variability indicates heterogeneous enrichment at a ca 100 µm scale (Maurice *et al.*, 2016). The highest measured MgO contents (ca 15 wt. %) could correspond to up to ca 30 wt. % Mg-sulphate

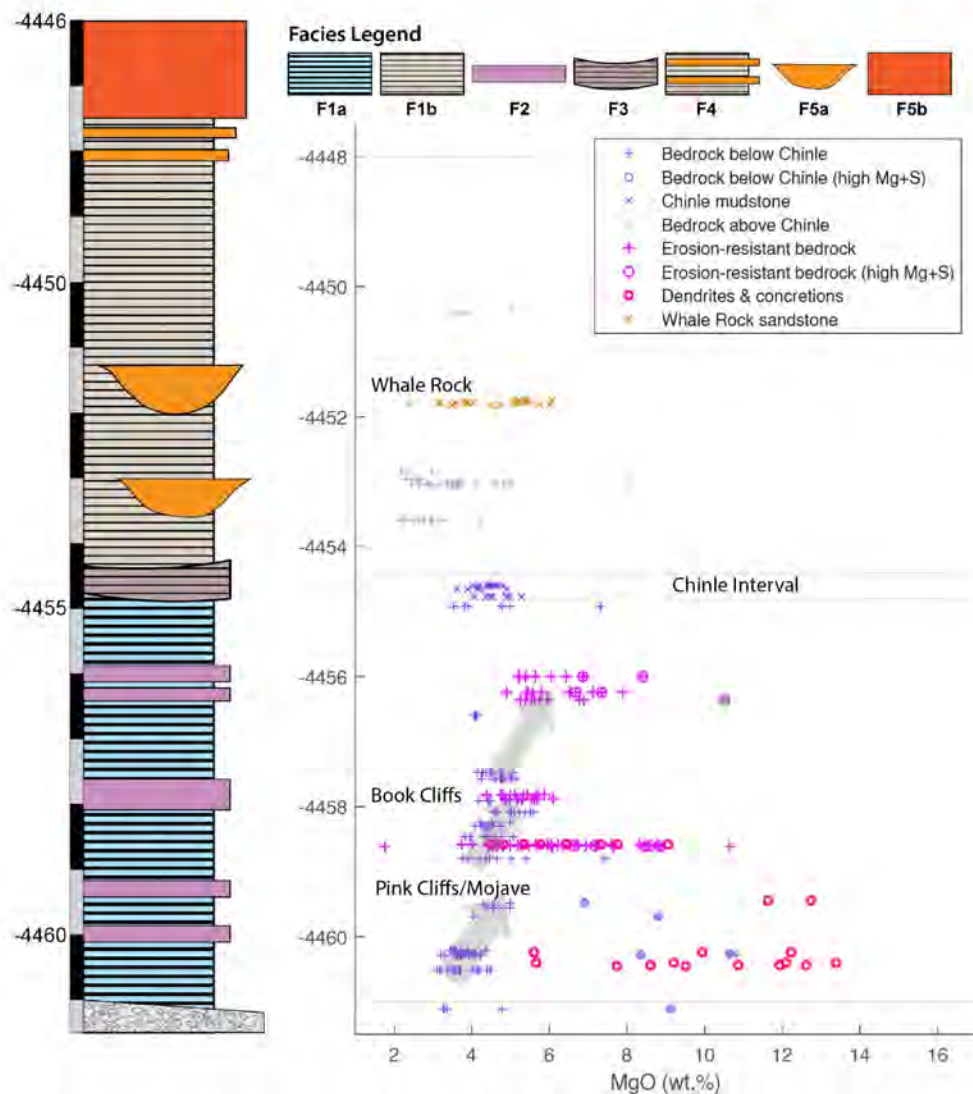


Fig. 7. ChemCam MgO content as a function of target elevation (vertical axis, in metres). Corresponding facies on column to the left (numbers left of column are elevation in metres). Bulk MgO content of the mudstone mostly varies between 3 wt. % and 6 wt. %, with a few scattered enrichments up to 13 wt. % MgO. Individual mudstone targets show relatively homogeneous MgO content, and the observed target-to-target variability in MgO content is therefore considered stratigraphically controlled. Shaded arrows point to part of the section where bedrock MgO values appear to increase systematically upward. Lowermost part of the section shows the top of the Panamint conglomerate.

and are associated with dendrites and concretions (Fig. 6). Most of the SO₃ detected by APXS in the Pahrump drill samples is accounted for in the amorphous component for each sample (Rampe *et al.*, 2020; Table 2).

Minor discrepancies between observed and modelled diffraction patterns suggest the possible presence of several minor phases in all CheMin samples: ilmenite, pyrite and apatite (see Appendix S2B). The potential presence of other

minerals was evaluated, including Mg-calcite, magnesite, siderite, calcite, pyrrhotite, marcasite, apatite, ilmenite, parabutlerite, gypsum, thenardite, trona and shortite. Of these, most refined to 0% or had errors greater than or equal to the refined value and therefore their presence in these samples is considered to be unlikely. Some are reported as trace amounts in Table 2, based on the effect their addition or deletion had on fit parameters and data plots.

Table 3. Sedimentary facies of the Pahrump Hills member, Murray formation.

Grain size	Facies F1 Corrugate weathering mudstone	Facies F2 Smooth weathering mudstone	Facies F3 Scour and drape mud aggregate sandstone	Facies F4 Hackly weathering muddy sandstone	Facies F5 Cross-bedded sandstone
F1a = interbedded with F2					F5a = discontinuous lenses
F1b = interbedded with F5a					F5b = laterally extensive
Detrital grains: probably dominated by particles <20 µm			Detrital grains: bimodal distribution – mud <32 µm; reworked ‘crystals’ and mud clasts <2 mm	Undetermined (probably mud to sand)	
Authigenic particles: <2 mm: 0.4 to 2.6 mm (mode: 1.3 mm) long by 0.15 to 0.35 mm (mode: 0.25 mm) wide in basal 0.5 m of section according to Kah <i>et al.</i> (2018)			Authigenic particles: <2 mm: 0.6 to 1.8 mm (mode: 1.1 mm) long by 0.2 to 0.6 mm (mode: 0.45 mm) wide at Pink Cliffs and Book Cliffs according to Kah <i>et al.</i> (2018)	<2 mm: 10 to 120 mm 1 to 3.5 mm	Laminae: not imaged; bed/ bedsets: 10 to 120 mm
Layer thickness	0.4 to 3 mm (below Chinle); 0.8 to 4 mm (above Chinle)				Laminae: 1 to 10 mm; Beds: 20 to 110 mm
Lamina/Bed geometry	Continuous planar- parallel to discontinu- ous planar-parallel		Continuous wavy parallel, discontinuous wavy parallel, continuous curved parallel; continuous planar parallel, continuous planar parallel, non- parallel	Discontinuous curved nonparallel, with sparse discontinuous wavy nonparallel, discontinuous wavy parallel, and continuous planar parallel	
Bedding terminations	Truncation, downlap, onlap	Truncation, downlap, onlap	Truncation, downlap	Truncation, downlap	Truncation, downlap
Sedimentary structures	Scour surfaces, planar- parallel beds	Scour surfaces, planar- parallel beds, current ripples	Scour surfaces, scour and drape bedding, planar- parallel beds	Scour surfaces, wavy parallel beds, current ripples	Scours, planar-parallel beds, current ripples, planar-tabular and trough cross-beds, compound cross-beds, foreset bundles, mud drapes

Table 3. (continued)

	Facies F1 Corrugate weathering mudstone	Facies F2 Smooth weathering mudstone	Facies F3 Scour and drape mud aggregate sandstone	Facies F4 Hackly weathering muddy sandstone	Facies F5 Cross-bedded sandstone
Composition	Feldspars, mafics, Fe-oxides, silica, phyllosilicates, sulphates (Fe, Ca, Mg), ilmenite, pyrite, apatite, shortite, allophane	Feldspars, Fe-oxides, mafics, phyllosilicates, silica, sulphates (Fe, Mg), pyrite, allophane	Probably reworked FA1 and FA2	Undetermined	Sand; feldspar (plagioclase), mafic minerals (pyroxene, olivine, magnetite), rock fragments, and mud clasts
Authigenic components	Crystal pseudomorphs, dendrites, stack concretions, isolated concretions (concretions sparse above Chinle)	Tabular concretions; oblate-spheroidal concretions (Potatoe, Searles)	Crystal pseudomorphs (reworked)	No centimetre-scale concretions observed	None observed
Crystal shapes	Rhomb, pyramidal-triangular, lath-blade, lozenge (white); rounded-oval (above Chinle only)	Pyramidal-triangular, tabular-rhomb-blade (black), tabular-lozenge hole, lath-blade, lozenge (white)	Pyramidal-triangular, rhomb, rounded-oval	Undetermined	Not apparent
Grain/Particle origin	Detrital mudstone grains; Authigenic <i>in situ</i> crystal pseudomorphs	Detrital mudstone grains; Authigenic particles; <i>in situ</i> and reworked authigenic particles	Detrital primary mudstone grains, Reworked mudstone clasts and crystal-shaped particles	Detrital mudstone and sandstone grains	
Provenance	F1a = Provenance A F1b = Provenance B F1a: 35%; F1b: 35%	Provenance A	Provenance A (multi-cycle)	Unknown	F5a = Provenance C F5b = Provenance D F5a: 7%; F5b: 10%
% of vertical section	6%	2%	5%		

Amorphous constituents

Of the samples analysed by CheMin, MJ has the highest abundance of amorphous material. Linear programming optimizations suggest Al_2O_3 enrichment in the MJ amorphous component relative to CH and TP. APXS analysis corroborates Al_2O_3 enrichment in MJ, and all other APXS analyses associated with erosion-resistant horizons of smooth weathering mudstone [Facies F2 (F2); Fig. 5] likewise show elevated Al_2O_3 concentrations, suggesting that Al-rich amorphous material (in the form of poorly ordered colloidal hydrous aluminosilicates, for example, allophane or imogolite) might contribute to the relative resistance of smooth weathering mudstone ledges (F2; Fig. 5). Allophane or imogolite is consistent with low-angle X-ray scattering seen in the MJ data, as well as with Al_2O_3 enrichment in the other resistant ridges inferred from ChemCam cross-plots of MgO versus Al_2O_3 (Fig. 6C).

FACIES AND STRATIGRAPHIC SUCCESSION

The mudstone-dominated Pahrump Hills succession (Figs 1 and 2) consists of five facies defined by texture, bedding and composition (Table 3). Outcrop observations were augmented with compositional analyses and examination of bed and bedset stacking patterns. Detail images (MAHLI) and compositional data were available for four facies. One facies (hackly weathering muddy sandstone, F4) was only examined via M100 MastCam images. These facies, the building blocks of a predictive model of the depositional system, are summarized below, with additional detail available in Appendix S5A.

Corrugate weathering mudstone facies (F1)

F1 consists mainly of continuous to discontinuous planar-parallel bedded feldspathic (Table 2) mudstone with sand-size crystal pseudomorphs, forming alternating layers of greater and lesser resistance to aeolian abrasion. Less resistant layers consist of poorly sorted mud, with coarse silt-size particles dispersed in a matrix of medium to fine mud (Appendix S5A; Lazar *et al.*, 2015; Schieber, 2018). The more resistant layers contain sand-sized sediment-incorporative crystal pseudomorphs (Schieber *et al.*, 2015; Kah *et al.*, 2018), that show rhombic, pyramidal-triangular, lath-blade and

lozenge shapes, along with rounded-oval shapes that occur only above the Chinle interval.

F1 mudstones form layers from less than a millimetre to as much as 4 mm thick which may show truncation, downlap and onlap (Fig. 8). Scours and undulose erosion surfaces are ubiquitous and can be traced laterally for up to 30 m (Fig. 9).

F1 is dominated by feldspars, mafic minerals and Fe-oxides, with minor amounts of opal-CT, phyllosilicates, sulphates (Fe, Ca, Mg), ilmenite, pyrite, apatite and shortite, along with allophane (Table 2). The harder layers harbour matrix-pervasive cements in addition to mudstone fines and sand-size crystal shaped features (Figs 10 and 11), considered pseudomorphs of sediment-incorporative crystals (the term ‘crystal pseudomorph’ is used in this paper) that occur throughout most of the succession. Recessive layers consist of softer mudstone (scratched by DRT bristles, Fig. 11A) that may contain scattered crystal pseudomorphs (Fig. 11). In places where they are exposed favourably between resistant layers, these softer layers can show stacks of discrete sub-layers (Fig. 12).

The outcrop appearance of F1 reflects the proportion of crystal-pseudomorph layers to recessive mudstone layers (Fig. 11). Although prior studies attempted to differentiate the layered mudstones into two subspecies, uneven discontinuously laminated and rhythmic laminated (Stack *et al.*, 2019), observations by Yawar *et al.* (2018) and Minitti *et al.* (2019) indicate that discontinuous layering is largely an artefact of exposure quality (Appendix S5A), and not a primary sedimentary feature. In favourable exposures these millimetre-scale layers can be traced for the entire metre-scale extent of near-rover MastCam images. Softer layers show considerably more variability in thickness than the more resistant crystal pseudomorph-rich layers.

Discontinuities, erosion surfaces and downlaps

Although parallel bedding is the dominant sedimentary feature of F1 mudstones (Fig. 8), careful examination shows subtle low-angle truncations, lamina downlaps and top-truncated laminae (Fig. 8). Truncation surfaces with a clear difference in lamina dip below and above the surface occur at multiple elevations in the section (Fig. 9) and may show considerable lateral extent (Fig. 9A to C). Observing these features at multiple levels along the random walk transect

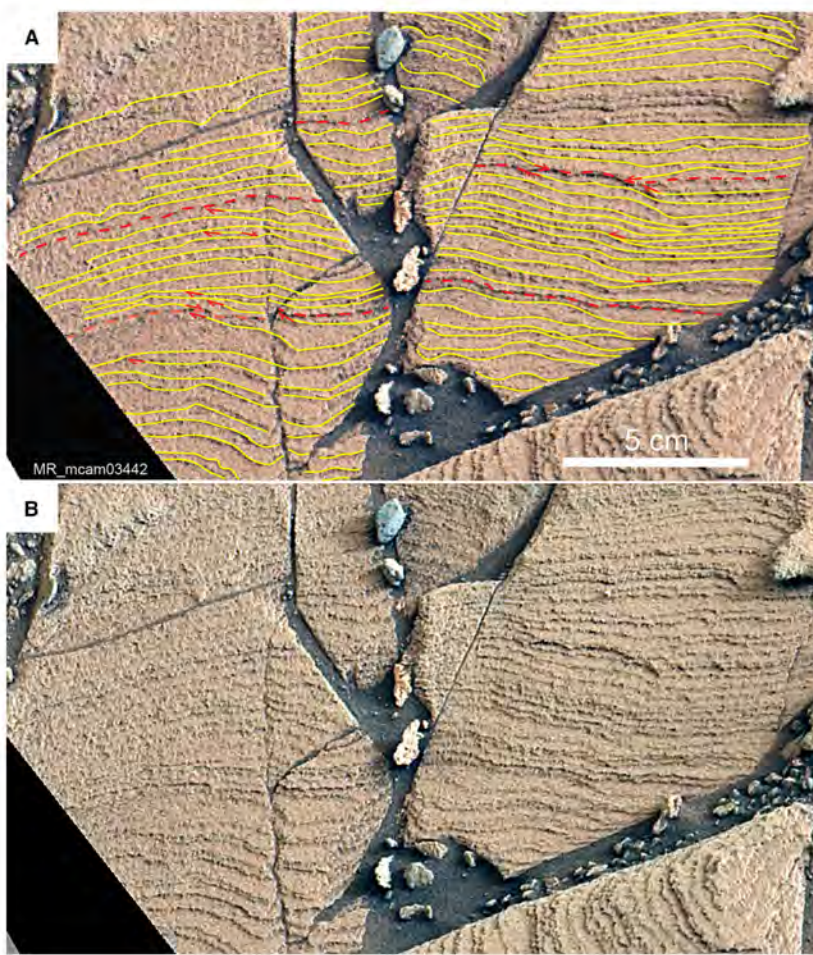


Fig. 8. (A) F1 – Beds of continuous planar to curved parallel to nonparallel laminae (yellow highlights) bounded by laterally persistent truncation surfaces (dashed red lines). Note localized truncation as well as lamina-scale downlap and possible onlap within the beds (red arrows) (Barstow area, ca -4457.4 m; MR_mcam03442). (B) The uninterpreted original image.

through the section suggests that they are likely common throughout.

Cementation, concretions and dendrites

Erosion-resistant features in F1 strata include lamina-scale cementation, prominently weathering millimetre-thick to centimetre-thick layers, concretions and dendrites (Figs 13 and 14). Laminae of millimetre-scale (with crystal pseudomorphs) represent the smallest scale of cementation, followed by centimetre-scale ‘stack concretions’ (Fig. 14) that are restricted to specific stratigraphic intervals, bedsets of discontinuous flat concretions (Fig. 15), and finally decimetre-thick laterally extensive resistant ledges. The latter show sufficient textural differences (for example, composition, bedding thickness and geometry) from F1 to qualify as a separate, though closely related, facies (F2, smooth-weathering mudstone).

Dendrites show elongate branches parallel to bedding, range in size from *ca* 1.5 to 4.5 cm

(Minitti *et al.*, 2019) and only occur at the base of the section. They appear to be cemented by MgSO₄ (VanBommel *et al.*, 2016), whereas XRD and geochemical data point to allophane, opal-CT and Fe-oxides (see *Compositional data and inferences*) as plausible cementing agents for millimetre-scale to decimetre-scale resistant layers (Ming *et al.*, 2006; Pain *et al.*, 2007; Rampe *et al.*, 2012; Blake *et al.*, 2013; Meslin *et al.*, 2013; Weitz *et al.*, 2014; Lowe *et al.*, 2020).

Systematic variations within F1 strata

Although the common denominator of F1 strata is the alternation of softer and harder layers at sub-millimetre-scale to millimetre-scale, two distinct sub-categories (Fig. 16) can be differentiated on the basis of bedding, weathering characteristics, chemical composition and interbedded facies. F1a (found below Chinle, -4454.8 m) is closely associated with centimetre-scale to decimetre-scale concretions and dendrites and interbedded with resistant ledges of F2 strata. In

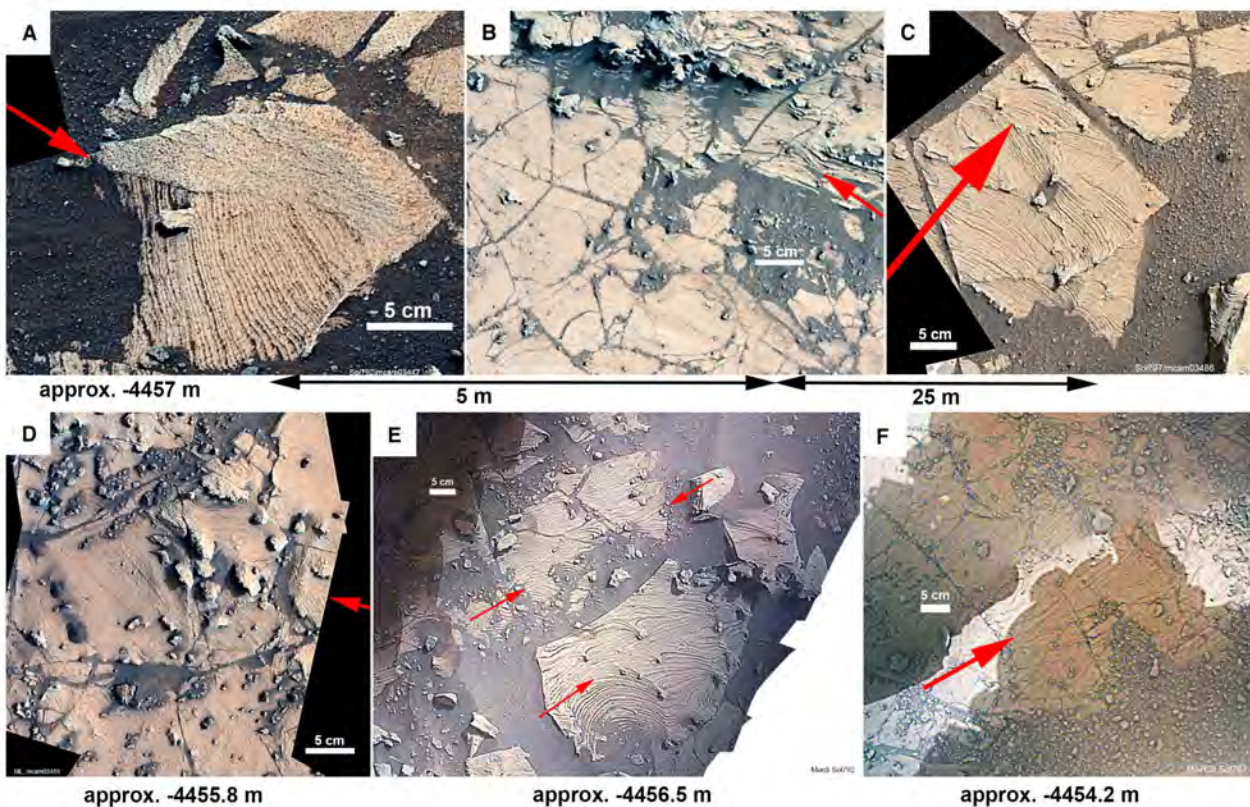


Fig. 9. Truncation horizons in the corrugate-weathering mudstone facies (F1). (A) to (C) Three occurrences that were observed at an elevation of approximately -4457 m , over a lateral distance of 30 m . In all images red arrows point to truncation surface. The truncation at (A) may scour into the substrate by several decimetres. (D) to (F) Examples of truncation surfaces at other elevations. Images (A) through to (D) were acquired by MastCam, images (E) and (F) were captured with MARDI (Minitti *et al.*, 2019). F1 mudstone exposures invariably show fracture networks, but these fractures are not related to desiccation at the time of deposition. They are filled with modern surface sediment and are considered the result of exposure and weathering near and at the surface long after deposition.

F1b (found above Chinle and below Salsberry Peak; Fig. 2) the harder layers are darker in colour (Fig. 16), appear more easily traceable, yet still contain crystal pseudomorphs. Compositinally it differs from F1a (see *Compositional data and inferences*; Figs 5 and 7; Appendix S4), by containing more SiO_2 , Ti, Na and P, and less Ca, Mg, S, Al, Mg and Ni. F1b strata contain lenses of cross-bedded sandstone (F5a), host few concretions and do not contain F2 resistant ledges. Some nodule-like features were observed between -4452.8 m and -4453.5 m .

First order interpretation of F1

Mineral and elemental composition (Fig. 5; Table 2) indicate that detrital components of all facies were eroded from basaltic bedrock and

transported to the lake by streams. Authigenic components reflect the dissolved load of inflowing streams and groundwater, generated by the interaction of low-pH precipitation with basaltic bedrock, impact-melts and ejecta blankets (e.g. Schwenzer *et al.*, 2012; Arp *et al.*, 2019).

Softer layers in F1 are interpreted as poorly cemented detrital mudstone, settled from intermittent hypopycnal suspension plumes that extended offshore. Lamina downlap, truncation and erosion surfaces with localized channelization indicate bottom currents that eroded lake muds and transported mud aggregates across the lakebed as bedload (Schieber *et al.*, 2010, 2019). Multiple laminae in softer layers (Fig. 12) suggest multiple detrital pulses between successive harder layers (no 1 : 1 pairing of softer and harder layers). The thickness of softer layers serves as a

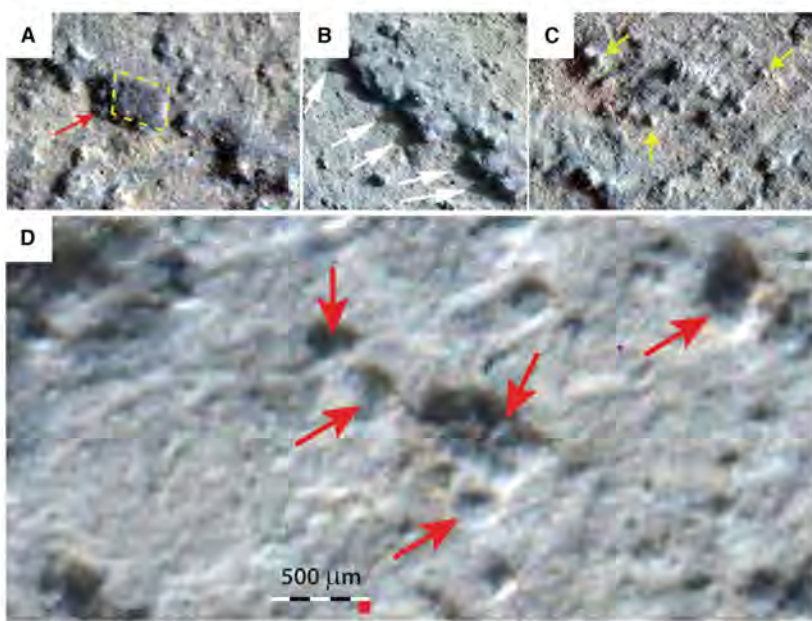


Fig. 10. F1 – Crystal-rich layers in the brushed MAHLI target ‘Pelona’. The resistant layers contain abundant angular sand-sized objects. (A) to (C) Detail views of these objects. (A) A rhombic shape (yellow dashed line) that is raised above the rock surface and casts a rhombic shadow (red arrow). (B) Triangular (dog-tooth like) shadows (white arrows) cast by a row of these objects. (C) Pyramidal and triangular objects (yellow arrows) that project above the rock surface. (D) A pixel-scale look at the rock surface. Red arrows point to sand-sized objects – see (A) to (C) – that are suspended in a rather homogenous matrix. The red square below the scale bar is the size of a coarse silt grain (63 μm). Most of the matrix appears finer than coarse silt and shows random single pixel variability (see Appendix S2A).

measure of clastic supply to the lake basin. Higher SiO_2 concentrations were observed in F1b. SiO_2 phases are considered detrital, because if they were pervasive secondary cements, F1b should be notably harder than F1a.

Harder layers have the same detrital components as the softer layers but were cemented by abundant authigenic components soon after deposition. Comparisons with saline and hyper-saline lake strata on Earth (e.g. Smoot & Lowenstein, 1991; Rosen, 1994; Warren, 2006; Renault & Gierlowski-Kordesch, 2010) suggest that the crystal pseudomorphs in harder layers originated as evaporite minerals that grew in surficial muds as sediment-incorporative (poikilotopic) crystals prior to burial. Initially evaporite minerals may have accumulated as lake floor cumulate or bottom-growth crystals. Subsequent dissolution formed brines that sank into the bottom muds and crystallized as sediment-incorporative crystals due to a combination of changes in lake water evaporation and ambient temperature. Harder layers are now an amalgam of detrital particles, crystal pseudomorphs and cements.

Multiple evaporite minerals were probably present initially (variety of crystal pseudomorph shapes), an inference supported by XRD and compositional data, as well as chemical modelling results. Calcium sulphate (gypsum) was most common, along with Mg-sulphate (epsomite, etc.), Na-sulphate (thenardite), and others [Na-Ca carbonates (gaylussite/pirssonite, now shortite) and Mg-silicate (kerolite)]. CheMin analyses illustrate that the original mineralogy of these rocks has been altered substantially post-deposition.

The erosion resistance of these layers is owed to a combination of opal-CT, Fe-oxide and allophane cements. Crystal shapes in F1 (Fig. 10) are reminiscent of evaporitic lake muds from the Green River Formation (Schieber *et al.*, 2015). Although CheMin data (Table 2) and morphology (Kah *et al.*, 2018) suggest gypsum as the dominant evaporite mineral, there are a great many monoclinic minerals, and other evaporite minerals, such as trona ($\text{Na}_2\text{CO}_3 \cdot \text{NaHCO}_3 \cdot 2\text{H}_2\text{O}$), that are equally plausible (Fig. 17D). Pyramidal-triangular crystal pseudomorphs in F1 (Fig. 10)

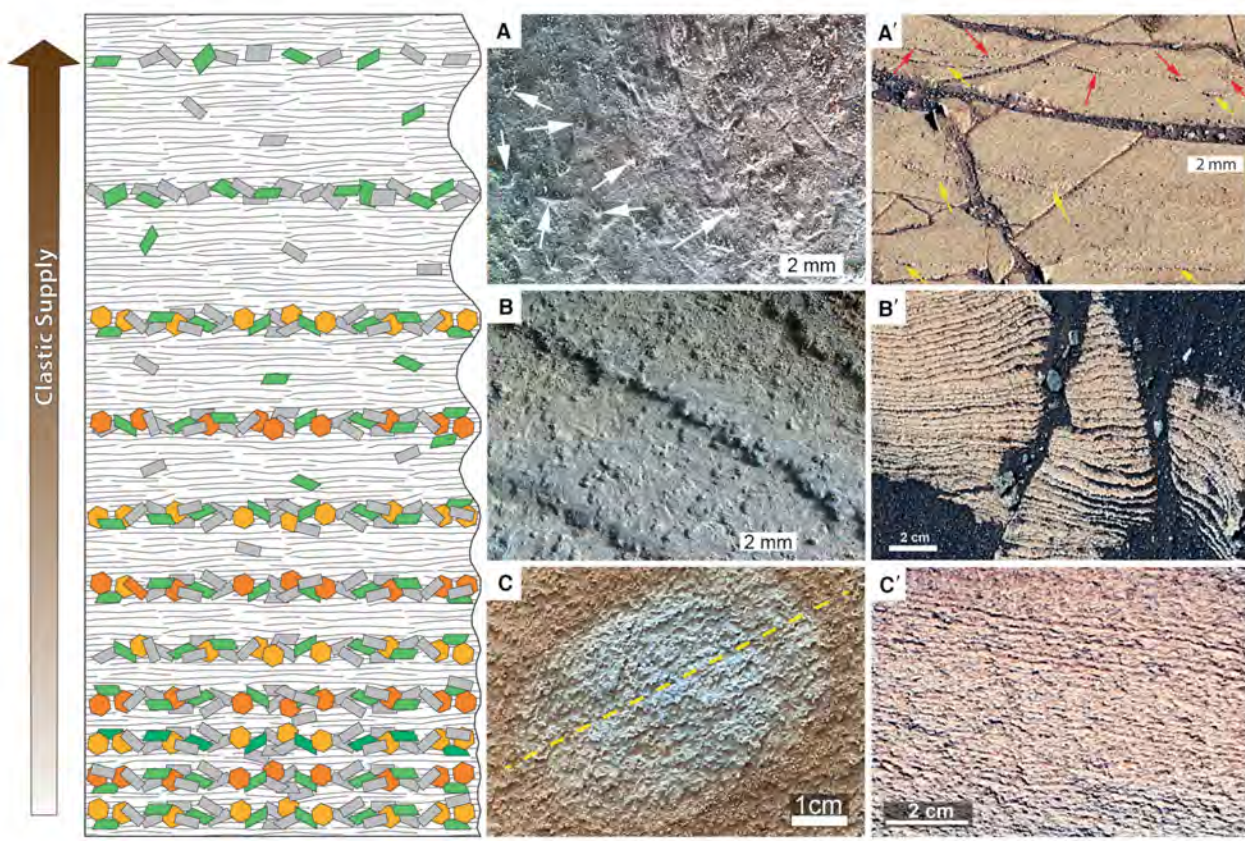


Fig. 11. A summary of outcrop appearance of F1 (images on the right) versus proportion of crystal layers and recessive mud layers (sketch on left). What one sees in outcrop is a continuum from mud-dominated (upper third of figure) to crystal-pseudomorph dominated (lower third of figure). (A') Outcrop with widely spaced crystal layers (yellow and red arrows), suggestive of discontinuous crystal layers. (A) Surface between crystal pseudomorph layers with crystal shapes (white arrows) embedded in the mudstone matrix. Concentric scratches were made by the bristles of the DRT tool. (B') Outcrop with intermediate spacing of crystal pseudomorph and mudstone layers, with well-developed recessive nature of mudstone layers. (B) Step-wise retreat of crystal pseudomorph layers. (C') Outcrop where mudstone layers are very thin and layering is easily missed in the presence of surface dust. (C) A closer view of such a surface. The dashed yellow line indicates orientation of layering. It is possible to recognize the crystal-pseudomorph layers in places, but the dominant impression is a hackly surface dominated by crystal shapes.

are reminiscent of shortite-rich beds of the Green River Formation (Fig. 17), and detection of trace shortite in F1 samples (CH and TP; Table 2) hints at the tantalizing possibility of abundant sodium–calcium carbonate minerals in the original deposits. The shortite is probably the product of burial diagenesis of the primary hydrated sodium–calcium carbonate minerals gaylussite or pirssonite that precipitated on or in the shallow sediment column; a situation analogous to that interpreted for the Wilkins Peak member of the Green River Formation (e.g. Bradley & Eugster, 1969; Jagniecki *et al.*, 2013). The implications of initial trona and gaylussite/pirssonite are profound, offering the prospect of

early carbonate precipitation. Instead of an exclusively acid-saline system, the brine evolution pathway IIIa of Eugster & Hardie (1978) is indicated. Detection of trace authigenic minerals (shortite, thenardite and kieserite; Table 2) is consistent with lacustrine evaporites (Eugster & Hardie, 1978) and provides a modicum of plausibility that the observed pseudomorphs may indeed reflect depositional conditions at the time of accumulation and shortly thereafter, and not be a consequence of pervasive late-stage alteration.

The generally thicker detrital-dominated recessive layers in F1b are likely due to higher clastic flux to the lake basin (Renaut &



Fig. 12. A fortuitous insight into the nature of layering as seen in adjacent blocks of the same stratigraphic level. Two layers, 1 and 2 (marked by red and blue arrows respectively) can be followed across blocks. In the right block, aeolian abrasion has exposed five pseudomorph-rich layers ('a' through 'e') below layer 1. In the left block (lower left), there are 15 much thinner and rather similar layers visible over the same thickness of rock. In addition, even though layering in the right block is defined by pseudomorph-rich layers, in the upper right of that block are faint hints of additional (less resistant) layers (white arrows) between layer 1 and the first resistant pseudomorph-rich layer below it (yellow arrow e). These faint layers are also visible on the left side of the image and are marked with a double arrow.

Gierlowski-Kordesch, 2010). The associated increase of fluvial discharge and reduced salinity hindered formation of strongly cemented ledges, although background salinity remained high enough to allow intermittent formation of crystal-enriched harder laminae.

Although F1 mudstone exposures invariably show fracture networks (for example, Figs 9 and 13), these fractures are filled with modern surface sediment and are considered the result of exposure and weathering near and at the surface. The apparent absence of primary desiccation cracks in spite of likely intermittent exposure in saline lake systems, as well as the lack of differential compaction around presumably early diagenetic cementation features (stack concretions and flat concretions) is puzzling. Even without desiccation, synaeresis cracks might be expected under presumed variable salinity (Burst, 1965; Plummer & Gostin, 1981). Laboratory experiments described below explored this issue further.

MAHLI images (Schieber, 2018) and CheMin data (Table 2) show that the Pahrump Hills

mudstones consisted largely of non-clay-mineral grains (feldspars, pyroxene, olivine, etc.) $<63\text{ }\mu\text{m}$ at the time of deposition. Generally observed random single pixel variability (RSPV; Appendix S2A) suggests a mudstone matrix with an abundance of particles $20\text{ }\mu\text{m}$ and smaller in size. Experiments with mixtures of commercially available crushed and sieved quartz with similar grain-size distributions ($50\text{ }\mu\text{m}$ and finer) with BentoliteTM (Ca-montmorillonite) showed that, once settled from suspension, such mixtures had grain-supported fabrics of remarkable mechanical robustness (Fig. 18).

These fabric analogue experiments (see Appendix S5B for details), as well as the low clay-mineral content (Table 2; *ca* 4% or less), suggest the presence of a grain-supported fabric that would have prevented both desiccation and synaeresis cracks. Locally, though, there may have been more clay-mineral-rich layers (not visited by the rover) that developed cracks, became erodible and were coherent enough to be transported and incorporated in secondary deposits.

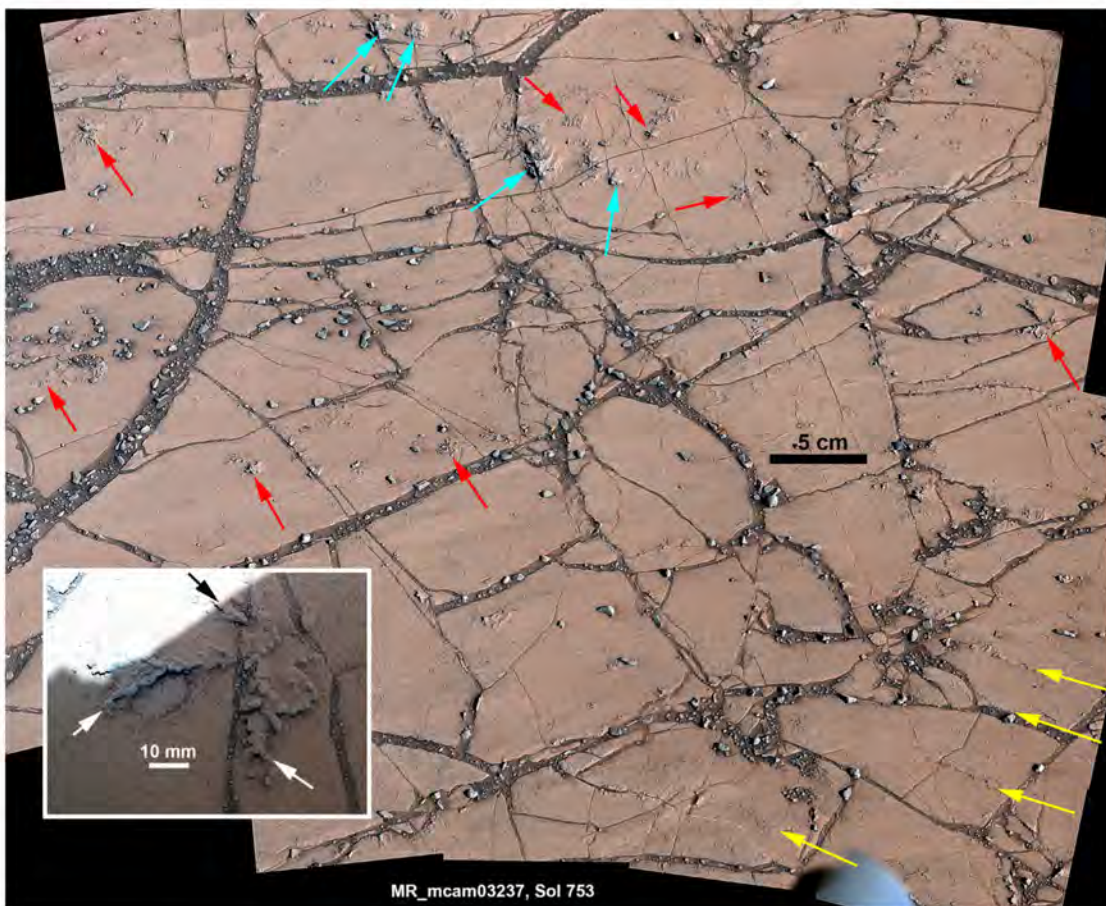


Fig. 13. Localized cementation features in F1. Yellow arrows point to more resistant, presumably better cemented laminae and laminaset structures. Red arrows point to dendrites that were exposed by aeolian abrasion of the enclosing mudstone matrix. The lower left inset shows a detail view of one of these dendrites (white and black arrows) that is clearly more resistant than the enclosing rock. Blue arrows point to concretions that represent more pervasive cementation. Image is from the basal metre of the Pahrump Hills outcrop (Fig. 5). This exposure shows a well-developed fracture network with fractures filled by modern surface sediment. They are therefore considered the result of exposure and weathering near and at the surface long after deposition.

Another outcome of these experiments concerns the apparent absence of differential compaction around concretions in Pahrump mudstones (Fig. 14). On Earth this is commonly interpreted to mean late diagenetic formation (Raiswell, 1971; Potter *et al.*, 1980), but at low clay content, grain support by silt grains severely limits compaction potential. Experimental compaction of silts to a *ca* 3 km burial equivalent (assuming Mars gravity of 3.721 m s^{-2} , which is about a third of Earth's gravity at 9.802 m s^{-2} ; Appendix S5B) does not show significant differential compaction (Fig. 19). Thus, absence of differential compaction around nodules in Pahrump mudstones

(Fig. 14) is not in conflict with early diagenetic formation. In addition, the resulting mudstone fabric appears to have very low permeability (Appendix S5B; Fig. S5B-2) suggesting that late-stage diagenesis by pervasive fluid flow is an unlikely scenario.

In summary, F1 appears to have accumulated in a distal sublittoral depositional environment with variable but overall relatively low sedimentation rates. Benthic energy was variable, but at times sufficiently high to erode lake bottom muds and transport them laterally. Laminae enriched in likely evaporite pseudomorphs, as well as comparison to Earth analogues, suggests an overall saline–evaporitic lake system.

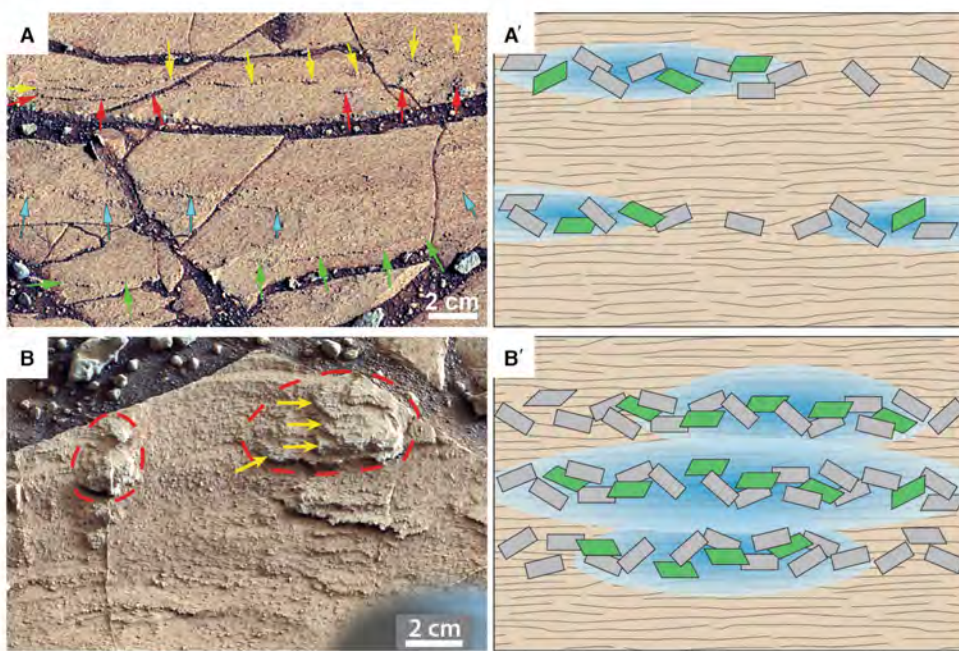


Fig. 14. Cementation of pseudomorph-rich layers in F1. (A) Discontinuous patches of cement in outcrop with low abundance of pseudomorph-rich layers that are marked with coloured arrows (MR_mcam03237, ca –4460.5 m). (A') Schematic sketch of cement growth in pseudomorph-rich layers. (B) Formation of 'stack-concretions'. Cementation 'hot spots' (marked with dashed red lines) extend vertically across multiple layers (MR_mcam03513, ca –4460.7 m). Yellow arrows mark laminae within the right 'hot spot'. (B') Schematic sketch that considers these as fused cement patches in vertically adjacent layers. Crystal shapes are grey and green rectangles and cements are indicated by blue tones. The mudstone matrix is indicated by a wavy-lined beige pattern.

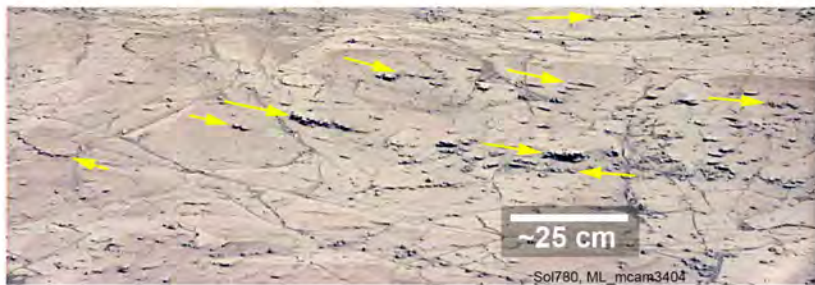


Fig. 15. Discontinuous cemented horizons marked by yellow arrows (near rover image, camera pointing down). Thicker horizons like the one marked A–A' appear to follow a specific stratigraphic interval (ML_mcam3404, ca –4458.3 m).

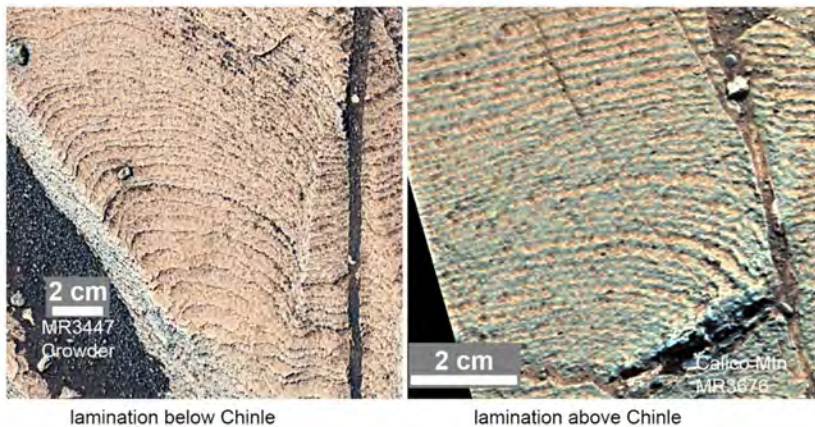


Fig. 16. Visual comparison of the two types of corrugate-weathering mudstone (F1) encountered at Pahrump Hills. At left, an example of F1a (below Chinle) and of F1b (above Chinle) at right.

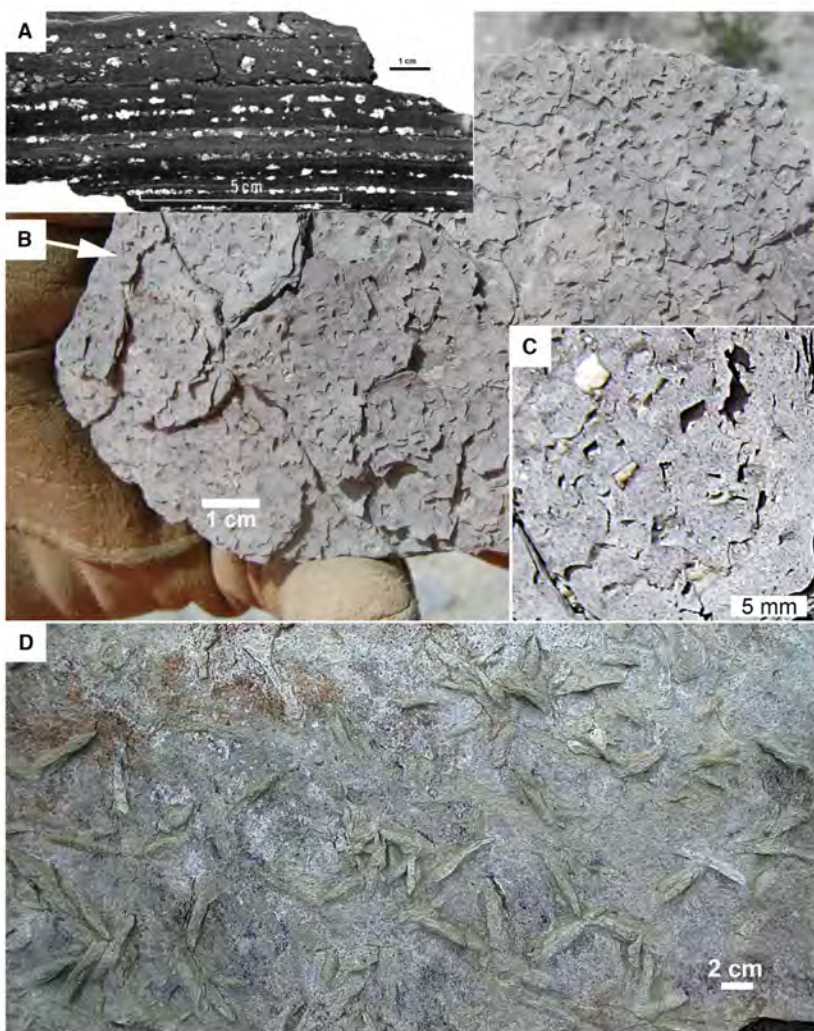


Fig. 17. Crystal pseudomorphs in evaporative lacustrine strata from the Green River Formation of Wyoming. (A) Laminated lake mudstone (Wilkins Peak member) with layers of calcite pseudomorphed shortite crystals (from Bradley & Eugster, 1969). (B) A bedding plane view of (A) that shows crystal moulds and crystals. The crystals were pseudomorphed from shortite by calcite during outcrop weathering. Note textural similarity to crystal pseudomorph layers shown in Fig. 10. (C) Enlarged portion of (B) that shows crystal moulds and calcite pseudomorphs after shortite (light-whitish). (D) Calcite pseudomorphs of trona on mudstone bedding plane.

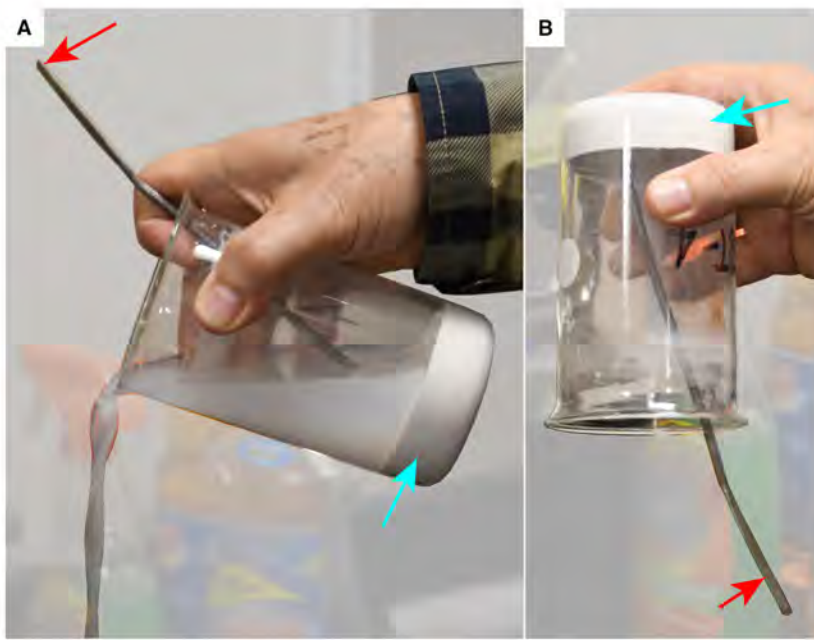


Fig. 18. A beaker with a poorly sorted quartz silt deposit after two days of settling. (A) Image illustrates that the sediment plug (blue arrow) does not collapse and flow as the beaker is tilted and the water is poured out. The deposit is hard to the touch and a spatula (red arrow) is stuck in the wet deposit. (B) Even once the beaker is inverted, the spatula remains stuck in the deposit. It is even possible to lift up the sediment plug plus beaker by pulling on the spatula. Silt samples with an admixture of small quantities of smectite (5 to 8 wt. %) behave essentially the same.

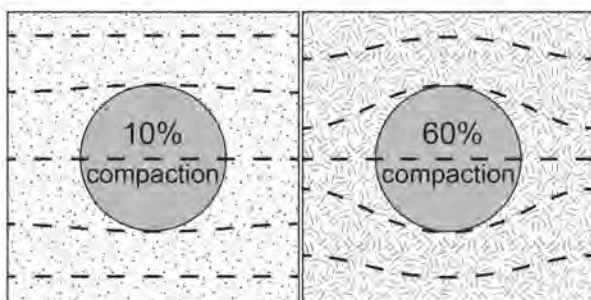


Fig. 19. Illustration of compaction induced lamina deflection likely in silt dominated mudstones (left) as found at Pahrump, and typical lamina deflection observed in clay-rich mudstones (right) on Earth. Even if the rover were to image the outcrop with the camera axis parallel to layering, it would be a challenge to tease out the small amount of differential compaction associated with silt-dominated mudstones.

Smooth weathering mudstone facies (resistant ledges, F2)

F2 forms prominent ledges in outcrop and consists of 3 to 20 mm thick layers with generally smooth appearance where exposed to aeolian abrasion. Its rock matrix is comparable in grain size to F1, with variable amounts of dispersed objects of coarse silt to sand size. Sedimentary structures include scours, planar-parallel beds and current ripples (Fig. 20) with planar to concave cross-laminae in centimetre-scale sets of wedge to trough shaped geometry. F2 intervals generally have gradational bases and sharp tops.

F2 (as analysed at MJ; Table 2) is dominated by feldspars, mafics and Fe-oxides, with minor amounts of silica, phyllosilicates, sulphates (Fe, Mg), ilmenite, pyrite, apatite and shortite, along with allophane. Notably missing is any trace of Ca-sulphate minerals. F2 resistant ledges contain consistently higher Al, Si and Cr, and lower Fe and K concentrations than F1 strata (Fig. 5; Thompson *et al.*, 2020), and have elevated Mg (Fig. 7) relative to interbedded F1a. This is interpreted (see *Compositional data and inferences*) to reflect finely dispersed Mg-sulphate in addition to Mg-smectites. Weathering resistance appears to be due to pervasive cements that may include allophane/imogolite, opal-CT and Fe-oxides.

F2 is the most extensively cemented facies, and forms decimetre-thick ledges (Fig. 21) that impart a distinct character to the interval below Chinle (Figs 2 and 4). Some ledges extend laterally for several metres, appear confined to

narrow stratigraphic intervals (Minitti *et al.*, 2019; Yawar *et al.*, 2019), and resemble tabular concretions seen in terrestrial mudstone successions (Potter *et al.*, 1980).

F2 ledges contain smaller concretions (Figs 21 and 22), internal layering (Fig. 23) and crystal pseudomorphs (Kah *et al.*, 2018). Visible layer thickness is 7 to 25 times of that observed in F1 (Appendix S6). Crystal pseudomorphs show multiple distinct shapes and colours: pyramidal-triangular, black tabular-rhomb-blade, tabular-lozenge hole, lath-blade and white lozenge (Schieber *et al.*, 2015; Kah *et al.*, 2018). Assemblages of pseudomorph shapes change in successive horizons (Appendix S6) and can be associated with voids that apparently were once occupied by crystals (Fig. 23).

First order interpretation of F2

F2 accumulated under variable benthic energy, from quiescent to capable of transporting sand-sized grains as bedload. Judging from thicker laminae/beds in F2, sediment supply rates were higher than for F1a. Truncations indicate erosion of surface muds and generation of mud-aggregates, and suggests currents of the same or larger magnitude than needed for ripple formation (Schieber *et al.*, 2010; Schieber, 2011). In combination with downlapping laminae, this attests to interaction of currents and waves with the lakebed (Kelts & Hsü, 1978; Smoot & Lowenstein, 1991).

Although F2 layers contain crystal pseudomorphs, presumably induced by supersaturation, their erosion resistance is unlikely due to evaporite minerals. More plausibly, their hardening can be attributed to a combination of early diagenetic cementing agents, including opal-CT, Fe-oxides and allophane/imogolite, an inference that is supported (see *Compositional data and inferences*) by geochemical (Figs 5 and 6) and XRD data (Table 2). Allophane is associated with hardpans and other erosion-resistant layers in lacustrine strata on Earth (Butt, 1983; Thornber *et al.*, 1987; Warren & Rudolph, 1997; van Breemen & Buurman, 2002), and has been interpreted similarly on Mars on the basis of global orbital observations and surface analyses at Gusev and Gale craters (Ming *et al.*, 2006; Pain *et al.*, 2007; Rampe *et al.*, 2012; Blake *et al.*, 2013; Meslin *et al.*, 2013; Weitz *et al.*, 2014; Lowe *et al.*, 2020). The pervasiveness of early cements was likely a function of longer periods of sediment starvation, as well as sediment porosity, intensity and variability of evaporation, and

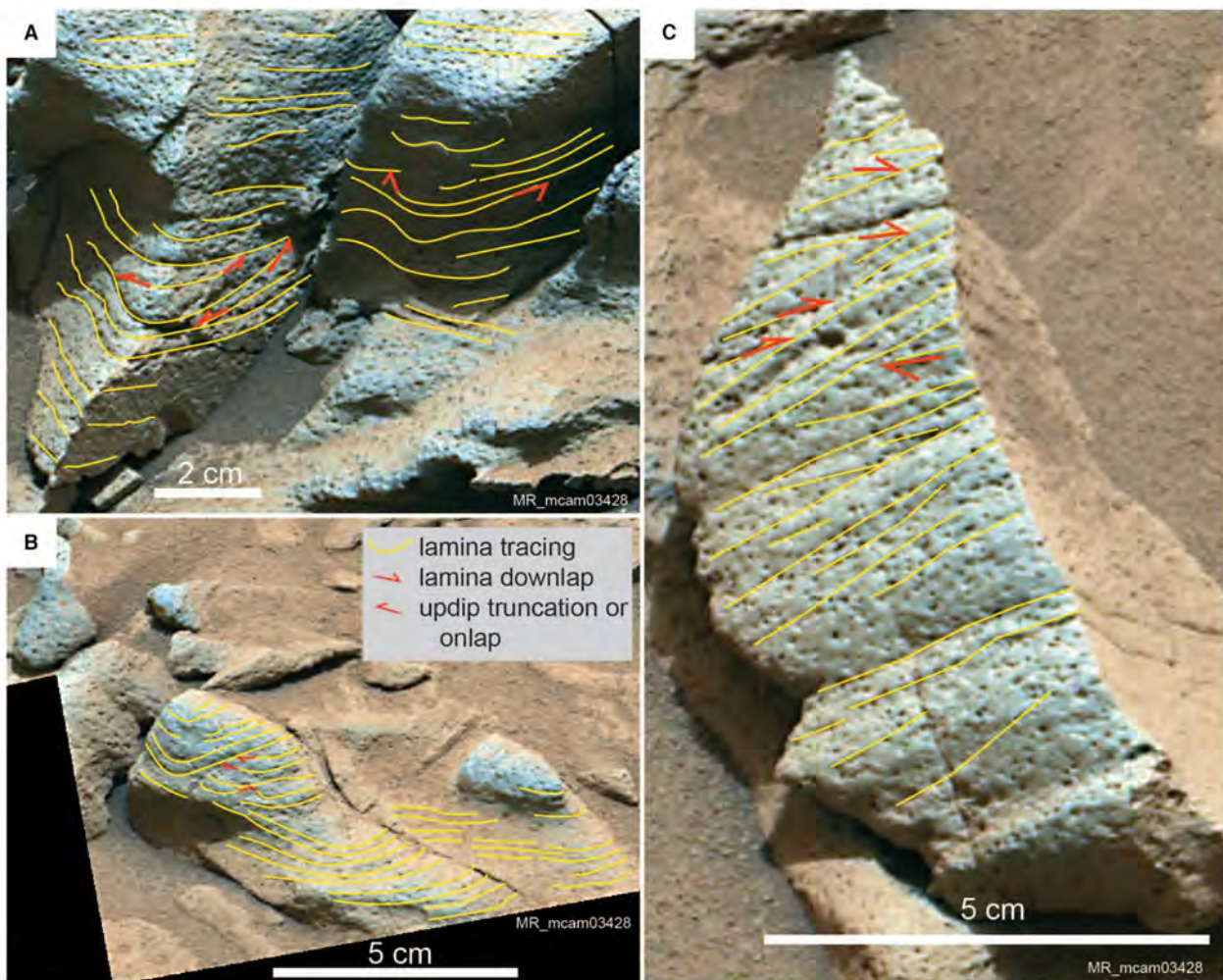


Fig. 20. Examples of sedimentary structures in F2 that record erosion and traction transport. (A) to (C) Images show marked up (yellow tracings, red arrows) discontinuous curved nonparallel lamina geometry, curved to planar laminaset boundaries and lamina-scale downlap and top truncation that are diagnostic of current-ripple bedding, even in mudstone strata (Campbell, 1967; Lazar *et al.*, 2015): (A) in particular shows a three-dimensional view enabling accurate characterization of lamina geometry in flow-parallel and flow-transverse views. (Book Cliffs interval, ca -4457.7 m elevation; MR_mcam03428.) An unmarked version of this image is included in Appendix S5A.

groundwater salinity (Hardie, 1968; Smoot & Lowenstein, 1991). As in F1, crystal pseudomorphs in F2 may reflect dissolution–reprecipitation of finer, cumulate evaporite particles (Smoot & Lowenstein, 1991).

Kah *et al.* (2018) proposed that most of the crystal pseudomorphs at one of the F2 ledges (Pink Cliffs, MJ) were originally gypsum. Yet, Ca-sulphates are clearly present in cross-cutting veins everywhere at Pahrump, have been detected by CheMin at CH and TP in F1 strata (Table 2), but were not detected at MJ. Stable Ca-sulphates in outcrop and rock matrix at CH

and TP beg the question why location MJ, where the former presence of gypsum is surmised on the basis of morphology (Kah *et al.*, 2018), is devoid of even a trace. Alternatively, the gypsum identification may be mistaken – not implausible, given the large number of minerals in the monoclinic system. As discussed above (F1 interpretation), trona is a plausible alternative based on crystal shape (Fig. 17D), as is shortite (traces detected at CH and TP; Table 2) or pirssonite.

The oblate–spheroidal concretions seen in Fig. 22 (targets Potatoe and Searles, Pink Cliffs

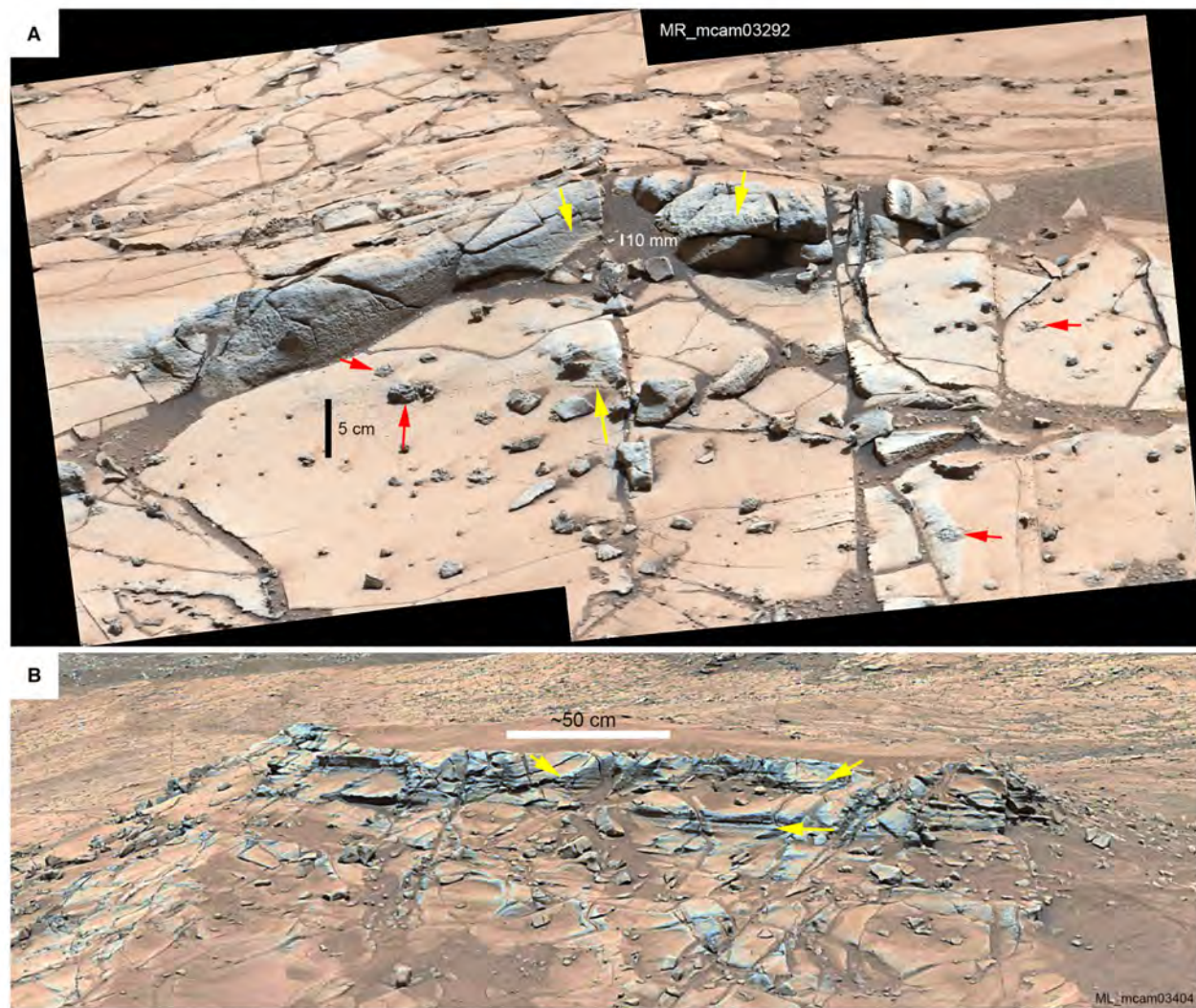


Fig. 21. Cemented F2 intervals of decimetre thickness. (A) Comb Ridge (*ca* 1 m above base of section) forms a resistant ledge, with internal layering 3 to 6 mm thick (yellow arrows), whereas layers in the underlying mudstone are generally <1 mm thick. Red arrows point to concretions that are enclosed in the more pervasive ledge forming cementation. From a distance, these appear to be of the ‘stack concretion’ type illustrated in Fig. 14. (B) Book Cliffs (*ca* 3 m above base of section) is the thickest cemented interval, and internal layers (yellow arrows) are up to 20 mm thick.

ledge) closely resemble crystal ‘biscuits’ reported from perennial saline lakes on Earth. There they are attributed to crystal growth at local nucleation centres on the lake floor in water depths as shallow as 10 to 20 cm (Müller & Irion, 1969; Weiler *et al.*, 1974; Warren, 1985; Smoot & Lowenstein, 1991). Overall, F2 is interpreted to have accumulated in a sublittoral depositional setting, with higher energy and sediment influx than F1, and possibly closer to shore. Benthic energy was variable from quite low to intermittently capable of eroding and

transporting mud, mud aggregates and coarse-silt to sand-size particles as bedload to form ripples and planar-parallel beds. As surmised for F1, observations from F2 suggest an overall saline–evaporitic lake system.

Scour and drape mud-aggregate sandstone facies (F3)

From direct observation, F3 appears to be a continuous wavy parallel bedded felspathic sandy mudstone. Grain-size distribution is

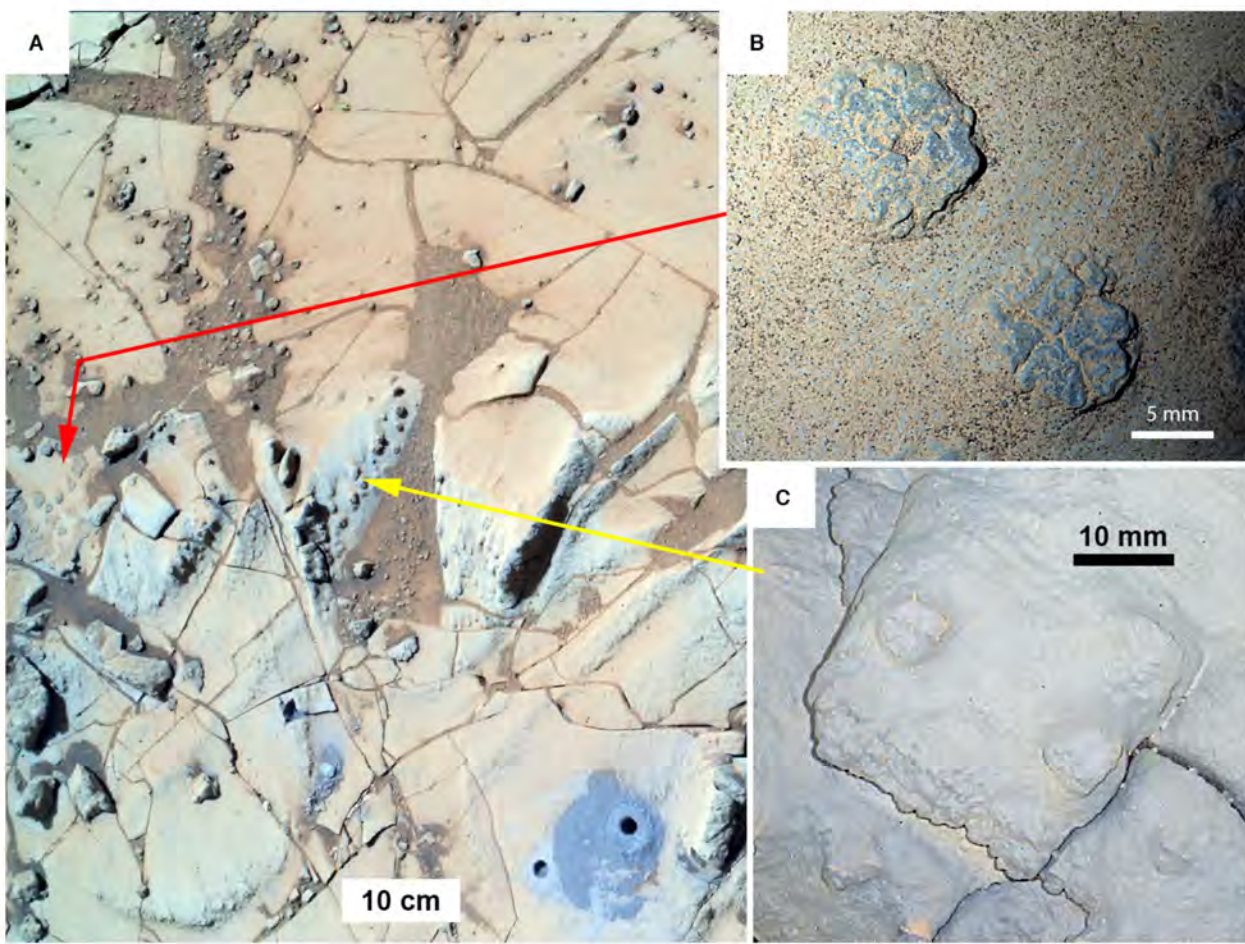


Fig. 22. (A) Plan view of the Pink Cliffs cemented ledge (F2), the site of the Mojave drill hole (bottom right). (B) Oblate-spheroidal concretions on a bedding plane ('Potatoe' target), showing a clear margin relative to the surrounding rock. Red arrow points to location in outcrop. (C) Concretions of the same type that are in the process of being exhumed from a ledge by aeolian abrasion ('Searles' target).

distinctly bimodal: a poorly sorted matrix of medium to fine mudstone (Lazar *et al.*, 2015; Schieber, 2018) with dispersed coarse silt size particles, as well as particles that range from 63 µm to *ca* 2 mm (Figs 24 and 25). Discernible grain shapes at the >63 µm scale include sharp-edged relatively equant pyramidal-triangular and rhombic, and sharp-edged tabular, comparable in appearance to the crystal pseudomorphs observed in F1, as well as a significant proportion of rounded particles (Figs 24 and 25). F3 only occurs only in the Chinle interval (−4455 m and −4454 m; Figs 2, 4 and 5; Appendix S7) and overlies a truncation surface that can be followed for ≥50 m across the hillside (Fig. 4; Appendix S8).

Sedimentary structures include scour and drape beds on a wavy basal surface with up to

5 cm local relief (Fig. 26; Appendix S9A and B) with continuous and broadly wavy parallel internal laminae that are 1 to 2 mm thick and evenly spaced vertically. Bedsets range in thickness from a few centimetres to 10 cm and contain, in places, low-angle cross-lamination where successive overstepping laminae lap down onto the underlying truncation surface (Appendix S7).

Superficially, F3 is similar to underlying F1a, but the scour and drape geometry is unique to F3. Deeply recessive softer layers and very resistant harder layers (Appendix S7) also distinguish F3 from F1. Given that the sand-size particles resemble crystal pseudomorphs seen in F1a and F2 and are embedded in a mudstone matrix (Fig. 24), the presumption is that the softer recessive layers are mudstone as well.

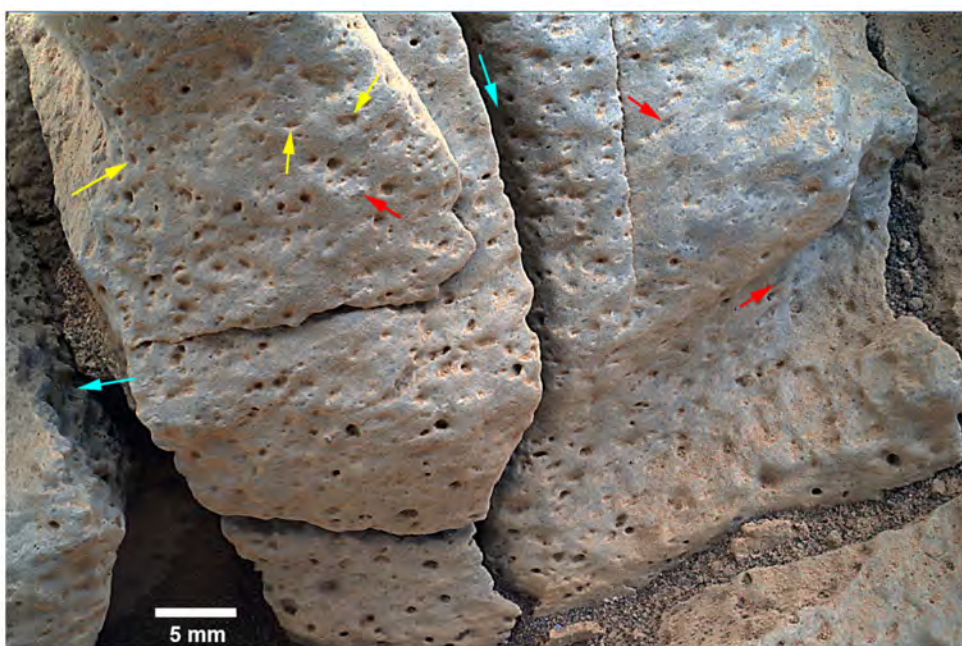


Fig. 23. Development of millimetre-size cavities in a strongly cemented F2 interval at Book Cliffs (Fig. 21B). These voids still show the outlines of pre-existing crystals (yellow arrows). In places crystal shapes are flush with the aeolian abraded surface or stand slightly above it (red arrows). The best cavity development is seen inside fractures (blue arrows) that protect from aeolian abrasion and may retain moisture. These observations suggest that cavity development is largely due to dissolution of more soluble crystals, rather than to aeolian abrasion, and that crystals of varying resistance to dissolution and abrasion are encased in the cemented matrix.

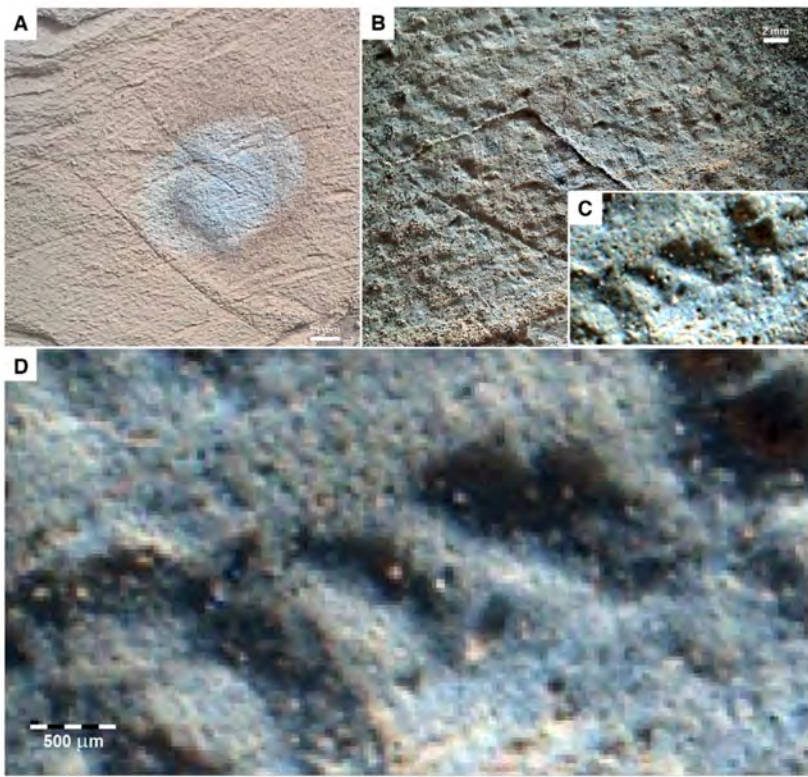


Fig. 24. Crystal pseudomorphs and matrix grain size in F3 at Chinle. (A) A bundle of dominantly harder layers with a brush spot in the centre (target Pickhandle). The rough surface texture is due to various crystal shapes projecting above the surface. (B) Close-up view of the brush spot in (A). (C) Shadowing of surface depressions indicates pyramidal-triangular depressions that were once occupied by crystals. (D) A pixel-scale look at the rock surface. Dark areas are shadowed crystal moulds, surrounded by a rather homogenous matrix that is finer than coarse silt and shows random single pixel variability (RSPV; see Appendix S2A).

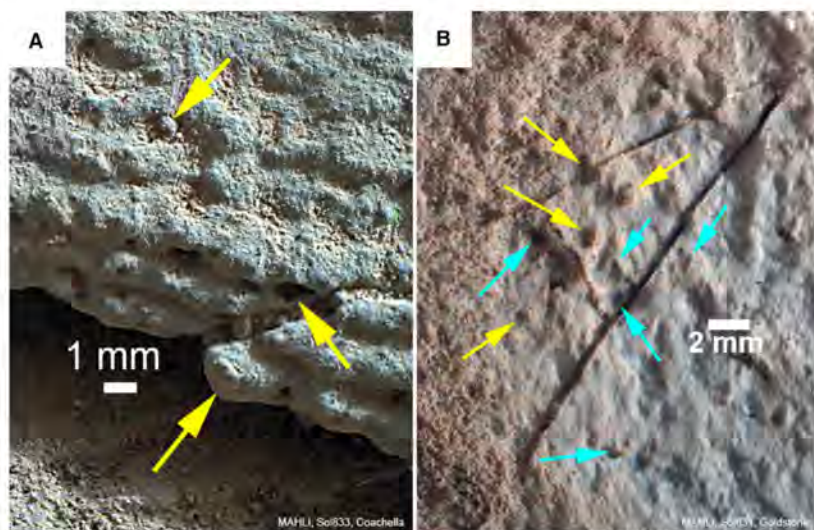


Fig. 25. Rounded grains and hollows in F3. (A) Harder layers with rounded grains and hollows (yellow arrows). (B) Mixture of rounded hollows (yellow arrows) and euhedral crystal shapes and hollows (blue arrows) on brushed surface.

Compositionally F3 overlaps with underlying F1 and F2 mudstones (Fig. 5). Chemical analyses of sharp-edged to rounded particles (Figs 24 and 25) suggest only small amounts of non-detrital minerals in these, indicating that they likely originated as pseudomorphs of sediment-incorporative crystals that grew within surficial muds (just as inferred for F1).

First order interpretation of F3

Compositional similarities between F1a, F2 and F3 (Fig. 5; Appendix S4) indicate that the detrital components of F3 were plausibly reworked from underlying F1 and F2 strata, consistent with its position above an erosion surface (Fig. 4; Appendices S8 and S10). The undulating scour surfaces and draping laminasetss resemble storm-wave reworked sandy strata on Earth (Brenchley *et al.*, 1993). Truncation surfaces and scour and drape bundle-wise buildup suggest intermittent strong currents, and low-angle downlap and convergence of laminae (Fig. 26; Appendix S7) indicate lateral migration of low-amplitude bedforms (Middleton & Southard, 1984; Rubin, 1987) and re-distribution of eroded sediments by wave-induced currents.

Likely erosion from underlying mudstones suggests that F3 sediments once consisted of mud-dominated composite particles (MCPs) that plausibly ranged in size from coarse silt to sand (Li *et al.*, 2021). MCPs can survive substantial amounts of reworking and transport (Schieber *et al.*, 2010; Schieber, 2016), and are an important component of modern and ancient muddy deposystems (Nanson *et al.*, 1986; Rust & Nanson, 1989; Wakelin-King & Webb, 2007; Li &

Schieber, 2018; Schieber *et al.*, 2019). Smoot & Lowenstein (1991) report that scour and fill structures, beds of intraclasts and storm-produced graded beds are common in saline and hypersaline terrestrial lakes. Although positive identification of MCPs requires scanning electron microscopy (Schieber, 2016; Li & Schieber, 2018), the high benthic-energy levels implied by erosion and bedform buildup strongly suggest their presence.

Alternating crystal-pseudomorph-rich and mud-rich laminae implies grain segregation in a flow that simultaneously transported crystals and MCPs in bedload. High energy conditions and strong currents are consistent with rounded MCPs and crystal pseudomorphs. Detrital evaporite minerals can be a significant aspect of perennial saline lakes on Earth (Smoot & Lowenstein, 1991), and rounded evaporite particles imply physical reworking under more dilute waters (Last & Schwegen, 1985; Logan, 1987) and such high-energy settings as shallow sublittoral zones with significant wave activity (Mees *et al.*, 2012). In contrast, gypsum crystals in modern terrestrial aeolian deposits are generally reported as undamaged and uncorroded (Mees *et al.*, 2012; Trichet, 1963, Trichet, 1967).

Summarizing, F3 is interpreted to have accumulated in a proximal sublittoral depositional environment, in shallower, more persistently energetic waters than F1a or F2. The environment was frequently subjected to waves and currents capable of eroding mud and transporting sand-size and larger mud aggregates as bedload.

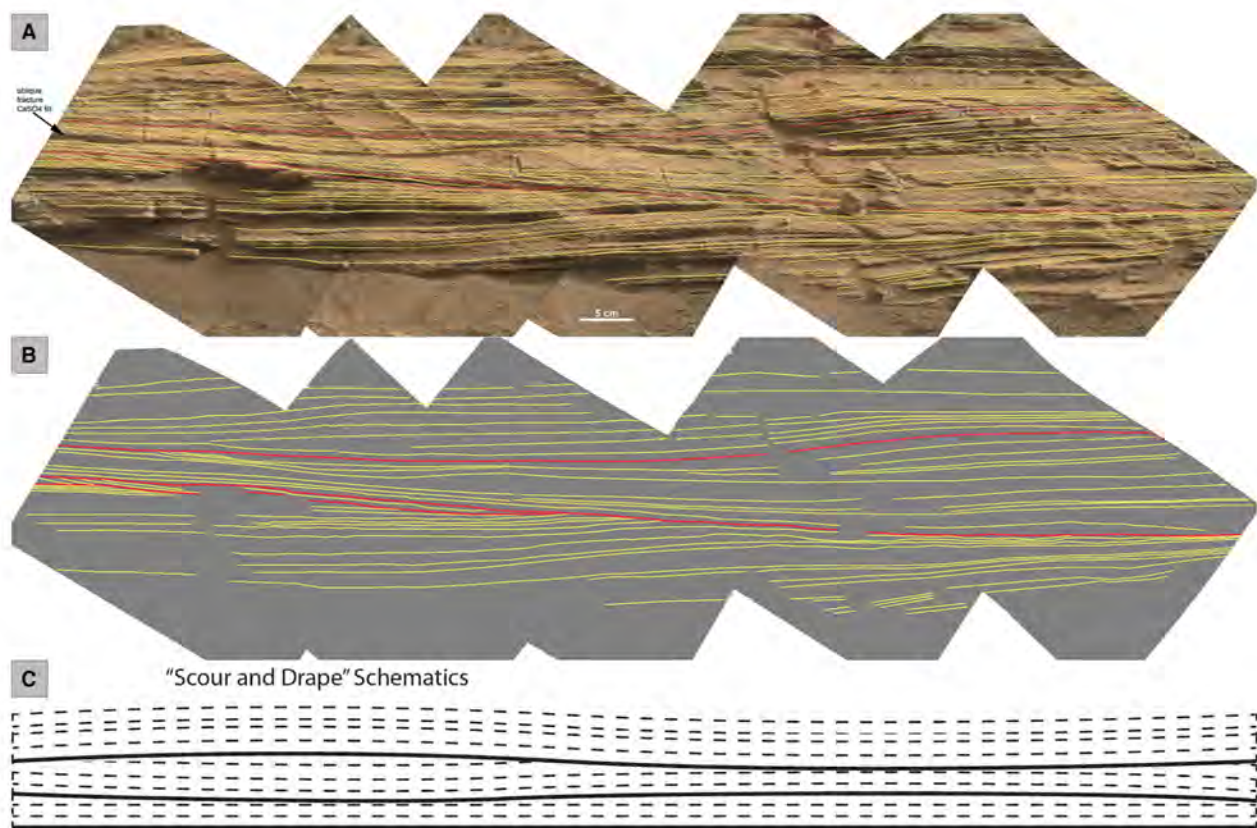


Fig. 26. F3 at Chinle. (A) A MAHLI composite image from Sol 828 that shows gently undulating scour surfaces (traced in red) that are draped by approximately conformable packages of laminated mudstone with resistant crystal pseudomorph-rich layers (traced in yellow). (B) The tracings from (A) on a grey background for better visibility. One can see truncation of layers below scour surfaces (red lines), as well as low-angle downlap and lamina convergence suggestive of lateral bedform migration (shown in more detail in Appendix S8). (C) Schematic summary of 'scour and drape' bedding. A higher resolution version of this figure is available as Appendix S9A. Appendix S9B is an unmarked version (without yellow tracing).

Hackly weathering muddy sandstone facies – F4

F4 comprises hackly (rough) weathering strata whose descriptions are mainly based on two image sets from the west and east sides of Artists Drive (MR_mciam04175, and MR_mciam04119; Fig. 27). Grain-size range was inferred from bedding geometry, stratigraphic context and weathering characteristics. Mudstone-dominated bedsets are interbedded with more resistant bedsets that are interpreted as coarser grained sandstones, have sharp bases, mostly sharp tops, and are from 1 to 12 cm thick.

F4 strata occur in a 2.0 to 2.5 m thick interval below the Salsberry Peak sandstone cap (Fig. 5), whose layers appear to coarsen and thicken upward, transitioning from mudstone through

sandy mudstone and muddy sandstone to sandstone, and showing progressive increase of the sandstone to mudstone ratio (Fig. 5). The interpretation of F4 is combined with the interpretation of the overlying F5b sandstone (below) because they are likely genetically related.

Cross-bedded sandstone facies – F5

The cross-bedded sandstone facies (F5) occurs in two modes: (i) as laterally isolated exposures (lenses) in the interval from –4454 to 4451 m (F5a); and (ii) as laterally extensive exposures in the interval above –4449 m (F5b).

Laterally isolated cross-bedded sandstone (F5a)

F5a sandstones are very fine to coarse (discernible grains 100 to 700 µm) and moderately

Murray Formation, Salsberry Peak interval,
Pahrump Hills, Gale Crater, Mars

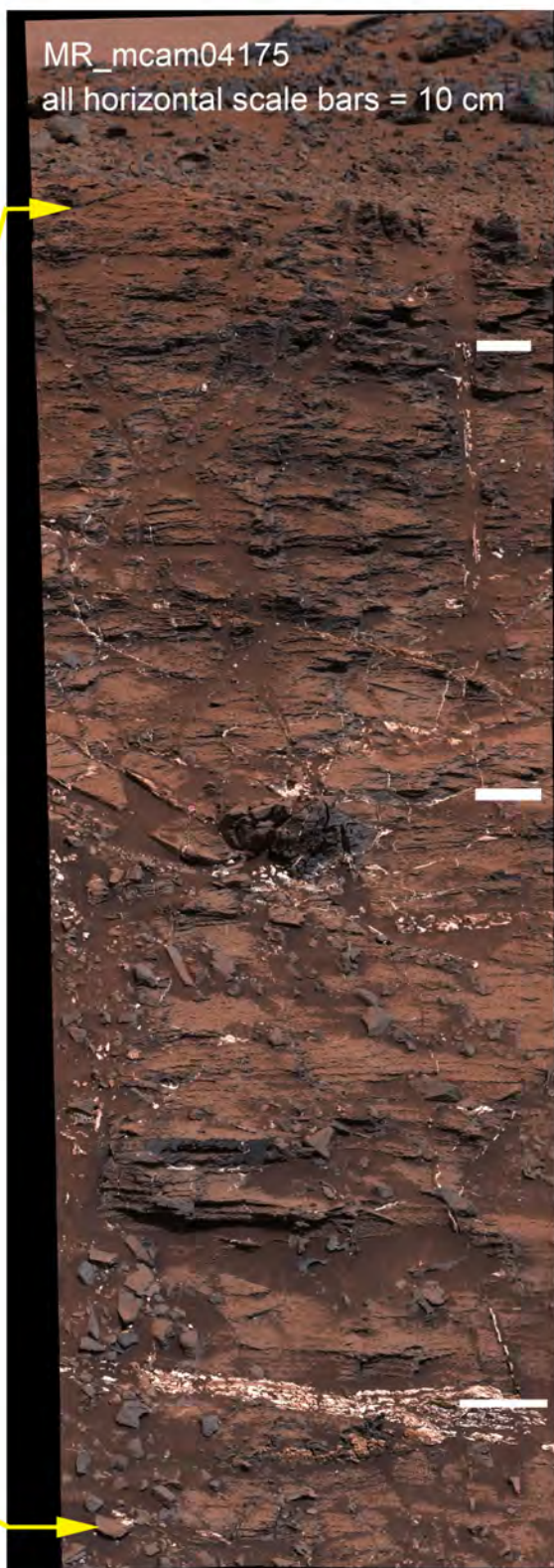
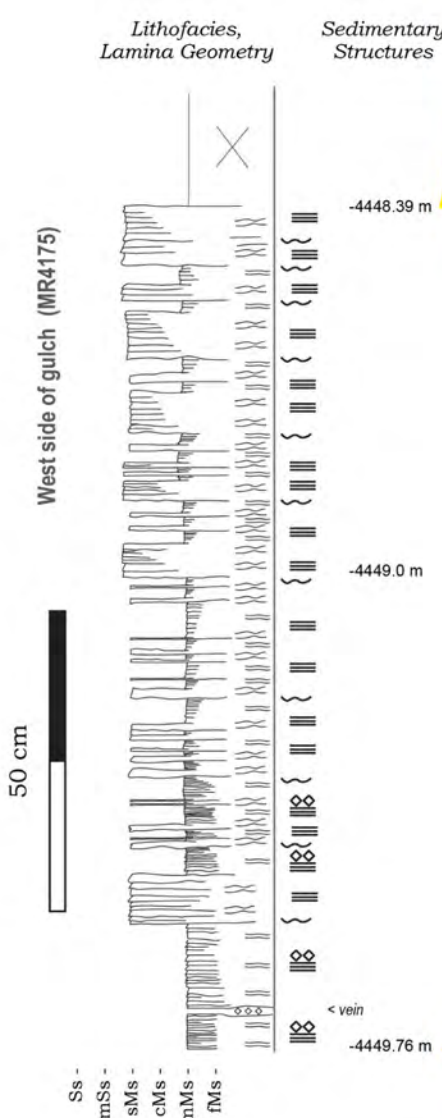
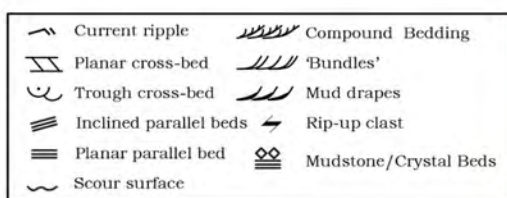


Fig. 27. Measured section of hackly weathering muddy sandstone facies (on left), derived from observations made on image mosaic MR_mcam04175. Legend for sedimentary features is shown at upper left.

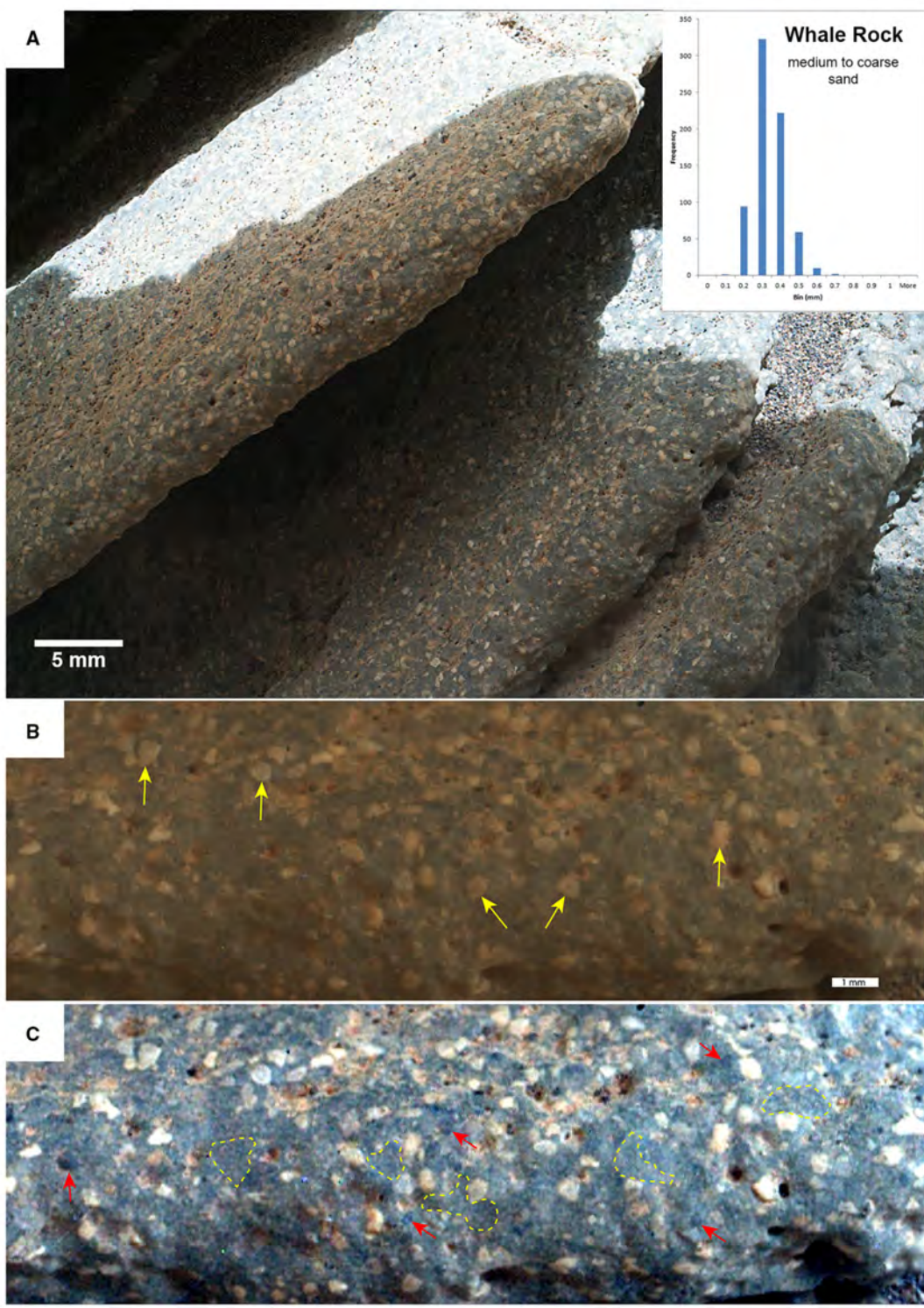


Fig. 28. (A) MAHLI image of a piece of Whale Rock sandstone (F5a) shows three resistant layers of sandstone with a speckled appearance. Inset shows size distribution of visible grains. (B) A closer view of the middle layer. This is the ‘as is’ MAHLI image. Yellow arrows mark likely plagioclase grains. (C) Enhanced (e.g. Lazar *et al.*, 2015) version of (B) that shows dark mafic grains (red arrows) and a fine-grained grey matrix between visible grains. In places that matrix has the appearance of deformed lumps (dashed yellow outlines), suggesting a mud rip-up clast origin. The rounded voids may have contained soft alteration products of labile minerals which were eroded upon outcrop exposure.

well-sorted (Fig. 28). Framework grains are probably feldspar (plagioclase), mafic minerals (pyroxene, olivine and magnetite) and rock fragments. Chemical analyses of Whale Rock float blocks (Thompson *et al.*, 2020) show F5a differing distinctly from the surrounding F1b mudstones (Fig. 5) and also from F5b (Salsberry Peak cap sandstone; Fig. 5). Unresolvable fine matrix between sand grains may mostly consist of mud rip-ups (Fig. 28C). Sedimentary structures include scour, planar-parallel beds, current ripples, planar-tabular and trough cross-beds, compound cross-beds with reactivation surfaces, foreset bundles, mud drapes and mud clasts (Figs 29 and 30).

Planar-parallel bedsets are of decimetre-thickness, and component laminae range from 1 to 10 mm thick (Fig. 29C). Current ripple laminasets are 3 to 11 cm thick and most common in the upper intervals of F5a bedsets (Fig. 29A). Planar-tabular and trough cross-beds range in thickness from 2 to 10 cm and are most common in the lower intervals of F5a bedsets. Compound cross-beds occur at two scales: 0.5 to 2.0 cm and 2 to 6 cm; curved foresets of the smaller scale lap down onto larger scale planar to curved foresets both obliquely and tangentially (Fig. 29A and B). Larger-scale foresets tend to truncate the tops of smaller-scale foresets. Both scales of foresets appear to have migrated in the same general direction at a relatively low angle of climb. Reactivation surfaces occur mainly within a 5 to 10 cm thick zone at the top of the compound-cross-bedded basal interval of Newspaper Rock and Whale Rock and have up to 3 cm of relief over 5 to 10 cm laterally (Fig. 29B).

Several F5 intervals contain foresets that vary quasi-systematically in thickness, weathering resistance and inclination. Bundles of thicker, more resistant and higher inclination foresets alternate with bundles of thinner, less resistant and lower inclination foresets (Fig. 30A and B) and are most common in the lower intervals of F5a bedsets. Isolated foresets in other intervals appear to consist of finer-grained material and are potentially mud drapes (Fig. 30).

Small mud clasts interpreted from MAHLI close-ups (Fig. 28C) tend to be larger than mineral grains and may exceed 1 mm in size. Another population of larger mud clasts is suggested by the shape and distribution of weathered voids (Fig. 30D and E). These presumed mud clasts are thin and flat, 4 to 24 mm long by 1 to 3 mm thick, occur along the horizontal part of sandstone foresets and are common in the lower intervals of F5a bedsets.

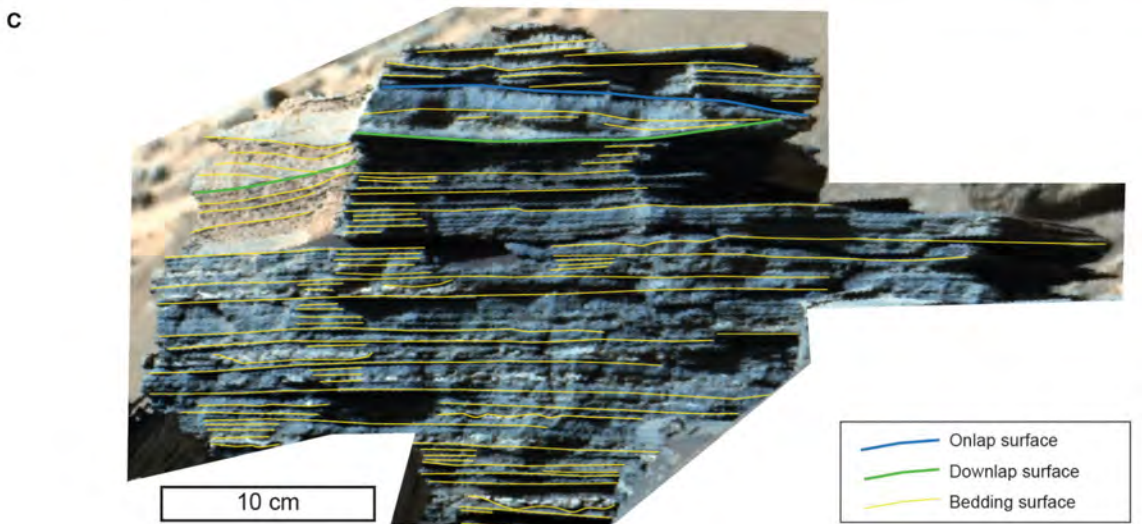
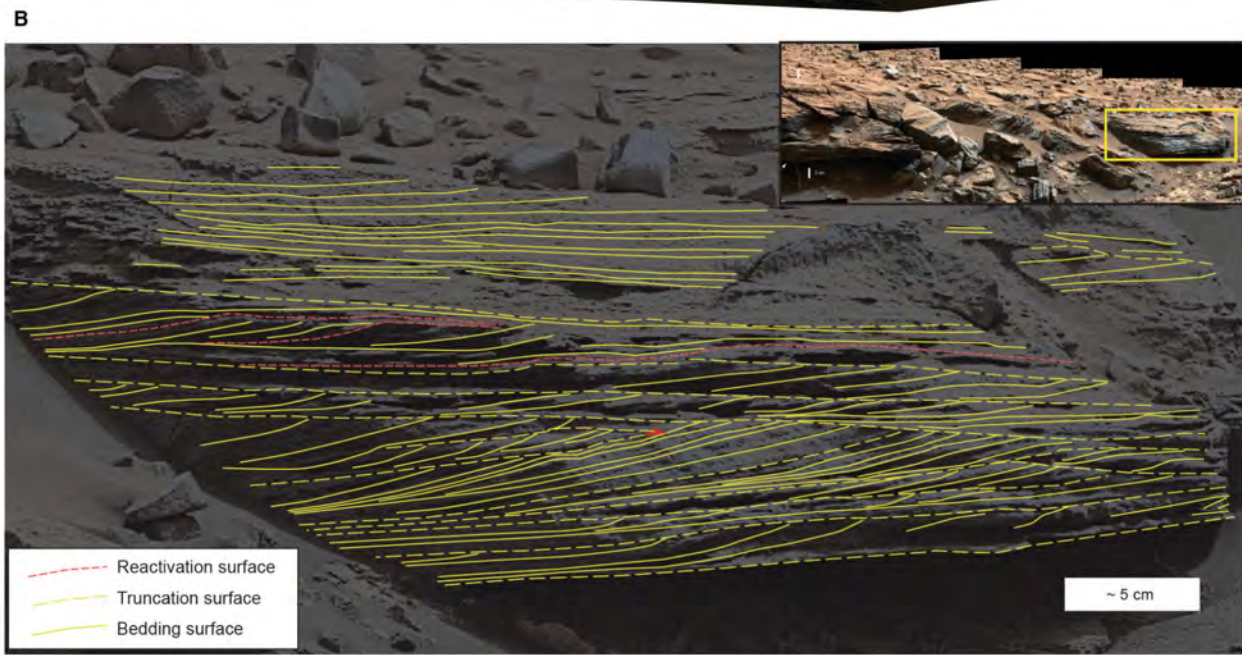
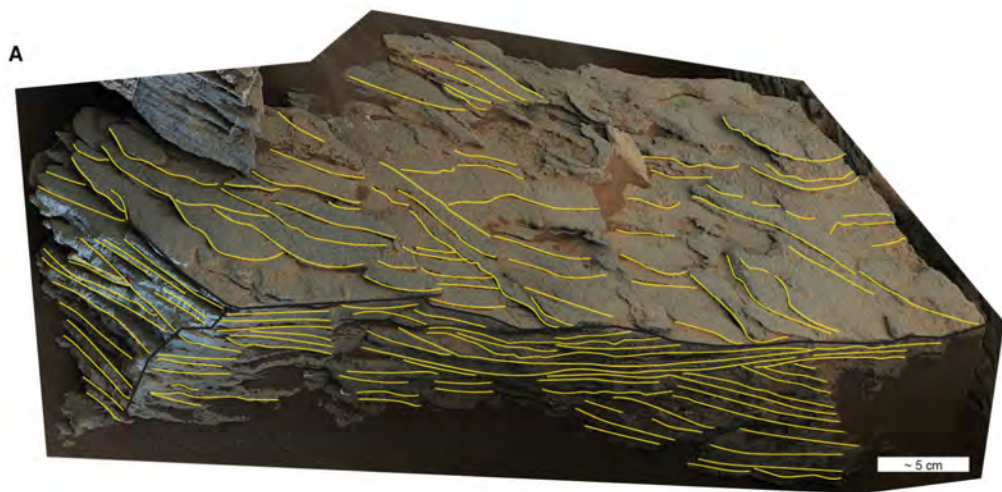
F5a sandstone lenses Newspaper Rock and Whale Rock were examined by Curiosity, and as many as nine additional occurrences are newly reported here (Figs 4 and 31). F5a lenses range from 2.7 to >7.0 m wide and 0.3 to 1.0 m thick, and have sharp bases and gradational tops. Upward, bedsets decrease in thickness and increase in width. The lower parts of exposures contain scour, mud clasts, flaser beds, mud drapes, foreset bundles of trough cross-beds and compound cross-beds (Fig. 31). The upper parts of exposures contain broader-scale scour, planar-tabular and trough cross-beds, and horizontal and inclined planar-parallel beds.

First order interpretation of F5a

The subangular to subrounded detrital grains of F5a were likely not very far travelled (less than tens of kilometres), judging by criteria that Folk (1980) lists for sands sourced from uplifted bedrock blocks on Earth. Because much of the potential provenance area had previously been affected by impacts, grains could have become rounded after only a few kilometres of transport because they had been ‘preprocessed’ (Arp *et al.*, 2019).

F5a strata fill channels that were incised into sublittoral F1b muds, consistent with incorporation of millimetre-scale to centimetre-scale mud clasts in these sandstones. These clasts (Fig. 30E) probably did not travel very far (on the order of hundreds of metres) and potentially had relatively high water content. Smaller, sand-sized mud clasts (Fig. 28C) probably travelled longer distances (kilometres to tens of kilometres), and record erosion of semi-consolidated F1b muds (Schieber, 2016). Eroded and transported mud clasts are common in terrestrial dryland fluvial strata (e.g. Nanson *et al.*, 1986; Müller *et al.*, 2004; Wright & Marriott, 2007). Mud drapes, foreset bundles and reactivation surfaces have all been reported from terrestrial lacustrine and fluvial strata (Appendix S11; Bradley, 1964; Tye & Coleman, 1989; Gierlowski-Kordesch & Kelts, 1994, 2000; Bohacs *et al.*, 2000; Cohen, 2003; Ainsworth *et al.*, 2012) and indicate alternating higher and lower flow velocities, though not necessarily on a regular period (Fraser & Hester, 1977; Alam *et al.*, 1985; Bye & Will, 1989).

Compound cross-bedding may indicate superimposed three-dimensional bedforms of two scales, both scales being stoss-erosional and lee-depositional, with a small net positive angle of climb, oriented dominantly transverse to



subordinately oblique to sediment-transport direction (*cf.* Rubin, 1987). Although feasible under either steady or unsteady flow (Allen, 1982; Middleton & Southard, 1984), bedform organization at this scale implies relatively steady uniform (and unidirectional) flow of many hours duration (Bohacs, 1981).

Mud clasts and drapes, foreset bundles and compound cross-beds in lower intervals are overlain by trough and planar-tabular cross-beds in upper intervals, a vertical succession that suggests an upward increase in stream flow persistence and decrease of suspended load relative to bedload. These conditions are in keeping with a fluvial channel setting characterized by commonly recurring, yet widely varying flows that were unsteady and intermittent in the basal intervals and relatively steady and persistent (days to weeks) in its upper intervals.

Laterally extensive cross-bedded sandstone – F5b

F5b is represented by the Salsberry Peak sandstone interval (4448.9 to 4448.0 m) that tops the exposure, is at least 10 m wide and close to 2 m thick (Figs 4 and 5) and has correlative rocks on the west side of Artists Drive (Fig. 4). F5b is underlain by F4 (Fig. 32), a facies that is gradational upward, with sandstone bedsets that thicken upward towards the cap sandstone. F5b contains moderately well-sorted discernible grains that range in size from 140 µm up to 750 µm (Fig. 33B), and are sub-rounded to well-rounded, with mostly spherical grains (Fig. 33).

The clear visual contrast between F5a and F5b (Fig. 33) is corroborated by contrasting chemical composition. Analyses from a piece of Salsberry Peak float, the Kanosh boulder (Fig. 5), show distinct differences to F5a (Whale Rock).

Sedimentary structures are subtly expressed and include scours, current ripples and planar-parallel beds, with sparse trough cross-beds and compound cross-beds (Fig. 32). Compound and trough cross-beds are less abundant than in F5a. Scours and current-ripple beds dominate the basal 30 cm of the Salsberry Peak exposure. The

superjacent 50 cm contain abundant scours and a mix of current ripple beds, trough and planar tabular cross-beds, and planar-parallel beds. The uppermost portions of this sandstone unit are discontinuously exposed in large blocks at the top of the hill.

First order interpretation of F4 and F5b

F4 is interpreted as recording strong sand-laden flows alternating with low flow conditions and mud accumulation (Middleton & Southard, 1984). The more resistant bedsets (above ~4448.1 m) may represent upper-flow-regime planar-parallel beds resulting from river floods generating sediment-gravity flows (Middleton & Southard, 1984; Bhattacharya, 2010). Interbedded mudstones are hypothesized to be similar to F1b, recording the falling limbs of flood hydrographs and background sedimentation. The apparent thickening and coarsening upward towards the overlying Salsberry Peak sandstone (Fig. 32) suggests an overall increase in coarse sediment influx, sedimentation rate and benthic-energy levels. F4 is interpreted as a river-dominated distal to medial delta front, fed by one or more variable discharge streams that prograded into relatively shallow lake waters.

F5b clearly differs from F5a, as indicated by contrasting chemical composition (Fig. 5) and visual appearance (Fig. 33), probably due to origin and transport history. Bedload under unidirectional flows was the dominant mode of sediment transport. The lower interval of F5b records multiple episodic flows that waned rapidly. The upper interval records flows of variable strength and duration, suggesting the influence of intermittent streams. Flows were sufficiently persistent in some intervals to make larger-scale bedforms (trough and planar-tabular cross-beds), sufficiently strong to generate planar-parallel beds in other intervals, and only capable of forming small-scale bedforms (current ripples) in still others. The blocky weathering top portion (*ca* 75 cm) presumably was deposited under comparable

Fig. 29. Variety of bedding types in F5a. (A) Longitudinal, transverse and bedding-plane views of cross-beds (Whale Rock, MR_mcam03736, rotated from original image). Yellow lines outline exposed foresets on the top of the block, and cross-bedding on the vertical sides of the block. (B) Longitudinal view of compound cross-beds, truncation and reactivation surfaces (Whale Rock, MR_mcam03736). Note two scales of bedsets: 0.5 to 2.0 cm and 2 to 6 cm. (C) Planar-parallel beds, Newspaper Rock interval (MR_mcam03951). Planar-parallel beds are 1 to 3 cm thick; their component laminae range from 1 to 10 mm thick with an average thickness of 3.4 mm. A non-interpreted (no yellow tracings) version of this figure can be found in Appendix S5A.

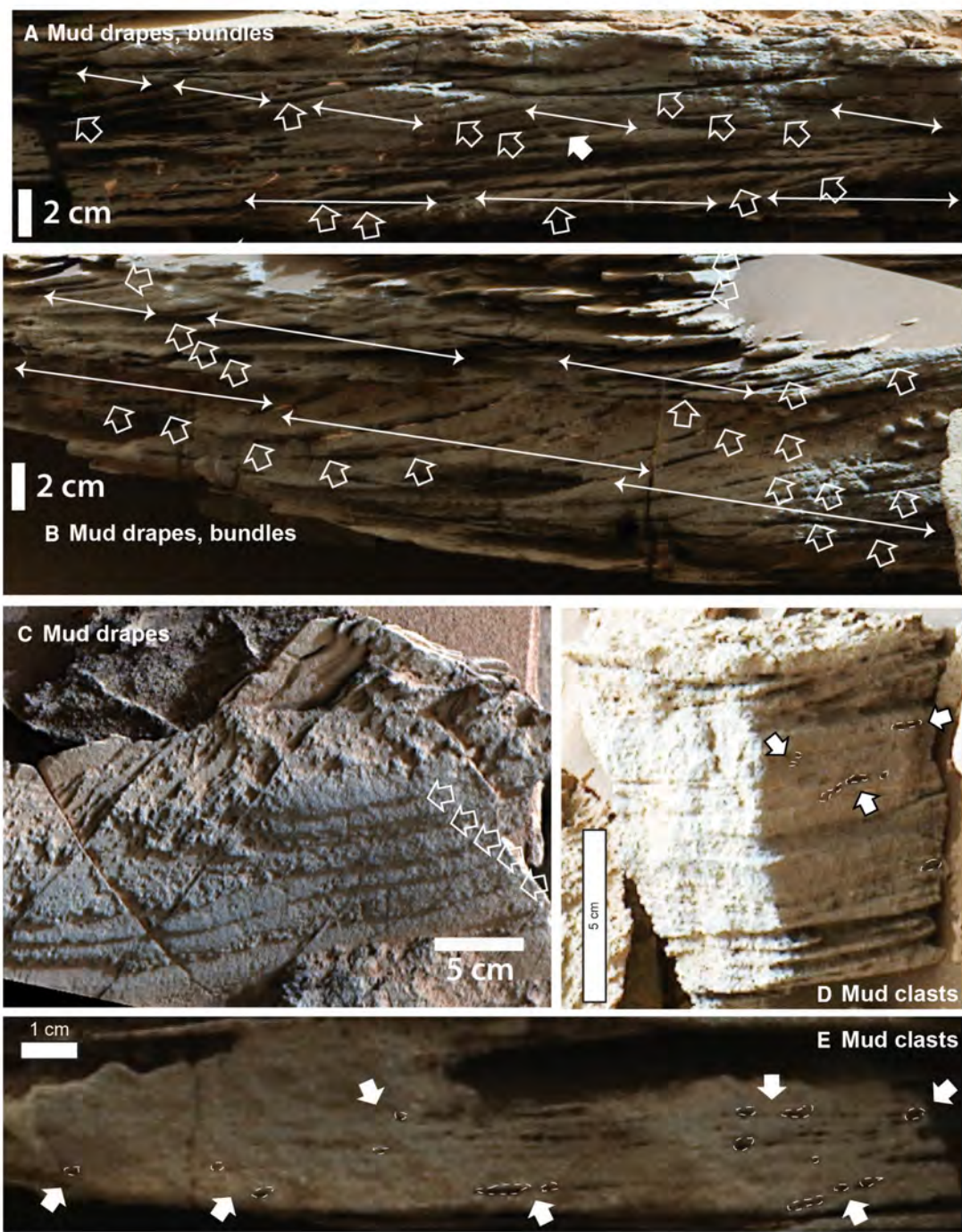


Fig. 30. F5a bedding character. (A) and (B) Examples of mud drapes (open arrows) and foreset bundles (double-headed arrows) in vertical profile at Whale Rock (MR_mcam03476). Foreset bundles are defined by systematic thickening and thinning of intervening mud drapes and changes in foreset dip angle laterally. Note occurrence of drapes and bundles in several vertically stacked beds. (C) Mud drapes (open arrows) on an oblique to bedding plane broken surface, Newspaper Rock (MR_mcam03481). Note stepped relief on fracture surface and differential weathering between coarser and finer grained layers. (D) and (E) Interpreted mud clasts based on shape and distribution of weathered voids in sandstone, Whale Rock (MR_mcam03476). Presumed mud clasts were thin and flat, 4 to 24 mm long by 1 to 3 mm wide and occur along the horizontal part of sandstone foresets. See Fig. 28 for preserved mud clasts and Appendix S11 for examples of foreset bundles and mud drapes from lacustrine strata on Earth.

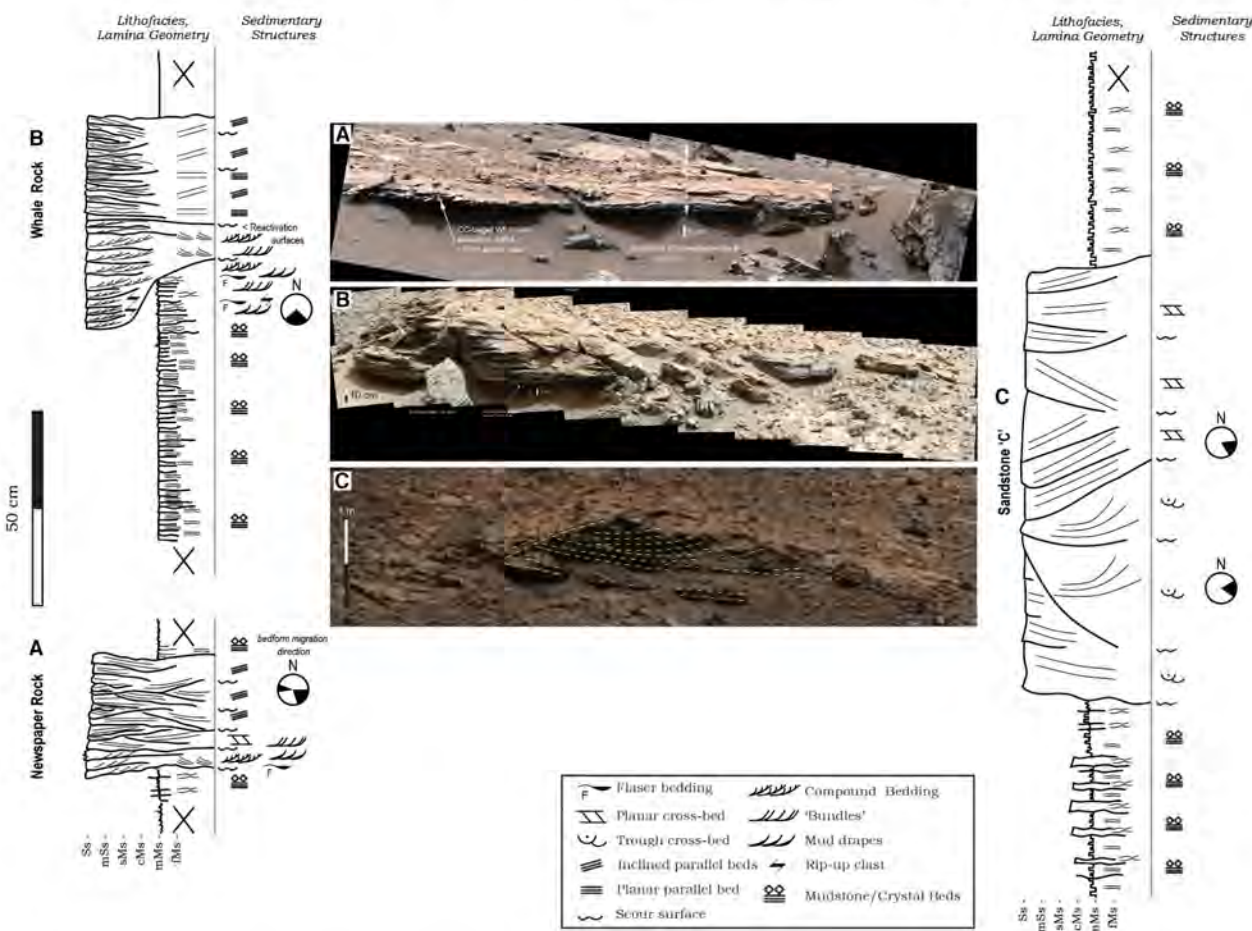


Fig. 31. Outcrops of laterally isolated cross-bedded sandstone facies (F5a). (A) Newspaper Rock (MR_mcam03481). (B) Whale Rock (MR_mcam03476). (C) Sandstone 'C' (Fig. 4; MR_mcam03232). Detailed measured sections of laterally isolated cross-bedded sandstone facies were traced and interpreted from MastCam images. Left columns document lithofacies, grain size, lamina geometries and bed surfaces. Right columns document sedimentary structures: black quadrants in circles indicate directions of bedform migration inferred from lamina geometries; N indicates north. A non-interpreted (yellow dashed lines) image of sandstone C can be found in Fig. 4, Inset 3.

conditions. Laterally discontinuous recessive layers that potentially represent mud-rich lenses are present throughout the 165 cm vertical span of continuous outcrop and suggest that slack-water periods were relatively common.

F4 and the conformably overlying F5b are interpreted as a shoaling-upward succession from distal to proximal delta front and stream-mouth bar areas of a river-dominated delta fed by intermittent streams. Stream flows, although somewhat variable, were more persistent than for F5a and overall discharge was larger (see **Facies and Stratigraphic Succession**). The stratigraphic thickness of F4 to F5b does not directly relate to water depth because lake shorelines can regress by a combination of progradation

and lake-level fall (Bohacs *et al.*, 2000). Thickening-upward and coarsening-upward stratal successions and abrupt vertical transition among depositional sub-environments as seen here are characteristic of river-dominated shoreline strata in lacustrine systems on Earth (e.g. Gierlowski-Kordesch & Kelts, 1994, 2000; Renaut & Gierlowski-Kordesch, 2010), as seen, for example, in modern-day Lake Bogoria (Appendix S12).

Stratigraphic distribution of facies and stratigraphic surfaces

Figure 34 documents distribution of Pahrump Hills facies types in a composite stratigraphic section compiled from observations along the

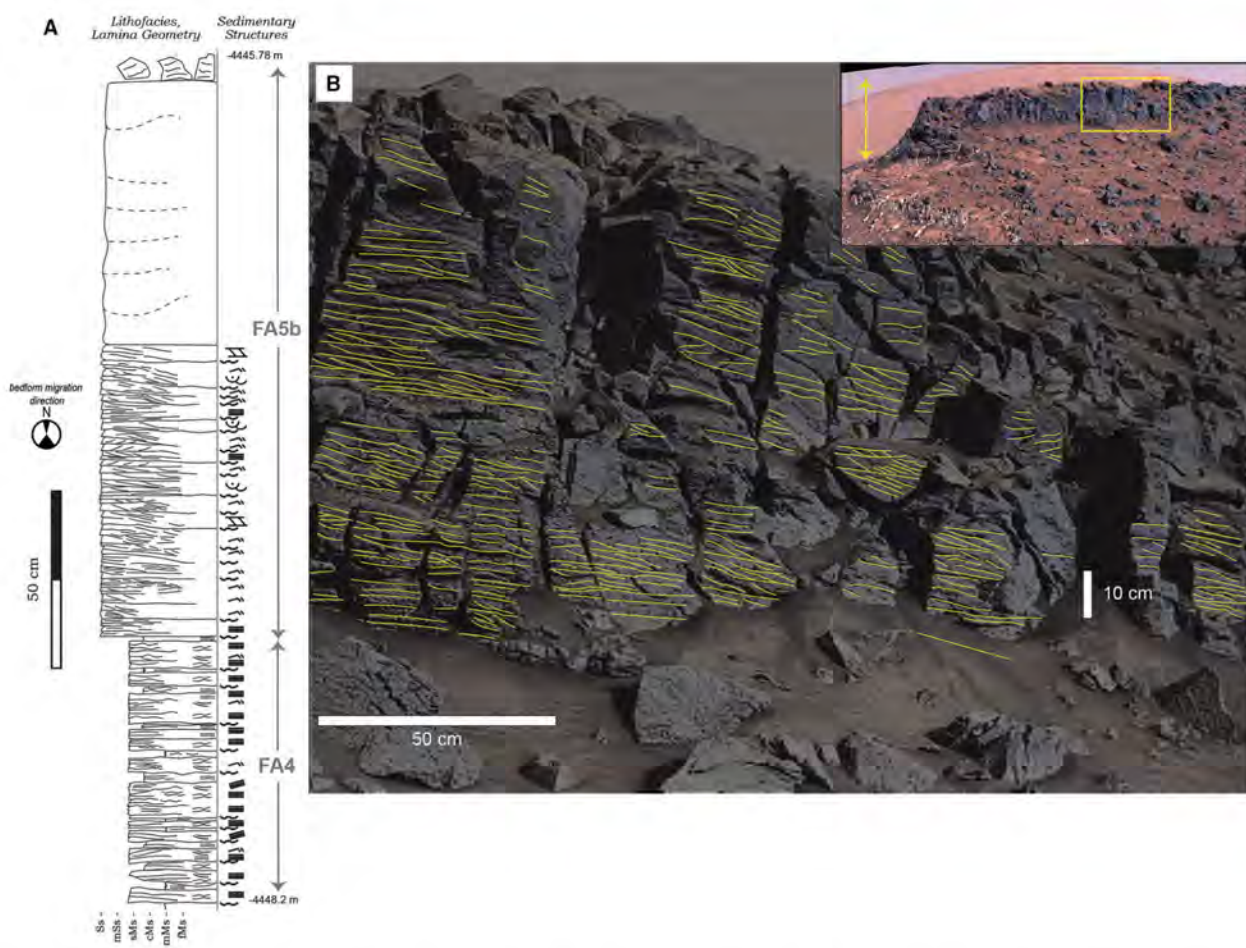


Fig. 32. Laterally extensive sandstone facies, F5b, the Salsberry Peak interval (−4447.6 to −4446.2 m). (A) Measured section traced and interpreted from MastCam mosaic MR_mciam04117 (upper right inset). The section extent is marked by the yellow double-head arrow in the upper right inset image and includes the underlying F4 interval (Fig. 27). Left column documents lithofacies, grain size, lamina geometries and bed surfaces. Right column documents sedimentary structures. Black quadrants in circles indicate directions of bedform migration inferred from cross-bedding. (B) Outcrop image, from MR_mciam04119 (yellow frame in upper right inset). The lower 0.83 m of the 1.7 m thick sandstone cap are continuously exposed in vertical profile and the upper 0.87 m occur as large blocks at the top of the hill.

rover traverse. It also contains placement of sedimentological observations and target names referred to in the text.

Facies types occur in organized succession and recurring relations. The basal 6.2 m of the section contain F1a mudstones interbedded with multiple decimetre-thick F2 ledges (Fig. 34) and also contains flat to oblate–spheroidal concretions and dendrites. Strata in this interval vary systematically in several thickening-upward and coarsening-upward metre-scale successions, from a sharp-based interval of F1a mudstone with few scours, upward through F1a strata with increasingly common scours, thicker layers and

cemented zones that increase in thickness and lateral extent, overlain transitionally by F2 strata with abundant scours, current-formed bedding and the thickest layers in the succession. Mg content increases upward within these metre-scale F1a to F2 successions (Fig. 7). F2 horizons increase systematically in thickness towards Book Cliffs and subsequently decrease farther upsection. Current ripples due to wave action and wind driven circulation (see F3), erosion surfaces, and downlapping and onlapping laminae are most common in the Book Cliffs interval of F2. Several geochemical trends parallel these changes (Fig. 5). FeO_T decreases towards Book

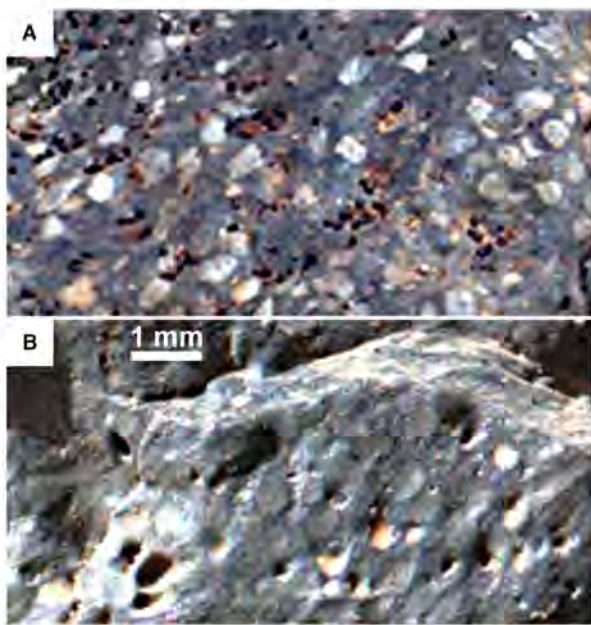


Fig. 33. Comparison of MAHLI images (same scale) of F5a at Whale Rock (A) with F5b float block Kanosh from the Salsberry Peak sandstone (B). In (A) light-coloured feldspars are easily recognized, and mafic mineral grains are obscured by the similar coloured mud rip-up clasts (Fig. 28). In (B) the depressions may be sites of now weathered-out feldspar grains, and discernible sand grains seem to be either basaltic rock fragments or mafic minerals. Note high degree of rounding of sand grains.

Cliffs and increases above, whereas MgO, Al₂O₃, Cl and Br have maxima at Book Cliffs and decrease in the F1a strata above.

This basal part of the succession is capped by an undulose erosion surface that is onlapped by as much as 40 cm of F3 (Chinle interval). Above follow about 6 m of F1b mudstones, which in its lower 3 m contain lenses of cross-bedded sandstone (F5a, 30 to 100 cm thick). The F1b mudstone interval is overlain conformably by sandy mudstone and muddy sandstone strata (F4), and laterally extensive F5b sandstone (Salsberry Peak). Above Chinle, stratal organization of facies at the decimetre-scale to metre-scale like seen below (F1a to F2 successions) is not apparent. Chemical and mineral data (Fig. 5; Table 2), such as a different feldspar assemblage and higher SiO₂ concentrations, indicate a significant change between F1a and F1b.

The physical stratigraphy of Pahrump is mirrored by mineralogical and geochemical changes at several vertical scales (see *Compositional data and inferences*). Most significantly,

mineralogical (Table 2) and geochemical data (Figs 5 to 7) fully support the split into a lower and upper subdivision at the Chinle unconformity (Figs 2 and 4). Oligoclase, sanidine, augite, ilmenite and orthopyroxene are observed below Chinle, whereas albite, anorthoclase, cristobalite and tridymite are only observed above Chinle (Table 2). Significantly higher Na₂O and SiO₂ concentrations were measured by APXS (Fig. 5) and ChemCam in the strata above Chinle. APXS data (Fig. 5; Appendix S4) show a systematic compositional difference between the lower and upper successions for TiO₂ and P₂O₅ (higher concentrations) and Al₂O₃, MgO, CaO, SO₃ and Ni (lower concentrations), as do the ChemCam data from bedrock targets. The composition of the half metre of F3 on top of the Chinle unconformity generally overlaps with that of underlying strata and suggests that its particles were eroded from the underlying mudstone succession (F1b, F2). Increased Na, and lower Al and Ca concentrations also agree with the different feldspar content of F1a at TP (albite, no oligoclase) versus F1b (as well as F2). Because the TP drill sample has an olivine content comparable to CH and TP, lower Mg is not associated with changes in forsteritic olivine content, but rather with lower augite content (consistent with low Ca concentrations). Significantly higher Ti concentrations in the bedrock targets above Chinle (F1b) are attributed to higher maghemite in the TP drill sample as well as a higher TiO₂ within the amorphous component. Maghemite is interpreted to be partially oxidized detrital magnetite. Additional support for the lower–upper subdivision comes from plotting chemical abundances relative to an arbitrary reference stratum and monitoring which elements show relative increases/decreases going upsection (Appendix S4). All lines of evidence, therefore, point to a ‘reset’ at the Chinle level with regard to inferred environments of deposition, landscape organization, salinity history and magnitude of lake level fluctuations.

INTEGRATION AND INTERPRETATION OF OBSERVATIONS IN A SEQUENCE STRATIGRAPHIC CONTEXT

Sequence stratigraphy and depositional history

Sequence stratigraphy allows construction of a comprehensive chronostratigraphic framework

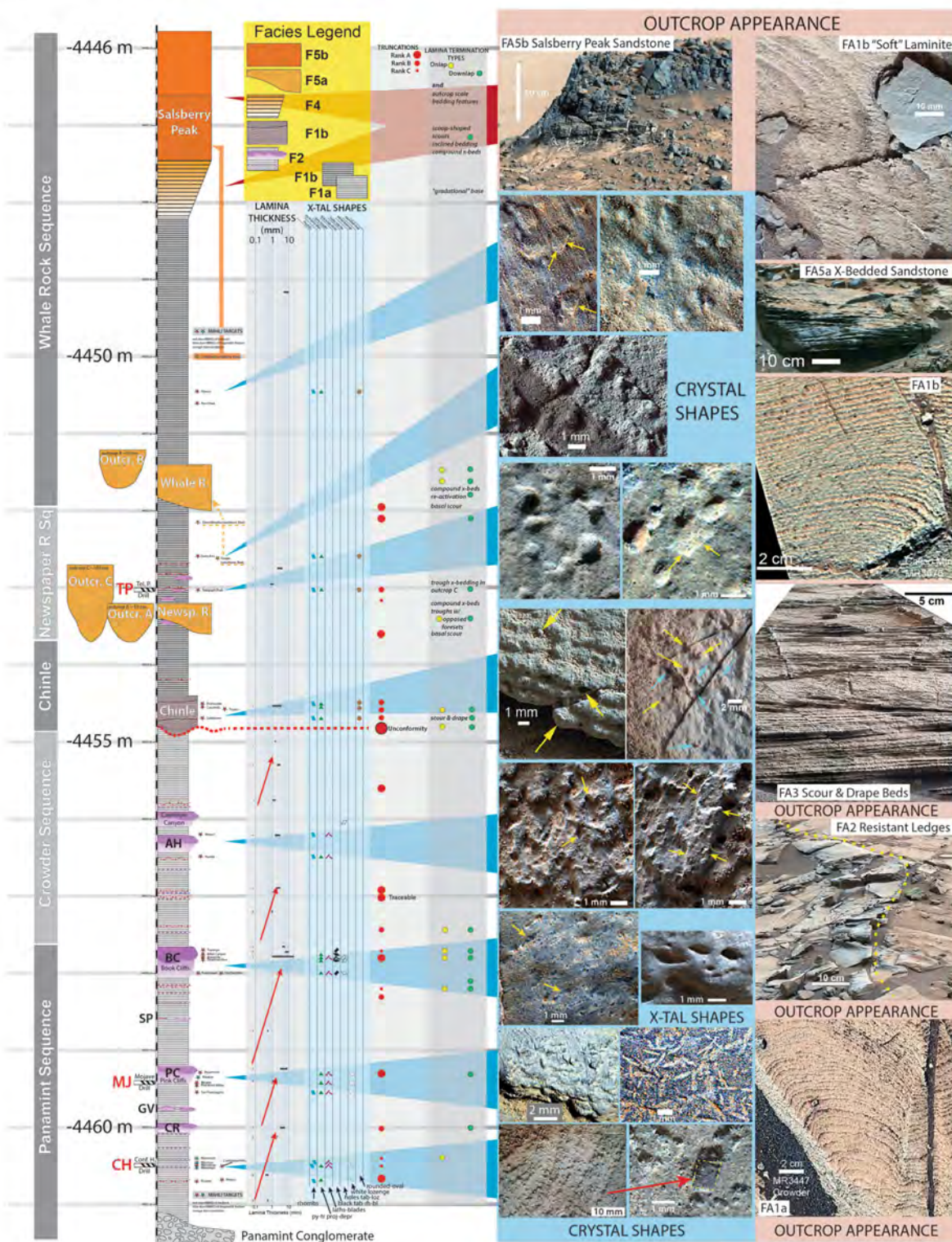


Fig. 34. Composite stratigraphic section of the Pahrump Hills area. Shows the vertical distribution of facies, layer thickness and crystal pseudomorph types as well as outcrop appearance of facies. This figure is available in higher resolution in Appendix S6. CH = Confidence Hills; MJ = Mojave; TP = Telegraph Peak; CR = Comb Ridge; GV = Gold Valley; PC = Pink Cliffs; SP = Saddle Peak; BC = Book Cliffs; AH = Alexander Hills (includes Carnivore Canyon).

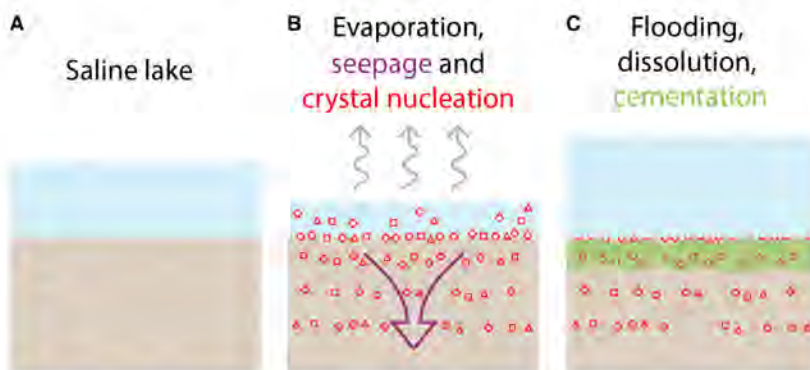


Fig. 35. Schematic representation of the accumulation of evaporite minerals at the lamina to bedset scale. (A) Flooding in saline lake delivers detrital fines. (B) Evaporation leads to formation of a variety of cumulate and bottom-growth evaporites (filled red diamonds, squares and triangles) as well as dense benthic brines that seep into the sediment and form sediment-incorporative crystals intrastratally (open red diamonds, squares and triangles). (C) Subsequent flooding and cooling dissolves most of the cumulate and bottom-growth evaporites. Prolonged residence of pore waters leads to formation of intrastratal cements such as opal-CT, Fe-oxides, and allophane/imogolite (green ellipses and zone).

based on a single criterion – the physical relations of the strata themselves – that reveals genetically related rocks. A comprehensive sequence-stratigraphic framework facilitates integrating all types of data, from kilometre-scale to metre-scale orbital images and spectroscopy, through metre-scale to centimetre-scale outcrop images and analyses, to millimetre-scale images and geochemical analyses (Appendix S13 details the construction of this framework). The main building blocks of the stratigraphic record are depositional sequences composed of parasequences made of beds and bedsets (e.g. Mitchum & Vail, 1977; Van Wagoner *et al.*, 1988; Bohacs, 1998; Abreu *et al.*, 2010), with recognized stratal patterns widely recurrent and therefore predictable.

Lamina to bedset scale

The processes that controlled formation of smaller scale layering (millimetre-scale) are outlined in the section *First order interpretation of F1*. Softer layers record detrital fines carried into the lake by episodic floods and runoff events, whereas harder layers reflect lake floor cumulates and bottom growth of evaporite minerals that subsequently underwent partial dissolution and reprecipitation as sediment-incorporative crystals (now pseudomorphed; Fig. 35).

Bedset to parasequence scale

Bedset to parasequence scale bedding is best expressed below Chinle as recurrent decimetre-

scale to metre-scale shallowing-upward successions (Fig. 34), interpreted as parasequences. Lower intervals of these typically are relatively soft and composed of F1a without large nodules or cemented horizons. Upward within each parasequence, horizontal F1a bedding is more commonly interrupted by scours and truncations, and contains downlapping lamina, thicker layers and scattered small nodules. In the uppermost intervals, truncation surfaces are most common, layers are even thicker, and nodules are larger and more laterally extensive. Upward increase in softer-harder layer thickness serves as a proxy for shoreline regression. Parasequence top portions show laterally extensive nodules or stratiform cementation and sedimentary structures (scours, ripples) indicating wave-induced current reworking of lake-floor muds (F2). Parasequences record initial flooding (water depth increases) and transgression (landward retreat) of the lake shoreline, followed by a 'ratchet-like' fall of lake level and regression (basinward migration) of the lake shoreline, mostly by withdrawal of lake waters with relatively minor progradation. Lake level varied up and down fairly regularly at the shorter time-scale but with a longer-term overall falling trend (Fig. 36).

The upward increase in abundance and volume of nodules and cemented horizons implies parallel increases in duration of evaporation/concentration interludes, an inference supported by the observed upward increase of MgO within each

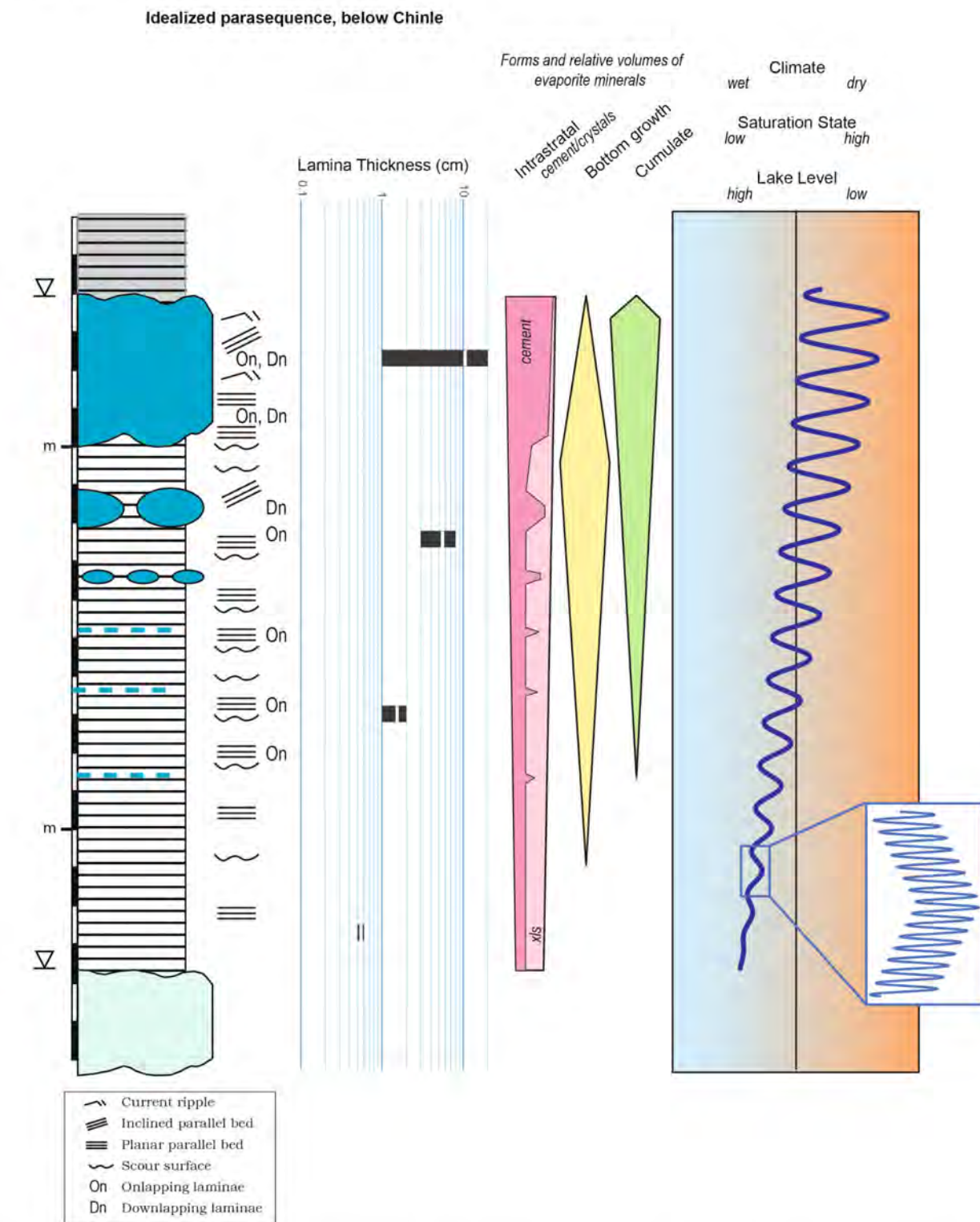


Fig. 36. Schematic depiction of an idealized parasequence in the lower half of the succession. Mudstone layers are thinner upward, crystal pseudomorph layers are more closely spaced, and cemented layers and concretions are better developed upward. Mudstone-crystal pseudomorph couplets record short-term wet-dry periods whereas parasequences record longer-term flooding and subsequently more frequent dry periods, and overall more evaporative and saline conditions.

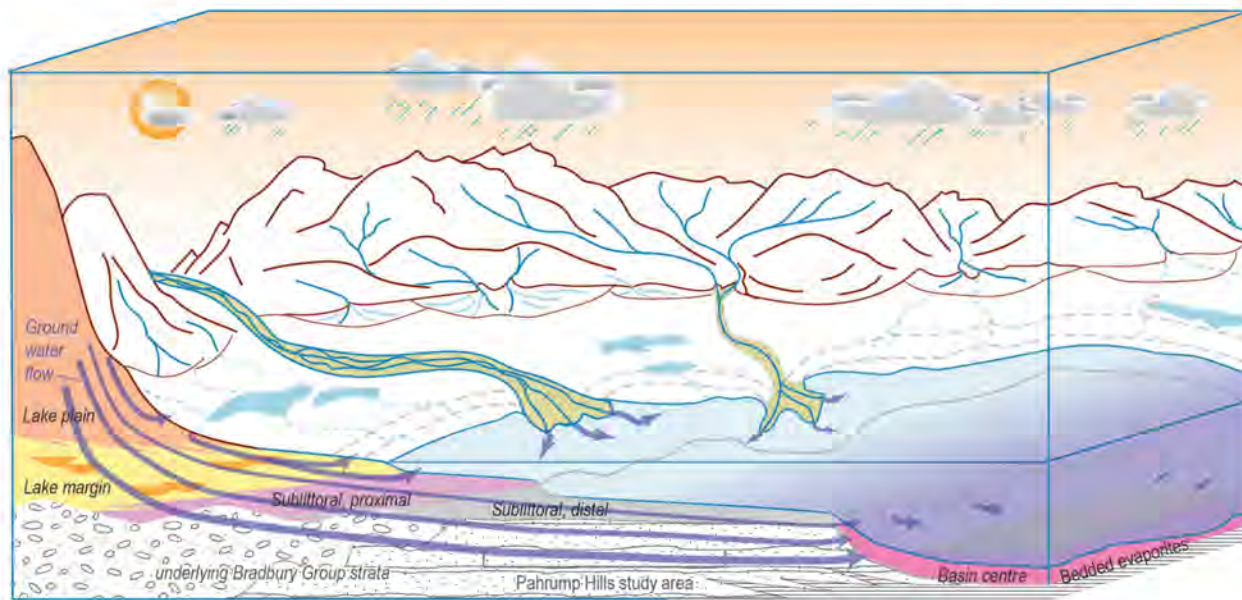


Fig. 37. Depositional setting of the Pahrump Hills succession in the context of a larger lake system. Water supply to the lake was by a combination of short and long rivers and groundwater flow that discharged both subaerially and subaqueously (blue arrows). Bedded evaporites are restricted to central portions of the lake. The figure depicts system components, not a specific point in time of lake basin evolution.

parasequence (Fig. 7). Likewise, an upward increase in pseudomorph variability (Fig. 34) points to increasing mineral diversity due to more widely varying salinities that trended to higher end-point salinities overall (Fig. 36). The parasequence tops probably record very shallow water (decimetre to centimetre; Fig. 20) or even sub-aerial exposure (albeit with a high-water table/saturated pore waters). A lack of bedded evaporites at Pahrump can be explained by the lateral position of these strata towards the margin of a larger lake basin (Fig. 37). Bedded evaporites (Fig. 37) would have formed in remnant brine pools in the basin centre, sustained by groundwater discharge (*cf.* Rosen, 1994, on playa lakes, Fig. 2; Bohacs *et al.*, 2000, 2007). Evaporation (salinity increase) seldom, if ever, led to complete desiccation and bittern-salt/chloride precipitation, based on the occurrence of such features as Potatoe and Searles (Fig. 22) and constraints on allophane/imogolite accumulation described below. Instead, the lake and pore waters were episodically resupplied with fresher water and additional solutes.

Resistant ledges of smooth-weathering mudstone (F2) record highly evaporative, shallow near-shore conditions at the culmination of each parasequence. Decreasing pH in lake and pore waters as solute concentration increased upward

in each parasequence would have led to mobilization of more Al in surficial sediments (Parfitt & Kimble, 1989). During parasequence culmination, *in situ* weathering of olivine in surficial sediments could have raised pore water pH sufficiently to precipitate allophane and lead to hardened horizons of F2. Thus, the F1 to F2 lithological successions of parasequences below Chinle (Fig. 34) are a logical consequence of changing energy and solute levels due to initial expansion and subsequent contraction of the lake.

Above Chinle, bedrock observations are stratigraphically discontinuous, hampering the definition of parasequences. In the uppermost interval above -4448.2 m, however, the succession from F4 to F5b (Figs 32 to 34) at Salsberry Peak is interpreted as a parasequence dominated by clastic progradation.

Parasequence set to depositional-sequence set scale

The largest scale of bedding considered here is the metre-scale to decametre-scale of parasequence sets and depositional sequences. The parasequence stacking patterns and key surfaces recognized at Pahrump, and their correlation to outcrops farther north (Fig. 38) provided key insights into the sequence stratigraphy and depositional history of the area.



Fig. 38. Index map showing location of outcrops (yellow boxes) and their projection into the lines of the north-east/south-west and north-west/south-east cross-sections (yellow and orange lines) shown in Fig. 39 and Appendix S13, respectively. Rover track shown by grey curved line with a subset of rover locations (blue circles) and Sol numbers. Ss, sandstone.

The nominal base of the Pahrump Hills section (*ca* –4461.0 m) contains conglomerate, sandstone and mudstone. Conglomeratic strata, designated herein as the Panamint conglomerate (Fig. 34), appear to overlie deltaic strata of the upper Bradbury group (Fig. 2) and underlie all of the rocks examined in the study area (Grotzinger *et al.*, 2015). The top of the conglomerate varies in elevation by about 1.5 m across the area (Fig. 39; Appendix S13) and is overlain by sandstone in most places. Mudstone-dominated strata overlie the Panamint conglomerate at north-east, east and south-east Panamint, with the maximum northern (i.e. updip/landward) extent of mudstone at north-east Panamint. These mudstones appear to coarsen and thicken upward into sandstone bedsets, locally expressed as progradationally stacked parasequences (Appendix S13). The lowermost two mudstone to sandstone parasequences appear to lap on or lap down onto the top of the Panamint conglomerate (Fig. 39; Appendix S13).

Because the base of the Panamint conglomerate could not be examined, its sequence stratigraphic characteristics were inferred via its relation to immediately overlying strata and by comparing to analogous lake systems on Earth, concluding that the sequence boundary (SB)/unconformity and transgressive surface (TS) of the basal depositional sequence (informally named the Panamint Depositional Sequence; Fig. 34) coincides with the base of the Panamint conglomerate – analogous to the surface atop Book Cliffs (Fig. 39), as described below.

Depositional sequences were named after units or features near the base, the standard practice on Earth (Abreu *et al.*, 2010). The uneven upper surface of the Panamint conglomerate is considered an original depositional feature, reflecting gravel barforms that formed as sediment and water supply rates increased during the transgressive systems tract (TST), a feature characteristic of closed hydrography lake basins (Bohacs *et al.*, 2003). The lowstand systems tract (LST) of the Panamint Depositional Sequence presumably occurs more distally and laps out south of the study area. Such laterally displaced LSTs are not uncommon in balanced-fill and underfilled lake basins (Bohacs *et al.*, 2000; Renaut & Gierlowski-Kordesch, 2010). The Wilkins Peak member of the Green River Formation (south-east Wyoming, Bohacs *et al.*, 2007, Fig. 11) provides an Earth analogue, where bedded evaporite LSTs lap on 8 to >27 km basinward of the pebbly sandstones of their TSTs. Thus, bedded evaporites potentially coeval with Pahrump Hills strata may well be buried beneath Aeolis Mons to the south. A maximum flooding surface (MFS) is interpreted at the top of the Panamint conglomerate, the level at which mudstone strata extend the farthest to the north and north-west (up transport direction/landward) and above which stratal stacking becomes progradational (Fig. 39). Basal convergence and inferred onlap at the Upheaval Dome outcrop (and elsewhere) provide further support for this MFS placement (Appendix S13).

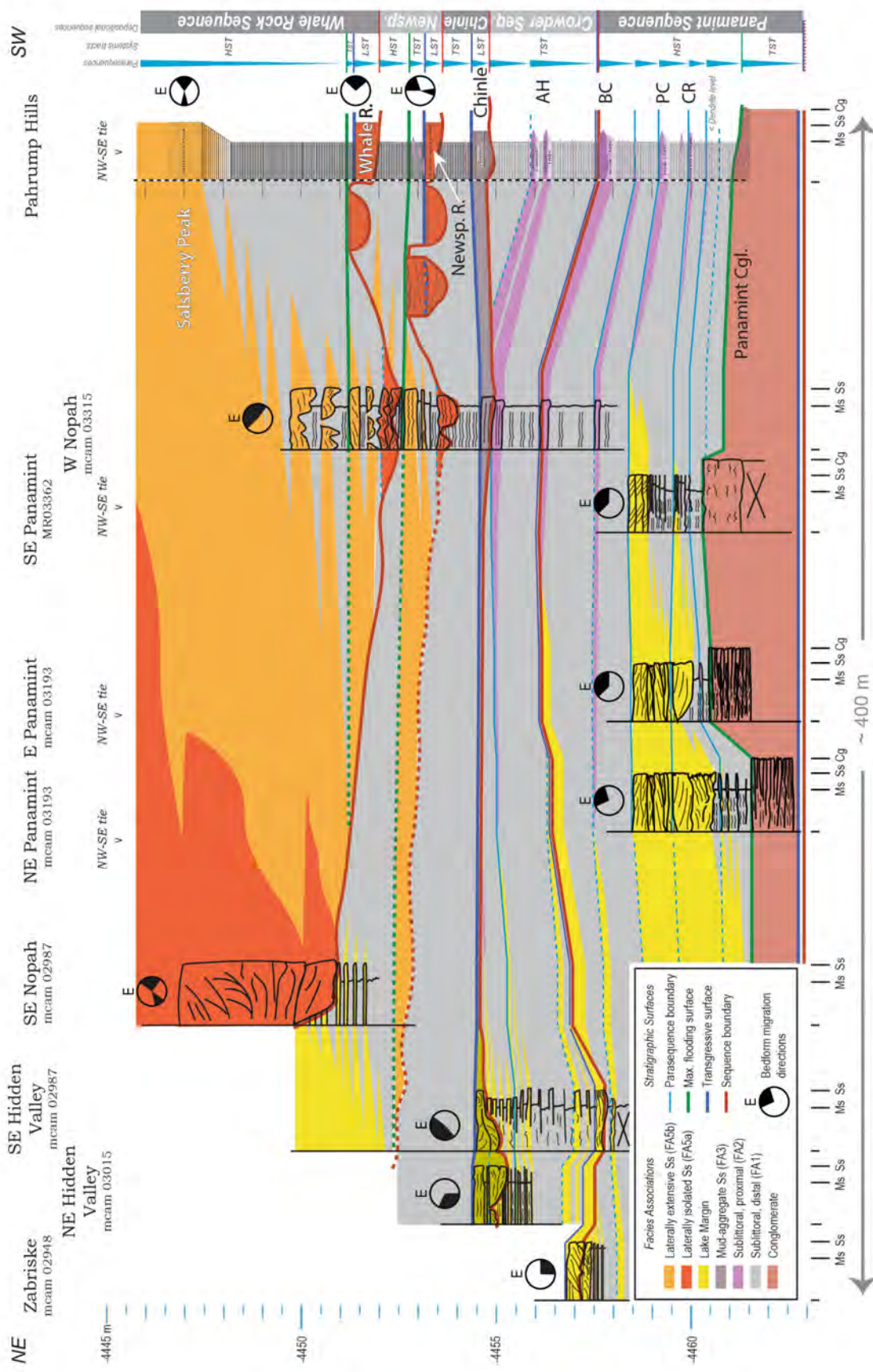


Fig. 39. Stratigraphic cross-section oriented from north-east to south-west, generally along depositional dip, showing laterally equivalent strata of the Pahrump Hills section and interpreted depositional environments and sequence stratigraphic framework. Blue triangles, parasequences; MFS, maximum flooding surface; SB, sequence boundary; TS, transgressive surface.

From the base of the Pahrump Hills main section (Fig. 34; -4461 m) to the top of Book Cliffs (-4457.6 m) parasequences stack progradationally (Figs 34 and 39). Each successive parasequence records more proximal (shallower water) conditions, and the interval is considered a highstand systems tract (HST). Parasequence boundaries (flooding surfaces) in this interval can be traced laterally for tens of metres in outcrop panoramas (Fig. 4) and can be correlated to multiple outcrops to the north and west of the main Pahrump section (Fig. 34) across approximately $90\,000\,\text{m}^2$ (Fig. 39; Appendix S13). Parasequence boundaries dip south at about 0.15 degrees, are generally parallel to one another, and suggest relatively stable bathymetric profiles.

The surface atop Book Cliffs (Figs 21B and 34) appears unconformable to the north-east and overlain by aggradational cross-bedded and planar-parallel sandstone at south-east Hidden Valley and Zabriskie (Fig. 39). Thus, the upper surface of the Book Cliffs F2 ledge is considered a SB that is directly overlain by the TS of the Crowder Depositional Sequence. As surmised for the Panamint Sequence, LST strata associated with this SB presumably occur distally (deepest part of lake) and lap onto the SB south of the study area. The local record of this LST is the extensive cementation and authigenesis of the Book Cliffs resistant ledge. As discussed above, possible allophane/imogolite in Book Cliffs may record an increase of pore-water pH during a time of clastic sediment starvation directly above the TS. From the top of Book Cliffs to the base of the Chinle interval (-4454.8 m) parasequences stack in a retrogradational pattern [each successive parasequence recording more distal (deeper-water) conditions; Fig. 39]. This interval represents a TST. No record of the MFS or HST of this depositional sequence was observed.

The F3 strata of the Chinle interval (-4454.8 to -4454.4 m) stack aggradationally and lap onto a basal unconformity (Fig. 4, inset 1) that can be traced across the Pahrump Hills outcrop for at least 40 m, correlated to north-east Hidden Valley (250 m to the north-east), and has at least 0.6 m of relief (Fig. 39). This erosion surface is interpreted as the basal SB of the Chinle Depositional Sequence (Figs 2 and 4; Appendix S10). The Chinle interval, consisting of F3, is an LST. For the succession from the top of the Chinle interval to the base of Newspaper Rock (-4454.4 to -4453.5 m), the only correlative strata in the area are poorly exposed mudstones at west

Nopah. The top of the Chinle interval is interpreted as a TS, overlain by a TST and possibly a HST dominated by proximal sublittoral lake mudstone (F1b). The MFS could not be located due to exposure limitations.

F5a strata in the Newspaper Rock interval (-4453.6 to -4453.2 m) lap onto and are aggradationally stacked atop an unconformable/erosive surface that can be correlated to west Nopah and outcrops A and C (Figs 4 and 39). It has at least 1.3 m of relief and is considered the basal SB of the Newspaper Rock Depositional Sequence. Correlative isolated sandstone strata atop the SB represent an LST. Their top surface is the TS ($ca -4453.2$ m at Pahrump Hills). At west Nopah aggradationally stacked lens-shaped resistant bedsets occur above about -4453.5 m (Fig. 39). This parasequence may represent the TST, because just above it the mudstone strata appear to extend farthest landward. In addition, there is a change in rock character at the correlative level at Pahrump Hills; the strata below -4452.8 m contain decimetre-scale concretions that are not apparent above that elevation. Together, these observations suggest that this is the level of the MFS. The resistant bedsets in the correlative interval above the MFS at south-east Nopah (-4452 to -4450 m) appear to stack progradationally, suggesting an HST.

F5a strata in the Whale Rock interval (-4452.0 to -4451.4 m; Fig. 34) lap onto and are aggradationally stacked atop an unconformable/erosive surface that can be correlated as far as west Nopah and south-east Nopah (Fig. 39). The surface has at least 1.7 m of relief and is considered the SB at the base of the Whale Rock Depositional Sequence. The top of Whale Rock and laterally equivalent sandstone strata represents a TS. Above the TS, a correlative interval at west Nopah appears to be a retrogradationally stacked parasequence, hence these strata are interpreted as the TST. Above that level ($ca -4451.2$ m) outcrops at Pahrump Hills allow little further refinement. However, observations from west Nopah and south-east Nopah (Fig. 39) suggest an onset of progradational stacking at about -4451.2 m that is also evident in the F4 to F5b succession (-4448.2 to -4445.8 m) at Pahrump Hills, where F4 strata thicken and coarsen upward in a progradational pattern that continues into the F5b strata above -4447.5 m. Thus the succession above -4451.2 m to the top of the outcrop is considered an HST.

Five depositional sequences at the Pahrump Hills section are proposed: Panamint, Crowder,

Chinle, Newspaper Rock and Whale Rock (Figs 34 and 39). They range in thickness from 1.4 to 6.0 m, within the thickness range known from underfilled lake basins on Earth. In any case, depositional sequences are defined via geometric constraints, not by thickness or inferred changes in lake level (e.g. Mitchum & Vail, 1977; Bohacs *et al.*, 2000).

Depositional history and origin of components

Integrated portrayal of the depositional history of the study area addresses provenance bedrock character, weathering, erosion and transportation, deposition and early diagenesis. Mudstones are dominated by detrital minerals (Table 2) derived from basaltic bedrock and glass (part of the amorphous fraction) sourced from basalts pulverized by meteor impacts (Arp *et al.*, 2019). Tridymite is most likely detrital and impact derived, or less likely, sourced from silicic volcanics. Maghemite is attributed to weathering of detrital magnetite, and could have formed in the catchment, along the transport path, and in the lake itself. In ChemCam analyses of sandstones, points with lowest SiO₂ contents (<40 wt. %) also show elevated FeO_T (Fig. 6A) without associated MgO enrichment (Fig. 6B), pointing to possible Fe-oxide cements.

Diagenetic phases in CheMin samples (opal-CT, phyllosilicates, sulphates and possibly carbonates) provide essential insights into environmental conditions during accumulation and early burial and are compatible with evaporation processes. They span a wide range of solubilities, from Ca-sulphate (\pm carbonate) and silica (opal-CT) through kerolite (Mg-silicate) to Fe-sulphates and Mg-sulphates, and suggest variable activities of Al, Fe and Si and neutral to low pH waters.

Variable point-to-point compositions of F1 mudstones analysed by ChemCam (Fig. 6) are consistent with diagenetic products (opal-CT, Mg-smectites, Mg-sulphates, Fe-sulphate, colloidal alumino-silicates such as allophane) that reflect open-system weathering (in catchment or at site of deposition). High solubility of Fe-sulphates and Mg-sulphates suggests formation within surficial sediments during periods of extreme evapoconcentration.

Some minerals may have both detrital and diagenetic origins, depending on their stratigraphic context (phyllosilicates, pyrite, haematite). The poorly ordered or amorphous component seen in

CheMin analyses contains both detrital (volcanic and impact glass) and diagenetic constituents (allophane, imogolite, etc.).

Provenance and weathering

Provenance. Lacking analyses of the primary basalt materials that probably dominated the source area, characteristics of primary materials were estimated via calculated normative mineralogy (CIPW Norm; Cross *et al.*, 1902). Cousin *et al.* (2017) compiled and reviewed ChemCam analyses of igneous rock fragments of potential hinterland derivation and identified two parent-rock types with more than a single analysis (for statistical rigour): Group 1 (basalt-trachybasalt) and Group 4 (gabbro norite); referred to as Gp1 and Gp4 below. Calculating normative mineral compositions for these groups faces two potential problems: (i) variable amounts of amorphous material, which could include volcanic or impact glass; and (ii) variable abundances of minerals susceptible to weathering, degraded either *in situ*, during transport, or after deposition. All published methods assessing weathering susceptibility give the sequence olivine > glass > amphibole > pyroxene > plagioclase > alkali feldspar from most to least susceptible. To overcome the issues above only more resistant minerals, clinopyroxene and plagioclase, were used to characterize potential igneous sources, allowing comparison of measured mineral compositions with putative primary sources. The extent of olivine survival, relative to a much less easily weathered mineral, plagioclase, was used as a measure of the severity of weathering in the source area. Both of these comparisons are shown in Table 4 (additional detail in Appendix S2B).

Weathering. The abundance of easily weathered primary minerals (forsterite and pyroxenes) and paucity of their weathering products (for example, clay minerals) as well as the presence of apatite and pyrite indicate minimal chemical weathering

Table 4. Mineral ratios to characterize provenance of sediments and source material's extent of weathering.

Material	Clinopyroxene/ Plagioclase	Olivine/ Plagioclase
Confidence Hills (CH)	0.53 ± 0.07	0.12 ± 0.03
Mojave (MJ)	0.25 ± 0.04	0.26 ± 0.07
Telegraph Peak (TP)	0.22 ± 0.04	0.29 ± 0.09
Cousin <i>et al.</i> Group 1	0.49 ± 0.24	0.26 ± 0.18
Cousin <i>et al.</i> Group 4	0.24 ± 0.03	0.83 ± 0.37

in the hinterland, or significant erosion followed by rapid transport and burial, or both.

Using the ratio of the most easily weathered mineral, olivine, to the resistant one, plagioclase, (Table 4), it is possible to obtain a measure of the extent of weathering. F1a (CH) and F2 (MJ) show loss of easily weathered olivine relative to their putative parent basalts, Gp1 and Gp4, respectively. The difference in relative loss of olivine is reduced but not eliminated when the differences in original olivine content of the basalt sources are considered. Thus, the source materials of F1a suffered more chemical weathering than those of F2.

These considerations imply that river waters that entered the lake had relatively low solute concentrations. Consequently, authigenic mineral formation depended on concentration processes in the lake itself or in the resulting soils/sediments. The main contributors of solutes to runoff waters would have been volcanic glass (basaltic), impact glass (modified basalt) and forsterite (Mg, Fe and silica). Groundwater, having longer contact with more deeply buried sediments and not subject to the erosion and

transport that sourced the CheMin samples, probably had higher concentrations of solutes.

Previous work hypothesized deposition of the sediments in near-neutral pH and low Eh waters and subsequent passage of acidic groundwater through them to produce the observed diagenetic products (Rampe *et al.*, 2017). Those authors further hypothesized that the acidic conditions might have been caused by oxidation of sulphide to give H_2SO_4 , although the probable low permeability of the sediments (Appendix S5B) would not have allowed such pervasive diagenetic processes.

On the basis of geochemical modelling an alternative scenario is proposed that could have produced sporadic influxes of acidic waters. It is likely that there were low-pH waters from equilibration of meteoric water with volcanic SO_2 but even more acidic waters could have occurred. Because Mars was still volcanically active at that time (Xiao *et al.*, 2012), this study considers that emissions from sporadic volcanic activity anywhere on the planet could have caused temporary major changes to the global atmosphere. Volcanic emissions can produce very low-pH rain not only from SO_2 , but because HCl is very effectively

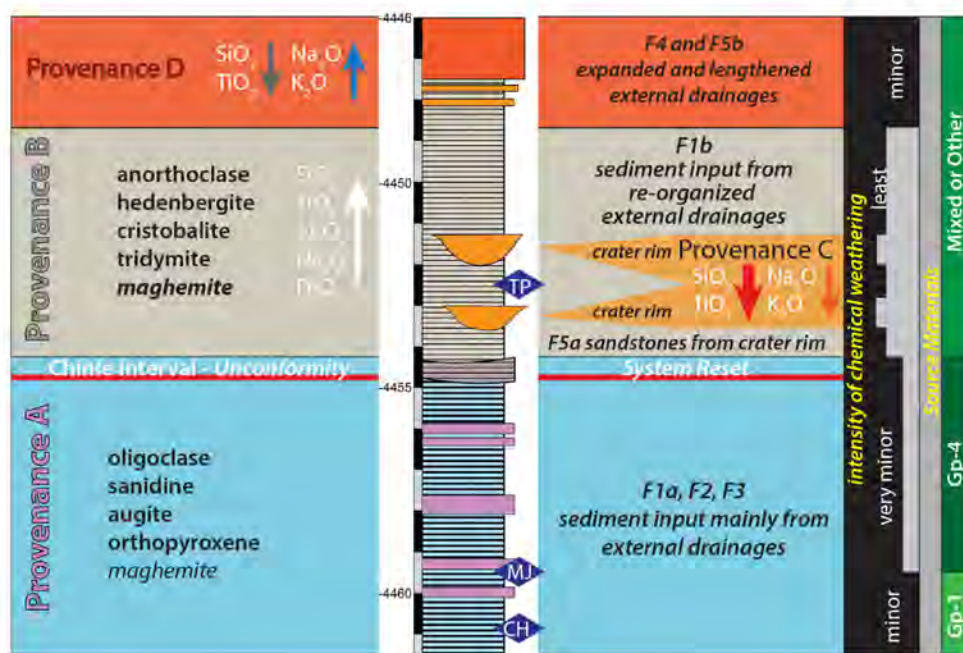


Fig. 40. Summary of character, distribution and origin of sedimentary provenances. Left of stratigraphic column. Main provenances (A) and (B) are distinguished via contrasting sets of minerals (Table 2) and contrasts in chemical composition (arrows indicate changes relative to underlying strata). Right of stratigraphic column. Presumed source of sediments and changes in external drainages over time, intensity of chemical weathering and potential source materials (in reference to Tables 2 and 4). Gp-1 = Cousin *et al.* (2017) ~ basalt – trachybasalt; Gp-4 = Cousin *et al.* (2017) ~ gabbro norite. Blue rhombs mark location of drill samples referred to in text.

scavenged by rainwater (Tabazadeh & Turco, 1993). In an extreme case, modelled results of basaltic eruptions indicate a pH of 2 to 3 (Black *et al.*, 2014). Furthermore, in such an environment, the weather would be expected to be quite variable with the possibility of major storms at various intervals affecting both weathering in the hinterland and transport of sediment.

In summary, although discussing provenance and weathering is necessarily limited by the data base, evaluating these topics in relative and statistical terms (Fig. 5; Tables 2 and 4; Appendix S2B) within the context of stratigraphic and sedimentological constraints gives the basic relations summarized in Fig. 40 and Appendix S2B: (i) provenance A for all strata below Chinle and above Chinle; (ii) provenance B for F1b mudstones; and (iii) provenances C and D for sandstones F5a and F5b.

Erosion, transport and deposition

The envisioned landscape evolution of the study area, anchored by sequence-stratigraphic considerations, is visualized by a set of palaeogeographical maps (Fig. 41). The base of the section records a significant expansion of the standing water of the lake, such that the Pahrump Hills area was fairly far out towards the centre of the lake. Prior to this expansion, conglomerates that have an uneven upper topography (deposited as fluvial gravel bar forms, analogous to the interpretation of the pebbly sandstone of the Shaler unit by Edgar *et al.*, 2018) were deposited on top of deltaic sandstones. Onlap of cross-bedded sandstones and parallel-bedded mudstones onto the conglomerate topography records rising water levels and lake expansion (Fig. 41A). These stratal relations and a likely SB at the base of the Panamint conglomerate imply that the strata below the SB (the Bradbury group; Fig. 2) are not genetically related to the strata examined for this study, although their depositional conditions might have been similar. Whereas the basal conglomerate and sandstone can be considered part of the Bradbury group in a lithostratigraphic sense, only the strata above the Panamint SB are chronostratigraphically equivalent to the Murray formation at Pahrump Hills. The Panamint SB therefore marks a significant reset of the lake system and a change in lake-basin type (*sensu* Carroll & Bohacs, 1999), as evidenced by the differing characteristics of the mudstone and sandstone strata below and above – for example, between the mudstones of

the Sheepbed and Pahrump Hills members (e.g. Hurowitz *et al.*, 2017), and the proportion of clinoform versus channel-form sandstone strata (e.g. Grotzinger *et al.*, 2015; this paper). Changes in lake system behaviour generally occur abruptly (not gradually) as the system crosses a geomorphic threshold through a combination of climate, tectonics and landscape evolution processes (Bohacs *et al.*, 2003; Carroll, 2017). For example, on Earth, the shift from intermittently open hydrography balanced-fill to persistently closed hydrography underfilled conditions between the Tipton and Wilkins Peak members of the Green River Formation was attributed to the diversion of a major inflowing river by fault movement; the subsequent change from underfilled to balanced-fill state (Laney Member) occurred because of stream capture by landscape evolution (Pietras *et al.*, 2003; Smith *et al.*, 2015). An analogous abrupt shift in system behaviour at Gale Crater in the section below the study interval was interpreted to occur between unit 2 and unit 3 of the Shaler outcrop based on distinctive changes in bedding and composition, and attributed to drainage capture (Edgar *et al.*, 2018).

In the interval from the base of the section at Pahrump Hills to the base of Chinle unconformity, the well-organized millimetre-scale to metre-scale stratal stacking and common provenance (provenance A; Fig. 40) indicates that lake behaviour was rather stable. Progradation and desiccation influenced shoreline regression sub-equally. The lake was subjected to alternating wetter/warmer and drier/colder episodes at higher and lower frequencies. The higher frequency events are recorded by the millimetre-scale layering of softer and harder layers. The frequency of wetter/warmer to drier/colder alternations may have been seasonal, yearly, decadal, centennial, millennial, or some combination thereof.

The lower frequency episodes are expressed as metre-scale parasequences capped by resistant ledges (Comb Ridge, Pink Cliffs, Book Cliffs; Fig. 41B and C). These parasequences stack in a manner that indicates an overall 'drier' trend (increased salinity, lake contraction, lower lake levels) up to Book Cliffs, overlain by an overall 'wetter' trend up to Chinle. These trends in the rock record are paralleled by trends in Mg, Br and Cl to maxima at Book Cliffs and Fe to a minimum at Book Cliffs (Appendix S4).

System behaviour changed significantly at the Chinle SB (Figs 4 and 39; Appendix S10). The Chinle SB records a substantial and

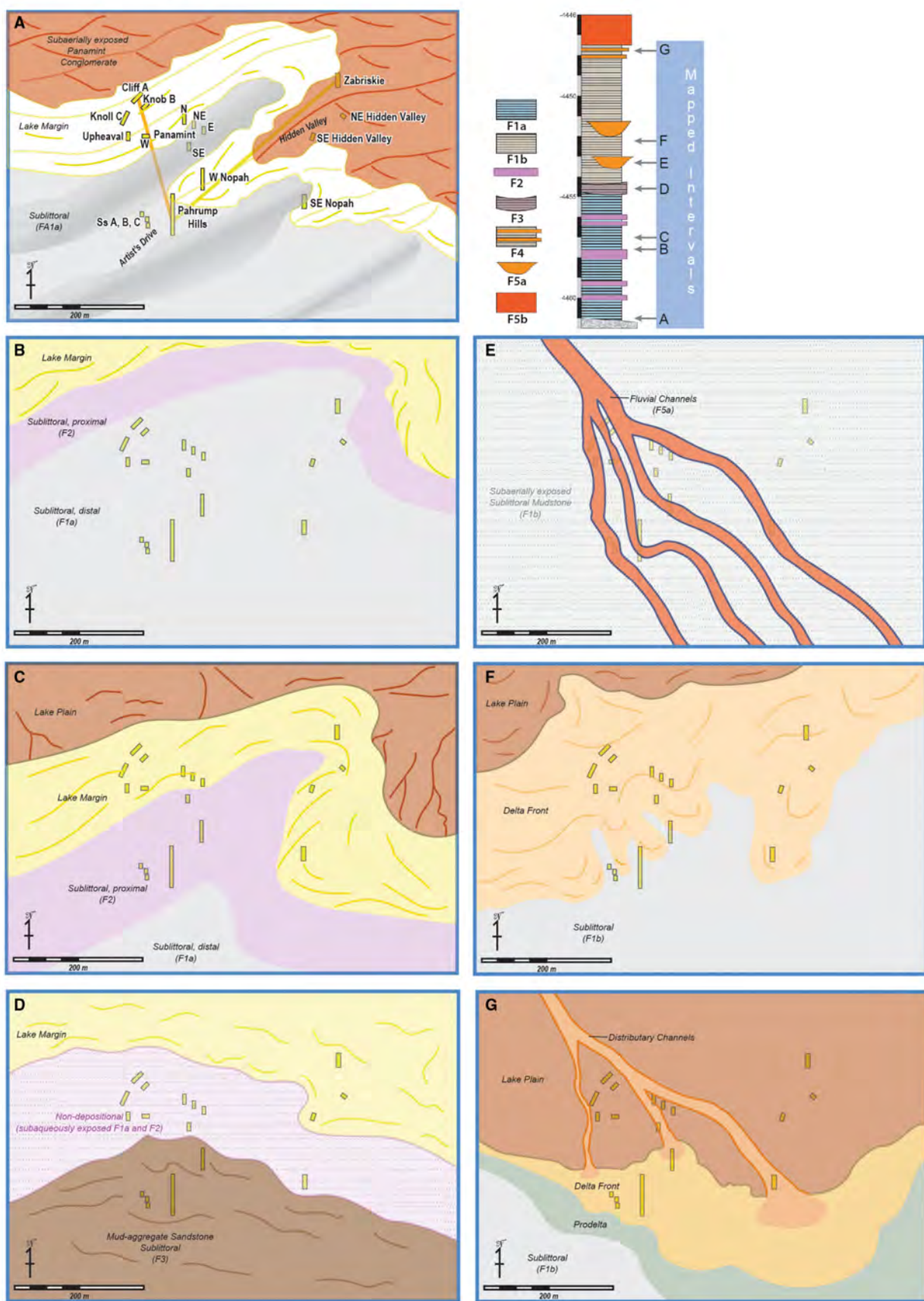


Fig. 41. Palaeographic maps illustrate the landscape evolution of the study area for the succession of rocks exposed at Pahrump Hills. (A) Map marks the base of the section and the onlap of F1a mudstones onto the pre-existing topography atop the Panamint conglomerate. (B) to (G) Successive time slices; a simplified stratigraphic column (upper right) shows the approximate stratigraphic position of the mapped time slices (numbers along left side of column are elevation in metres).

abrupt shallowing and is overlain by reworked sub-Chinle sediment (rounded crystals, mud rip ups, provenance A composition) with current-generated and wave-generated sedimentary structures (Fig. 41D). This shallowing interrupts the lake expansion ('wetter-upward') trend that started above Book Cliffs. The section above the Chinle interval, up to a metre or two above Whale Rock, records a basinward shift in depositional environments, from a relatively stable lake centre setting below Chinle, to a setting where lake plain stream channel-fills (F5a sandstone) alternate with lake margin to proximal lake centre muddy strata (Fig. 41E). Shoreline regression was dominated by desiccation rather than progradation. Instead of contracting to form a hypersaline water body, lake levels dropped intermittently so severely

that the Pahrump area became exposed and the rivers that supplied water had to cut channels (Newspaper Rock, Whale Rock, Sandstones A, B and C; Figs 4 and 41E) to carry water and sediment farther into the now much reduced lake [the depocentre was probably to the south or south-east, based on inferred bedform migration directions (Fig. 31)]. The change in provenance interpreted for both the F1b mudstones (provenance B) and F5a sandstones (provenance C; Fig. 40) of this interval suggests a possible cause for its shift in behaviour – a change in sediment supply from one dominated by a long-reach river system from outside Gale Crater (Farah Vallis; Arp *et al.*, 2019) to mainly short-reach systems from the crater rim and walls. The observed changes in augite and pigeonite relations in F1b (TP;

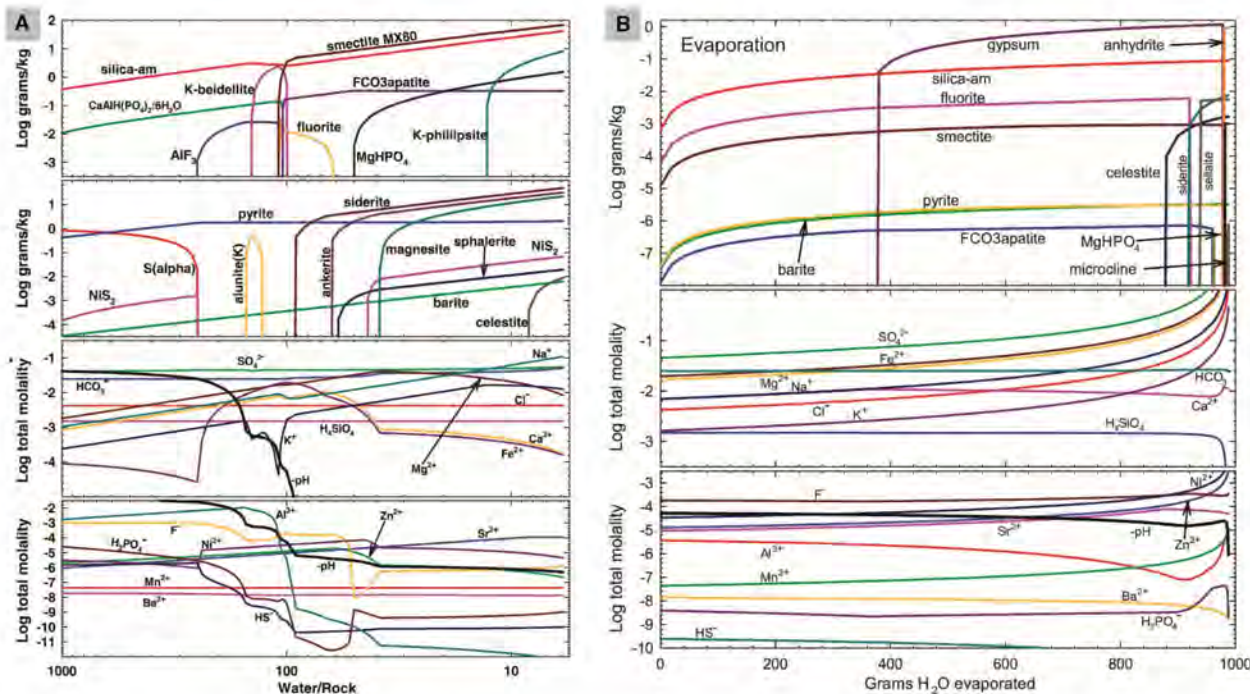


Fig. 42. Geochemical modelling results. (A) Hinterland weathering reactions of dilute volcanic gas condensate with basalt at 10°C and 0.05 MPa P(CO₂), and resulting compounds and water chemistries. See text and Appendix S15 for details of reactants. (B) Chemical compounds and water chemistries formed from evaporation of lake water derived from the w/r 100 reaction of diluted volcanic gas condensate with basalt (Fig. 42A).

Table 2) also indicate a change in provenance – they cannot be explained by transport processes because both minerals have similar density and hardness. A more local provenance for at least Whale Rock is supported by its more angular sand grain shapes, higher feldspar content and coarser grain-size distribution (Fig. 28).

The interval above Whale Rock to the top of Salsberry Peak records a lake margin to deltaic-shoreline setting with more expanded and stable lake levels in a relatively well-organized coarsening-upward succession (Fig. 41G). Shoreline movement appears to have been mostly by progradation of advected detrital sediments. Changes in sandstone composition (to provenance D, with lower feldspar content; Fig. 40), grain shape (to more rounded; Fig. 33), and grain-size distribution (skewed to finer sizes) suggests a longer-reach fluvial supply, potentially associated with Farah Vallis.

Geochemical modelling

The observed mineral assemblage and distribution, as well as physical sedimentology and stratigraphy, indicate a general Type III brine-evolution path ($Mg > Ca$) with a $Na-SO_4-Cl$ endpoint, analogous to the Saline Valley or Death Valley systems on Earth (Eugster & Hardie, 1978). The lack of carbonate minerals, however, suggests that the ‘Gale lake’ brine-evolution path differed slightly, with some acid-saline episodes (see below; cf. Benison & Goldstein, 2002).

Geochemical modelling of the origin of secondary minerals started with an acidic rain derived from a dilute volcanic gas condensate that reacts with Martian basalts at 10°C in a CO_2 -rich atmosphere. Mineral weathering products, such as smectite, pyrite and silica, travelled into the lake along with detritus and runoff of the now-evolved weathering water. Lake waters reacted further with detrital minerals, evaporated episodically, and produced gypsum with modest amounts of amorphous silica and small amounts of other evaporites (see details of geochemical modelling in Appendices S14 and S15).

The composition of the acidic-rain reactant was derived from dissolution of one mole of Erte Ale volcanic gas (Oppenheimer et al., 2014), with an added 1% O_2 (Lu et al., 2014) in 1 kg of water, then equilibrated with a CO_2 partial pressure of 0.05 MPa, as described in Schieber et al. (2017) and tabulated in Appendix S14. An

atmospheric CO_2 buffer for both weathering and diagenetic settings limits the model’s application to shallow diagenesis and avoids the need to turn off the buffer at an arbitrarily chosen reaction point. The rain’s initial pH is 1.4, owing to sulphuric acid from disproportionation of SO_2 in the volcanic gas. The rain was reacted with the parent basalt proposed above. Many model runs were executed for variations of $P(CO_2)$ between 0.01 and 0.10 MPa and three basalt compositions (Mazatzal basalt; McSween et al., 2006a, 2006b; and two compositions from Cousin et al., 2017; see Integrative method). The various runs yield small differences in secondary mineral quantities and the water/rock ratios of mineral appearance or dissolution, but the particular minerals and their precipitation sequence varies little. At 10°C, metastable smectites and amorphous silica form in place of kinetically impeded stable micas, chlorite, amphiboles, quartz and other silica polymorphs that were suppressed from the calculation.

The modelled reactions address the weathering of outcrop and regolith as well as shallow sediment diagenesis because both settings, hinterland and sediment, form a chemical continuum involving the same rock and water reactants. Hinterland basalts and weathering products become the sedimentary detritus, and the reaction water (runoff from hinterland) becomes the lake water.

One representative model calculation [Group-1 basalt; $P(CO_2)$ buffered at 0.05 MPa (Phillips et al., 2001; Kurokawa et al., 2018)] shows the neutralization of the sulphuric acid-dominated rainfall (Fig. 42A). As pH rises from 1.4 to 6, amorphous silica precipitates at low pH, followed by smectites at pH 3, then siderite, ankerite and magnesite at pHs exceeding 5. Pyrite precipitates at low pH, and small amounts of minor-element sulphates, phosphates, fluorides and sulphides precipitate as shown in Fig. 42A. Among the minor elements are Ni and Zn, aqueous concentrations of which are limited by sulphides at a low water/rock ratio (w/r), where pH is elevated.

Aqueous Fe, Ca and Mg concentrations rise to separate maxima before they are largely sequestered in carbonate minerals. Aqueous Al^{3+} builds to a maximum at low pH before it is removed to smectites. In a natural setting, aqueous Al^{3+} may combine with silica to form allophane as a metastable amorphous precursor to smectites. Neither Ca-sulphates nor Fe-oxides form, owing to atmospheric CO_2 , and an absence

of atmospheric oxygen, which facilitates the reducing conditions imposed by the large ferrous iron input from basalt.

Weathering and early diagenesis

These calculations have significant implications for understanding weathering and diagenesis. Most of the minimal clay-mineral component is likely authigenic (kerolite; *Compositional Data and Inferences*; Table 2). Kerolite, though detected, could not be included in the calculation because it is not in the BRGM data base. As a proxy, smectite with significant Mg content was used (MX80 in the BRGM data base). Computed smectites (beidellite and smectite MX80; Fig. 42A) and amorphous silica are dominant weathering products at pH >3.2. The computed precipitation of moderate amounts of smectites in weathering under acidic conditions (excluding carbonates) coincides with findings in the Pahrump sediments and with spectral data on weathered basalts in Martian hinterlands (Ehlmann & Edwards, 2014). The model suggests that clays in the absence of carbonate minerals imply a w/r of weathering in excess of 100. In combination with the large proportion of glass, olivene, pyroxene and plagioclase in the basaltic source material, such high w/r suggest short contact times between surface waters (rain) and the waters and the rocks of the hinterland and sediment. In contrast, in the case of small w/r the proportion of clay and carbonate would be larger, relative to primary basalt material.

In contrast to the Sheepbed mudstone analysed earlier in the mission (Schieber *et al.*, 2017), clay minerals are a minor component of the Pahrump Hills mudstones (Table 2), implying either minimal chemical weathering or possibly that smectites bypassed Pahrump Hills to a more distal depositional site. The computed amorphous silica is a likely component of the amorphous material identified in Table 2. Some silica may have recrystallized to opal-CT, whereas the other silica polymorphs (cristobalite and tridymite; Table 2), are plausibly the products of meteorite impact (very small crystallite size of *ca* 50 nm; *Compositional data and inferences*) or hydrothermal alteration in an impact setting.

The strata contain small amounts of pyrite (Table 2), plus substantial jarosite, likely due to secondary alteration. The pyrite is plausibly detrital, derived from hinterland basalt weathering, consistent (as on Earth) with a largely

oxygen-free early atmosphere (Cloud, 1968), although some of it could have formed during early sediment diagenesis. The hinterland weathering model (Fig. 42A) and variations thereof (17 model runs) does not yield haematite or jarosite, suggesting that both formed by later alteration of the sediment itself, which likely also contained detrital magnetite that altered to maghemite (Table 2). This presumed secondary alteration of the sediment (either post burial or during outcrop weathering) is backed by K-Ar dating (Martin *et al.*, 2017) that suggests the jarosite to be significantly younger than the primary sediment.

Aqueous Ni and Zn reach maxima in the w/r (water/rock ratio) range of 200 to 60 where they are not limited by sulphides, making them available in runoff to the lake, although Ni could be taken up by smectite at the weathering site, as it is on Earth. Equally, both Ni and Zn could be concentrated in other authigenic phases.

In appraisals of the overall process producing the Pahrump sediments, the role of sulphuric acid rain has been recognized in prior studies (Hurowitz & McLennan, 2007), but previous researchers have not put forward a specific portrayal of the chemical reactions involved. Calculations conducted for this study provide specific examination of underlying reactions, thereby constraining likely pHs, oxidation states, the role of sulphate vis-à-vis carbonate, and what mineral assemblages are reasonable. Two such weathering assemblages are those containing carbonates, at pH >5 and those lacking carbonate at lower pHs. Although carbonate quantity is generally modest on Mars, there are many local occurrences, particularly of magnesite (Scheller *et al.*, 2021), which this study's modelling produces, indicating that pH can be expected to exceed 5 in some settings, though apparently not at Pahrump. Being able to compute conditions for magnesite occurrence exemplifies the value of geochemical modelling for building a broader concept of early Martian geochemical conditions.

The near absence of carbonate minerals in the sediment indicates that none were produced during weathering in the hinterland outcrop. Had they formed there, such carbonates could have been transported the comparatively short distance to the crater floor (Zuffa, 1980; Schieber & Shao, 2021). This absence, despite the abundance of atmospheric CO₂, indicates that the pH of weathering fluids remained too acidic to form

the siderite, ankerite and magnesite computed for weathering of basalt in the source terrain, i.e. the weathering reaction (Fig. 42A) did not progress to w/r less than *ca* 100, where pH climbs above 5 and permits carbonate precipitation. This carbonate constraint, combined with the abundance of primary volcanic rock detritus indicates minimal reaction of source basalt with weathering waters or with pore fluids in the lake sediments.

In-lake processes

Although carbonate did not form in the hinterland outcrop, a small amount may have formed locally during sediment diagenesis (Fig. 42A) in locations where pH rises above 5 at w/r < 100. The high w/r (100) of weathering, and the minimal diagenetic modification suggest that reasonable lake waters for further examination of evaporation are those derived from the weathering model at w/r 100.

The observed casts of pseudomorphed evaporite minerals (see *Compositional data and inferences*; Figs 13 to 15) suggest that lake waters repeatedly evaporated at the close of many of the millimetre-scale depositional cycles seen in F1 (Fig. 22). The lake water must be largely derived from runoff and groundwater like that computed in the weathering model (Fig. 42A). Acidic enough to preclude precipitation of most carbonate minerals, the w/r 100 water from the weathering-diagenesis reaction in Fig. 42A (tabulated in Appendix S13) is a plausible candidate for lake water composition, dominated by sulphate, bicarbonate, Mg and Fe with modest Na, Ca and Cl at an initial pH of 4.3. Bicarbonate is generally greater than or equal to the concentration of Mg plus Ca, characteristic of the Type III brine evolution pathway of Eugster & Hardie (1978).

Computed evaporation of the w/r 100 water at 10°C (Fig. 42B) produces dominantly amorphous silica and gypsum. At high degrees of evaporation, anhydrite rather than gypsum, as well as small amounts of sulphates, fluorides and carbonate (siderite) form. At evaporation to near dryness, aqueous Mg and sulphate concentrations are large enough to saturate with Mg-sulphate salts (for example, epsomite), although these conditions are not addressed in the computation itself (see Appendix S15).

Authigenic gypsum was proposed by Kah *et al.* (2018) as the likely composition of crystal casts observed in Pahrump Hills mudstones, although alternative minerals, such as shortite

(see section on *Physical attributes*) and trona (see *Compositional data and inferences*) are equally possible. The modelled lake water is saturated with amorphous silica at the outset of evaporation, thus additional amorphous silica precipitates throughout evaporation (Fig. 42B), and prior to gypsum saturation. This particular modelling result prompted re-evaluation of CheMin data and strongly recommended amorphous silica as an important cementing agent during evaporative interludes (associated with gypsum). Evaporitic silica is a likely cementing agent in F1 and F2 (Table 3), making the layers with abundant evaporite mineral pseudomorphs (Figs 12 and 14) more resistant to aeolian erosion.

Among the many evaporation runs not shown here are those that start with a w/r 10 lake water composition, which would be at a point in the weathering run (Fig. 42A) where siderite, ankerite and magnesite constitute 45 wt. % of the generated mineral mass and pH is 6.1. Evaporation of that water (Fig. S14-1 in Appendix S14), and of waters from other weathering runs extracted at w/r 10, shows a strong dominance of carbonate minerals, especially magnesite with lesser siderite and ankerite, that is not observed in the Pahrump Hills mudstones. Waters at such w/r ratios might have evolved in long-residence groundwater and issued from springs fed by such groundwater, possibly enabling localized carbonate deposition.

Although this modelling represents the overall geochemical and mineral evolution, in some parts the kinetics of the reactions play a much more significant role. The sequence of ease-of-weathering is olivine > glass > the other components of a basalt. Thus, if the modelled reactions do not go to completion, the products of the first-reacted components will dominate. In the case of basaltic glass and probably impact glass too, reaction products should be similar to those of the bulk basalt. Modelling results show preferential loss of forsterite olivine relative to the more resistant mineral components of basalt. The weathering reaction of forsterite can be represented crudely as $Mg_2SiO_4 + 2H_2O \rightarrow 2Mg^{2+} + 4OH^- + SiO_2$ (aqueous). Clearly, this is not a representation of the whole process, but reactions like this give, for example, groundwaters with pH values <8 and up to >12 for weathering of the Oman ophiolite (Giampouras *et al.*, 2020). Although reduced in abundance relative to the other components, some olivine survived

transport to the site of deposition (Table 2). If preferential weathering occurs after deposition it could produce alkaline waters locally, either in time or space, capable of precipitating carbonate minerals not predicted by the bulk reaction scheme.

The lack of preservation of original carbonate minerals may be a consequence of neutral to low pH and low concentrations of HCO_3 of the lake waters at the time of accumulation or sporadic acid rain. Model calculations shown above (and in Appendix S15) plausibly suggest that under common assumptions of the past Martian atmosphere, low HCO_3 concentrations in overland flow and lake waters should have been such as to make lower pH values a common occurrence. Groundwaters, on the other hand, reacting with bedrocks and regolith for much longer, should be characterized by higher pH values, carry a higher solute load, and be conducive to carbonate precipitation. Given that the preserved record of lacustrine deposits at Pahrump Hills implies that groundwater input was an essential component of the system (Fig. 37), it is predicted that carbonates might be found in areas where groundwaters discharged in the lower lake plain, littoral or very proximal sublittoral zones.

Dendrites and Ni-anomaly

The depositional history and processes proposed above can also explain the presence and character of the dendrites observed in F1a strata. The dendrites at *ca* –4461 m show local, anomalously high amounts of the major elements Mg, Ca and S, and minor element Ni in both the ChemCam and APXS analyses. Comparison of the APXS composition of the feature and nearby non-diagenetic rock allowed derivation of an end-member composition for the dendrites (VanBommel *et al.*, 2016). Mg, S and Ni are most abundant elements in the dendrites while Ca also is prominent but with lower statistical certainty.

The sum of molar fractions of Mg (32.3%) and Ca (12.4%) is 44.7% compared with 45.3% for S. The results are compatible with both Mg-sulphate and Ca-sulphate phases. Nickel occurs at an extraordinary level of 5.3 mole%. Both Ni and Zn can readily substitute for Mg in orthorhombic $\text{MgSO}_4 \cdot 7\text{H}_2\text{O}$ (Balarew *et al.*, 1973). There is also an anomalously high amount of Zn but an order of magnitude lower (molar percent) than Ni. These observations imply the presence of a Mg-

sulphate mineral phase. No Mg-sulphates were detected in any of the CheMin analyses (Table 2), suggesting that any Mg-sulphate occurs as an XRD-amorphous phase (due to subsequent partial dehydration; Vaniman *et al.*, 2004).

Two further aspects of the system must be considered, the Mg and Ni concentration process and their transport. The source basalt is a realistic source of the Ni because basaltic laterites can concentrate the element (Aribowo *et al.*, 2018; Campodonico *et al.*, 2019). Thus, preferentially weathering olivine (and glass) in the source basalt would provide a source of Mg and Ni; furthermore, it would increase the pH noticeably (see Appendix S15), ensuring that Ni is immobilized and concentrated as oxyhydroxides (Huang & Rondinelli, 2019). After this concentration process, the next acid-rain storm would mobilize and transport the elements found in the dendrites subsequently formed by evaporation of that input. Further support for this hypothesis is the considerable Cl content of the dendrites (1.6 ± 0.4 wt. %) compared with its host rock, (0.52 ± 0.04 wt. %; VanBommel *et al.*, 2016). This would be expected if volcanically-induced acid rain were the dissolution and transport solvent. Additionally, because the dendrites were probably less permeable and porous than the host rock, the Cl is likely to be an original component. The anomalous ‘one-off’ nature of the dendrites was highlighted by the integrated interpretation that established a robust picture of the normal behaviour of this system (Figs 35 and 36) whose evaporation trends are opposite to those needed to form dendrites.

Lake-basin type interpretation and implications (earth analogues)

This section places the fluvial-floodplain and lacustrine environments envisioned for the Pahrump Hills strata into the context of lake basin systems on Earth. Key aspects of lake systems are sediment and water delivery pathways (precipitation, overland and groundwater), components of potential accommodation (*sensu* Carroll & Bohacs, 1999) and conditions in the lake water column (lake level changes, mixis and stratification).

Pahrump Hills and associated strata represent an evaporative lake facies (Carroll & Bohacs, 1999; Schieber *et al.*, 2015; Kah *et al.*, 2018) with most evaporite minerals formed very early (<<1 m burial). It is

interpreted as accumulated in an underfilled-through-flow lake basin, that is, a lake system with saline to hypersaline surface waters, a closed surface hydrography and through-flow groundwater input in a smaller sub-basin within Gale Crater in an intermediate position along the topographic profile from the crater wall to the ultimate low spot of the basin. Such a setting explains the occurrence of intra-stratal evaporites and the absence of bedded evaporites in the Pahrump Hills area (e.g. Rosen, 1994; Benavente *et al.*, 2017). It also indicates that a single standing body of water did not occupy the entire volume of Gale Crater at this time. Indeed, if Gale Crater had ever been filled with water from rim to rim, the resulting lake would be about the area of lakes Ontario or Balkhash, 1.3 times the volume of the largest volume lake on Earth, the Caspian Sea, and more than 3 times the depth of the deepest lake on Earth, Baikal (and 4.4 times its volume). It suggests that there were at least two separate lakes (i.e. standing bodies of water) during the accumulation of the Pahrump Hills section: one in the study area and another downstream, at a lower elevation, probably to the south of the present study area. This is analogous to the sub-basins of the present-day Salt Lake Valley of Utah where the evaporite-free Utah Lake feeds into the hypersaline Great Salt Lake, 50 km downstream and 88 m lower (Bohacs *et al.*, 2000, 2003). The floor of Gale Crater could easily accommodate the Utah Lake–Great Salt Lake system, or several lakes of the size of present-day lakes Eyre, Rudolph, Issyk-Kul, Torrens or Albert (Carroll & Bohacs, 1999; Bohacs *et al.*, 2003).

Although bedded evaporites are considered emblematic for evaporitic sedimentary successions, not seeing them at Pahrump Hills does not disqualify the succession as evaporitic (*cf.* Rosen, 1994; Benavente *et al.*, 2017). The absence of widespread dissolution features (stratal disruption, convolute bedding, intrastratal breccias and the preservation of millimetre-scale layering and Ca-sulphate minerals in cross-cutting veins (Minitti *et al.*, 2019), collectively suggest that lake basin processes at the time of accumulation can plausibly explain the absence of bedded evaporites at Pahrump Hills. Accumulation of lacustrine bedded evaporites requires persistent groundwater discharge to maintain brine pools (an underfilled-discharge lake basin; Benavente *et al.*, 2017), something that apparently did not happen at the Pahrump Hills location. Sequence stratigraphic analysis

(see *Parasequence set to depositional-sequence set scale*) predicts that bedded evaporites should occur in the overall lowest area of the crater floor (Fig. 37) where solute-rich groundwaters discharged persistently, probably in a separate sub-basin some distance south of Pahrump Hills. Such evaporites are likely buried beneath younger strata – although they might crop out on the far side of Mt. Sharp.

Although the Pahrump system could be classified as a ‘perennial’ saline lake, lake level probably fluctuated widely and the lake in the study-area sub-basin could have completely dried out intermittently. Absence of desiccation cracks is explained by the low clay-mineral content (<4 wt. %) and consequent mechanical properties of the sediment (*First order interpretation of F1*; Figs 18 and 19). Substantial freshening of the pore waters was unlikely, as evidenced by the well-preserved parallel to sub-parallel bedding at the millimetre-scale to centimetre-scale in the mudstone facies and lack of disrupted bedding and convolute laminae due to dissolution and reprecipitation. Abundant evidence of physical reworking and shallow water depths near parasequence tops in the interval below Chinle indicate that the lake waters were thoroughly mixed during those particular times.

Previous publications proposed that the Pahrump Hills succession was deposited by river-fed plunging plumes in a perennial freshwater lake, and that the Newspaper and Whale Rock sandstone lenses (both F5a in this study, Figs 4 and 30) represent the infills of subaqueous channels incised by hyperpycnal flows (e.g. Grotzinger *et al.*, 2015; Stack *et al.*, 2019). Comparing such interpretations to the detailed observations reported in this paper, as well as to what is known about hyperpycnites on Earth and personal experience with hyperpycnic deposits, indicates that a hyperpycnic interpretation is incompatible with the sedimentary record at Pahrump Hills (see detailed discussion in *Appendix S16*).

At the largest stratigraphic scale examined, the authors posit that the change in stratal character and lake system behaviour across the Panamint sequence boundary records a shift in lake basin type in the study area sub-basin from balanced-fill below (i.e. Sheepbed and main Bradbury group) to underfilled above. The interval of the Bradbury group from Sheepbed to the Panamint SB appears to be strata of the fluctuating-profundal lake facies association, with interbedded fluvial bedforms, deltaic clinotherms and

sublittoral mudstone strata with possible evidence of intermittent subaerial exposure (Grotzinger *et al.*, 2015; Hurowitz *et al.*, 2017). The dominance of fluvial and shoreline strata in that interval indicates that the standing waters of the lake seldom covered the study area, much less the entire Gale Crater. Those strata record frequently recurring relatively strong and persistent flows of similar magnitude and represent relatively high rates of sediment and water supply relative to potential accommodation (Carroll & Bohacs, 1999; Bohacs *et al.*, 2000). Thus the interval below the Panamint SB records balanced-fill lake basin conditions – which also requires at least one more lake sub-basin downstream. The interval above the Panamint SB up to at least Salsberry Peak (Fig. 34) contains strata of the evaporative lake facies association (under-filled lake basin), with interbedded profundal to sublittoral detrital mudstone and evaporative minerals, lake plain fluvial channel sandstones, and extensive early authigenesis. The dominance of profundal and sublittoral strata indicates that the lake waters had expanded in area and covered the study area frequently and persistently (Fig. 41). These strata record widely varying lake levels and intermittently recurring inflows of variable magnitude and duration; they represent overall lower rates of sediment and water supply relative to potential accommodation (or at least a decrease in the sediment : water ratio). That the area of the lake at Pahrump Hills should have expanded under such conditions seems counter-intuitive, but it accords with abundant observations of lake systems on Earth. Lake area on Earth is observed to be weakly inversely correlated with every measure of climatic humidity (Carroll & Bohacs, 1999; Bohacs *et al.*, 2003). This is apparently because more humid climates, although they can deliver more water to a lake, also deliver more sediment which tends to fill in the lake and decrease its size. Thus, the evolution of fluvial-lacustrine systems recorded in the Sheepbed to Salsberry Peak interval at Gale Crater appears to follow a trajectory well-established from the study of lake systems on Earth.

CONCLUSIONS

Notwithstanding the inevitable limitations of rover geology, the mudstone dominated succession at Pahrump Hills was amenable to Earth-like sedimentological analysis because of its (in

relative terms) exceptionally detailed data coverage. The Pahrump Hills data set may well be the most 'in depth' comprehensive data set from the entire Curiosity mission, and every effort was made to rise to the occasion and to do justice to these rocks.

The joint analysis of all rover observations leads to a number of conclusions that can be grouped into three categories: (i) conclusions concerning prevailing conditions during the accumulation of the Pahrump Hills strata; (ii) conclusions that have stratigraphic implications and illuminate how these conditions changed through time; and (iii) insights and questions that concern the Gale Crater sedimentary system at large, and its interaction with planet-scale processes and conditions.

Sedimentology and depositional conditions

1 Five facies were recognized, three of them mudstone dominated, with distinct ranges of grain size, bedding and composition.

2 Mudstones with minimal clay mineral content dominate the section (*ca* 85%) and are largely detrital from a mafic igneous provenance that experienced only minor chemical weathering.

3 The mudstone matrix consists mostly of poorly sorted silt that is cemented and infused with varying amounts of authigenic components (Fe-oxides, opal-CT, kerolite, Fe, Ca and Mg sulphates, and possibly pyrite and hydrated Na-Ca carbonates) that formed soon after deposition.

4 Sand-size particles within mudstones are authigenic, representing pseudomorphs of various evaporite minerals that initially formed on and within lake floor sediments.

5 The lake waters were saline to hypersaline. As lake levels and salinities fluctuated, they imprinted the accumulating muds with episodic growth of authigenic minerals that gave rise to millimetre-scale (evaporite-rich laminae), centimetre-scale (concretions) and metre-scale bedding (top-cemented parasequences). Overall, the Pahrump succession was deposited in an underfilled lake basin that received water from a combination of overland and groundwater flow.

Stratigraphy and depositional history

1 The Pahrump succession consists of five depositional sequences and contains all of the sequence stratigraphic elements known from terrestrial strata. While challenging when done

with rover observations, this current analysis shows that Mars, as Earth, obeys the laws of physics and chemistry. Sequence stratigraphy is validated as a robust and universal ‘set of rules’ for the study of sedimentary rocks.

2 Two of the recognized sequence boundaries (base of Panamint conglomerate, base of Chinle; Fig. 39) are unconformities that record substantial as well as critical shifts in the behaviour of the lacustrine system. Together with the sequence boundary atop Book Cliffs, they serve to subdivide the stratigraphic section into three main intervals of genetically related strata (Fig. 39).

3 The sequence stratigraphic analysis presented here also highlights the stratigraphic relation between the Bradbury group and Murray formation. Specifically, the Bradbury group strata below the base of the Panamint conglomerate do NOT have chronostratigraphic equivalents in the Pahrump Hills section.

Broader implications

1 A substantial part of variability in rock composition can be attributed to changes in provenance (Fig. 40), which integrates changing drainage basin configurations in the hinterland, type of exposed bedrock and changes in weathering regime. This observation serves as a validation for one of the key factors that made Gale Crater the finalist in landing site selection – namely that lake basins allow sampling of an entire source-to-sink system without having to visit all parts of it.

2 In places, systematic differences between elemental analyses by ChemCam and the Alpha Particle X-Ray Spectrometer (APXS) demonstrate that it is essential to identify exactly which facies was targeted, because facies relates to outcrop character (for example, smooth and flat versus steep and rugged) and outcrop character determines which instruments have ‘access’, and which ones do not. Recognizing this constraint on instrument access helps to avoid bias during interpretation of vertical and lateral trends.

3 The scour and drape bedding observed in F3 (Chinle interval) clearly resembles storm-wave reworked strata on Earth. As such it may represent the first physical evidence for wave action in ancient Martian lakes. So far, however, no analogue to terrestrial fair-weather wave ripples has been observed, possibly due to density stratification that suppressed wave-mixing to the lake

floor. Alternatively, there may be some fundamental difference between Mars and Earth with regard to the way in which surface waves leave an imprint in accumulating strata. Something potentially similar has already been found with regard to bedform generation in modern aeolian strata (mid-size ripples at Bagnold Dunes; Lapotre *et al.*, 2016).

4 By comparison to mudstone studies on Earth, sand-sized fine-grained aggregates or mud-dominated composite particles (MCPs) observed in sandy intervals at Pahrump Hills, may quite plausibly also occur in mudstone facies, particularly in association with scours and truncation surfaces. This phenomenon is most likely not limited to Pahrump Hills and may be a common element in Martian mudstones.

5 Whereas on Earth silt-rich layers typically occur intermingled with more clay-mineral-enriched mudstones, thick sections of poorly sorted silt are very uncommon. Weathering basaltic bedrock is not known to be a plentiful source of silt (Colman, 1982), and thus one wonders where all the silt came from at Pahrump. Is possibly the pulverization of the upper crust by meteor impacts, in the absence of crustal recycling, the reason for this apparent difference between Mars and Earth?

6 Saline lake waters inferred for the Pahrump Hills member were potentially a hospitable habitat for microorganisms – indeed life developed in saline waters on Earth and did not expand into freshwater environments for more than 2 billion years (Miller & Labandeira, 2002; Strother *et al.*, 2011)

7 This study shows that thoughtful integration of physical sedimentology and stratigraphy with chemical analyses and modelling significantly enhances understanding of palaeoenvironmental nuances. For example, this approach revealed key anomalies (dendrites) that suggest episodic rapid climate change events due to sporadic volcanic eruptions. For the understanding of complex systems with incomplete data sets, carefully considered integration of all data is superior to a summation of more limited evaluations of individual data sets. In other words, true integration transcends any conceivable summation of partial derivatives. The current analysis benefitted greatly from including diverse disciplines, approaches, expertise, experience and perspectives within an integrated sequence stratigraphic framework.

EPILOGUE

The data that a remote-controlled rover collects are the outcome of the many trade-offs among instrument teams, interest groups, time allotment, energy and terrain constraints, etc. Nobody ever gets exactly what they want, not even at a place like Pahrump that has (in relative terms) exceptionally detailed data coverage. Yet, of all the places along the rover traverse where Earth-like sedimentological analysis has a chance to succeed, Pahrump may well be the one with the greatest promise. The data set has sufficient depth to certainly pose a lot of good questions, and the authors of this study tried to address them to the best of their wide-ranging expertise and experience. Operating on the premise that the laws of physics and chemistry are impervious to distance, the philosophy was ‘same processes – different boundary conditions’. Judicious integration of physical sedimentology and stratigraphy with chemical analyses and modelling gave a much better understanding of palaeoenvironmental subtlety than previously possible, to the point that even seemingly anomalous features (for example, Ni-dendrites) made perfect sense. This approach enabled the authors to probe deeply and in detail into ancient Mars from an examination of just a small fraction of the total of the Murray formation (maybe 4 to 5%), and it stands to reason that if comparable scrutiny were to be applied to the rest of the Murray formation data, much more treasure could be recovered. Given the reality of incomplete data sets, understanding complex systems succeeds on the strength of careful integration of all data, rather than through aggregation of limited-reach interpretations centred on specific data sets.

ACKNOWLEDGEMENTS

This work results from MSL science activities performed at the Jet Propulsion Laboratory, California Institute of Technology, under contract with the National Aeronautics and Space Administration. The authors are grateful to the entire MSL Science team and the MSL engineering and operations teams, for generating these exceptional data. The Malin Space Sciences operations team is thanked for the high-quality images that form the basis of this project. The *Sedimentology* editors deserve our everlasting gratitude for agreeing to publish a manuscript of this extraordinary length, and through generous

use of online supplements allowed us to retain all the strands of reasoning in one place, rather than spreading them over multiple publications. And, finally, we might not have been able to ‘pull this off’ without our enforced idleness during the Covid-19 pandemic. The weekly teleconferences that stretched from early 2020 to the summer of 2021 were only possible because none of us travelled and thus finally we had the time to think deeply about these rocks without distractions. Our sincere thanks also go to the reviewers and editors, Drs Jeff Pietras, Nick Tosca, Peir Pufahl, Kevin Taylor and one anonymous reviewer, who provided us with abundant and helpful suggestions on how to streamline the manuscript for smaller size (it is now significantly less humongous than it used to be) and much improved readability. We also appreciate Elaine Richardson from the editorial office for guiding this rather complex project across the final hurdles to publication.

DATA AVAILABILITY STATEMENT

Data utilized for preparation of this paper are archived in the Planetary Data System (pds.nasa.gov).

REFERENCES

- Abreu, V., Neal, J.E., Bohacs, K.M. and Kalbas, J.L.** (2010) Sequence stratigraphy of siliciclastic systems – the ExxonMobil methodology. In: *Concepts in Sedimentology and Paleontology*, Vol. 9, p. 226. SEPM (Society for Sedimentary Geology), Tulsa.
- Ainsworth, R.B., Hasiotis, S.T., Amos, K.J., Krapf, C.B., Payenberg, T.H., Sandstrom, M.L., Vakarelov, B.K. and Lang, S.C.** (2012) Tidal signatures in an intracratonic playa lake. *Geology*, **40**, 607–610.
- Allen, J.R.L.** (1982) *Developments in Sedimentology: Sedimentary Structures, their Character and Physical Basis*, Vol., Vol. 2, p. 663. Elsevier, Amsterdam.
- Alam, M.M., Crook, K.A. and Taylor, G.** (1985) Fluvial herring-bone cross-stratification in a modern tributary mouth bar, Coonamble, New South Wales, Australia. *Sedimentology*, **32**, 235–244.
- Anderson, R.B. and Bell, J.F., III** (2010) Geologic mapping and characterization of Gale crater and implications for its potential as a Mars science laboratory landing site. *Mars*, **5**, 76–128.
- Aribowo, Y., Syahputra, Y. and Widiarso, D.A.** (2018) Characteristics of lateritic nickel mineralization in mid part of Madang and Serakaman areas, Sebuku Island South Kalimantan. *MATEC Web of Conferences*, **159**, 01038.
- Arp, G., Schultz, S., Karius, V. and Head, J.W., III** (2019) Ries impact crater sedimentary conglomerates:

- sedimentary particle 'impact pre-processing', transport distances and provenance, and implications for Gale crater conglomerates, Mars. *Icarus*, **321**, 531–549.
- Balarew, C., Karaivanova, V. and Aslanian, S.** (1973) Isomorphiebeziehungen bei den Heptahydratsulfaten von einigen zweiwertigen Metallen (Mg^{2+} , Zn^{2+} , Ni^{2+} , Fe^{2+} , Co^{2+}). *Krist Tech*, **8**, 115–125.
- Benavente, C.A., Mancuso, A., Bohacs, K.M. and Carroll, A.R.** (2017) Lake-basin-types 2.0—expanding the model to the 4th dimension... and beyond! Geological Society of America *Abstracts with Programs*. Vol. **49**, No. 6.
- Benison, K. and Goldstein, R.H.** (2002) Recognizing acid lakes and groundwaters in the rock record. *Sediment. Geol.*, **151**, 177–185.
- Bhattacharya, J.** (2010) Deltas. In: *Facies Models 4* (Eds James, N.P. and Dalrymple, R.W.), *Geological Association of Canada, GEOText*, **6**, 233–264.
- Black, B.A., Lamarque, J.-F., Shields, C.A., Elkins-Tanton, L.T. and Kiehl, J.T.** (2014) Acid rain and ozone depletion from pulsed Siberian traps magmatism. *Geology*, **42**, 67–70.
- Blake, D.F., Morris, R.V., Kocurek, G., Morrison, S.M., Downs, R.T., Bish, D., Ming, D.W., Edgett, K.S., Rubin, D., Goetz, W., Madsen, M.B., Sullivan, R., Gellert, R., Campbell, I., Treiman, A.H., McLennan, S.M., Yen, A.S., Grotzinger, J., Vaniman, D.T., Chipera, S.J., Achilles, C.N., Rampe, E.B., Sumner, D., Meslin, P.-Y., Maurice, S., Forni, O., Gasnault, O., Fisk, M., Schmidt, M., Mahaffy, P., Leshin, L.A., Glavin, D., Steele, A., Freissinet, C., Navarro-González, R., Yingst, R.A., Kah, L.C., Bridges, N., Lewis, K.W., Bristow, T.F., Farmer, J.D., Crisp, J.A., Stolper, E.M., Marais, D.J.D., Sarrazin, P. and MSL Science Team** (2013) Curiosity at Gale crater, Mars: characterization and analysis of the Rocknest sand shadow. *Science*, **341**, 1239505.
- Bohacs, K.M.** (1981) Flume studies on the kinematics and dynamics of large-scale bedforms. Sc.D. dissertation, Massachusetts Institute of Technology, 178 pp.
- Bohacs, K.M.** (1998) Contrasting expressions of depositional sequences in mudrocks from marine to non-marine environs. In: *Shales and Mudstones (Vol. 1): Basin Studies, Sedimentology and Paleontology* (Eds Schieber, J., Zimmerle, W. and Sethi, P.), pp. 32–77. Schweizerbart'sche Verlagsbuchhandlung, Stuttgart.
- Bohacs, K.M., Carroll, A.R. and Neal, J.E.** (2003) Lessons from large lake systems – thresholds, nonlinearity, and strange attractors. In: *Extreme Depositional Environments: Mega and Members in Geologic Time* (Eds Chan, M.A. and Archer, A.W.), *Geol. Soc. Am. Spec. Paper*, **370**, 75–90.
- Bohacs, K.M., Carroll, A.R., Neal, J.E. and Mankiewicz, P.J.** (2000) Lake-basin type, source potential, and hydrocarbon character: an integrated sequence-stratigraphic–geochemical framework. In: *Lake Basins Through Space and Time* (Eds Gierlowski-Kordesch, E.H. and Kelts, K.R.), *AAPG Stud. Geol.*, **46**, 3–33.
- Bohacs, K.M., Grabowski, G.J., Jr., Carroll, A.R., Miskell-Gerhardt, K.J. and Glaser, K.** (2007) Lithofacies architecture and sequence stratigraphy of the Green River formation, greater Green River Basin, Wyoming and Colorado. *Mt. Geol.*, **44**, 39–60.
- Bradley, W.H.** (1964) Geology of the Green River formation and associated Eocene rocks in southwestern Wyoming and adjacent parts of Colorado and Utah. *USGS Professional Paper 496-A*, 86 pp.
- Bradley, W.H. and Eugster, H.P.** (1969) Geochemistry and paleolimnology of the trona deposits and associated authigenic minerals of the Green River formation of Wyoming. *USGS Professional Paper 496-B*, 71 pp.
- Brenchley, P.J., Pickerill, R.K. and Stromberg, S.G.** (1993) The role of wave reworking on the architecture of storm sandstone facies, Bell Island group (lower Ordovician), eastern Newfoundland. *Sedimentology*, **40**, 359–382.
- Brindley, G.W., Bish, D.L. and Wan, H.M.** (1977) The nature of kerolite, its relation to talc and stevensite. *Mineral. Mag.*, **41**, 443–452.
- Burst, J.F.** (1965) Subaqueously formed shrinkage cracks in clay. *J. Sediment. Res.*, **35**, 348–353.
- Butt, C.R.M.** (1983) Aluminosilicate cementation of saprolites, grits and silcretes in Western Australia. *J. Geol. Soc. Aust.*, **30**, 179–186.
- Bye, J.A.T. and Will, G.D.** (1989) The hydrogeology of the 1974 filling. In: *The Great Filling of Lake Eyre in 1974* (Eds Bonython, C.W. and Fraser, A.S.), pp. 32–43. Royal Geographical Society of Australasia, South Australia Branch, Adelaide.
- Campbell, C.V.** (1967) Lamina, laminaset, bed, bedset. *Sedimentology*, **8**, 7–26.
- Campodonico, V.A., Pasquinia, A.I., Lecomte, K.L., Garc, M.G. and Depetris, P.J.** (2019) Chemical weathering in subtropical basalt-derived laterites: a mass balance interpretation (Misiones, NE Argentina). *Catena*, **173**, 352–366.
- Carroll, A.R.** (2017) Xenoconformities and the stratigraphic record of paleoenvironmental change. *Geology*, **45**, 639–642.
- Carroll, A.R. and Bohacs, K.M.** (1999) Stratigraphic classification of ancient lakes: balancing tectonic and climatic controls. *Geology*, **27**, 99–102.
- Cloud, P.E.** (1968) Atmospheric and hydrospheric evolution on the primitive earth. *Science*, **160**, 729–736.
- Cohen, A.S.** (2003) *Paleolimnology: The History and Evolution of Lake Systems*, p. 528. Oxford University Press, Oxford.
- Colman, S.M.** (1982) Chemical weathering of basalts and andesites: Evidence from weathering rinds. *USGS Professional Paper 1246*, 51 pp.
- Cousin, A., Sautter, V., Payré, V., Forni, O., Mangold, N., Gasnault, O., Le Deit, L., Johnson, J., Maurice, S., Salvatore, M., Wiens, R.C., Gasda, P. and Rapin, W.** (2017) Classification of igneous rocks analyzed by ChemCam at Gale crater, Mars. *Icarus*, **288**, 265–283.
- Cross, W., Iddings, J.P., Pirsson, L.V. and Washington, H.S.** (1902) A quantitative chemico-mineralogical classification and nomenclature of igneous rocks. *J. Geol.*, **10**, 555–690.
- Davis, K., Herman, J., Maksymuk, M., Wilson, J., Chu, P., Burke, K., Jandura, L. and Brown, K.** (2012) Mars Science Laboratory's Dust Removal Tool. 41st Aerospace Mechanisms Symposium, Pasadena, CA, May 16–18, 2012. NASA Conf. Proc. NASA/CP-2012-217653, pp. 279–292.
- Day, M. and Kocurek, G.** (2016) Observation of an aeolian landscape: from surface to orbit in Gale crater. *Icarus*, **280**, 37–71.
- Edgar, L.A., Gupta, S., Rubin, D.M., Lewis, K.W., Kocurek, G.A., Anderson, R.B., Bell, J.F., III, Dromart, G., Edgett, K.S., Grotzinger, J.P., Hardgrove, G., Kah, L.C., Leveille, R., Malin, M.C., Mangold, N., Milliken, R.E., Minitti, M., Palucis, M., Palucis, M., Rowland, S.K., Schieber, J., Stack, K.M., Sumner, D.Y., Wiens, R.C., Williams, R.M.E. and Williams, A.J.** (2018) Shaler: *in situ* analysis of a fluvial sedimentary deposit on Mars. *Sedimentology*, **65**, 96–122.

- Ehlmann, B.L. and Edwards, C.S.** (2014) Mineralogy of the Martian surface. *Annu. Rev. Earth Planet. Sci.*, **42**, 291–315.
- Eugster, H. and Hardie, L.A.** (1978) Saline lakes. In: *Lakes: Chemistry, Geology, Physics* (Ed Lerman, A.), pp. 237–293. Springer-Verlag, New York.
- Ewing, R.C., Lapotre, M.G.A., Lewis, K.W., Day, M., Stein, N., Rubin, D.M., Sullivan, R., Banham, S., Lamb, M.P., Bridges, N.T., Gupta, S. and Fischer, W.W.** (2017) Sedimentary processes of the Bagnold dunes: implications for the eolian rock record of Mars. *J. Geophys. Res. Planets*, **122**, 2544–2573.
- Fedo, C.M., Grotzinger, J.P., Gupta, S., Fraeman, A., Edgar, L., Edgett, K., Stein, N., Rivera-Hernandez, F., Lewis, K., Stack, K.M., House, C., Rubin, D. and Vasavada, A.R.** (2018) Sedimentology and stratigraphy of the Murray formation, Gale crater, Mars. 49th Lunar and Planetary Science Conference, The Woodlands, Texas, USA, March 19–23, 2018, Abstract No. 2078.
- Folk, R.L.** (1980) *Petrology of Sedimentary Rocks*, p. 170. Hemphill publishing company, Austin.
- Fraser, G.S. and Hester, N.C.** (1977) Sediments and sedimentary structures of a beach-ridge complex, southwestern shore of Lake Michigan. *J. Sed. Petrol.*, **47**, 1187–1200.
- Gellert, R., Clark, B.C., III and MSL and MER Science Teams** (2015) In situ compositional measurements of rocks and soils with the alpha particle x-ray spectrometer on NASA's Mars rovers. *Elements*, **11**, 39–44.
- Giampouras, M., Garrido, C.J., Bach, W., Los, C., Fussmann, D., Monien, P. and García-Ruiz, J.M.** (2020) On the controls of mineral assemblages and textures in alkaline springs, Samail ophiolite, Oman. *Chem. Geol.*, **533**, 119435.
- Gierlowski-Kordesch, E. and Kelts, K.** (1994) *Global Geological Record of Lake Basins*, p. 427. Cambridge University Press, Cambridge.
- Gierlowski-Kordesch, E. and Kelts, K.** (2000) Lake basins through space and time. *AAPG Stud. Geol.*, **46**, 648.
- Grant, J.A., Wilson, S.A., Mangold, N., Calef, F., III and Grotzinger, J.P.** (2014) The timing of alluvial activity in Gale crater. *Mars. Geophys. Res. Lett.*, **41**, 1142–1149.
- Grotzinger, J.P., Gupta, S., Malin, M.C., Rubin, D.M., Schieber, J., Siebach, K., Sumner, D.Y., Stack, K.M., Vasavada, A.R., Arvidson, R.E., Calef, F., III, Edgar, L., Fischer, W.F., Grant, J.A., Griffes, J., Kah, L.C., Lamb, M.P., Lewis, K.W., Mangold, N., Miniti, M.E., Palucis, M., Rice, M., Williams, R.M.E., Yingst, R.A., Blake, D., Blaney, D., Conrad, P., Crisp, J., Dietrich, W.E., Dromart, G., Edgett, K.S., Ewing, R.C., Gellert, R., Hurowitz, J.A., Kocurek, G., Mahaffy, P., McBride, M.J., McLennan, S.M., Mischna, M., Ming, D., Milliken, R., Newsom, H., Oehler, D., Parker, T.J., Vaniman, D., Wiens, R.C. and Wilson, S.A.** (2015) Deposition, exhumation, and paleoclimate of an ancient lake deposit, Gale crater, Mars. *Science*, **350**, aac7575.
- Hardie, L.A.** (1968) The origin of the recent non-marine evaporite deposit of Saline Valley, Inyo County, California. *Geochim. Cosmochim. Acta*, **32**, 1279–1301.
- Huang, L.-F. and Rondinelli, J.M.** (2019) Reliable electrochemical phase diagrams of magnetic transition metals and related compounds from high throughput ab initio calculations. *Npj Mater. Degrad.*, **3**, 26.
- Hurowitz, J.A. and McLennan, S.M.** (2007) A ~ 3.5 Ga record of water-limited, acidic weathering conditions on Mars. *Earth Planet. Sci. Lett.*, **260**, 432–443.
- Hurowitz, J.A., Grotzinger, J.P., Fischer, W.W., McLennan, S.M., Milliken, R.E., Stein, N., Vasavada, A.R., Blake, D.F., Dehouck, E., Eigenbrode, J.L., Fairén, A.G., Frydenvang, J., Gellert, R., Grant, J.A., Gupta, S., Herkenhoff, K.E., Ming, D.W., Rampe, E.B., Schmidt, M.E., Siebach, K.L., Stack-Morgan, K., Sumner, D.Y. and Wiens, R.C.** (2017) Redox stratification of an ancient lake in Gale crater, Mars. *Science*, **356**, eaah6849.
- Jagniecki, E.A., Jenkins, D.M., Lowenstein, T.K. and Carroll, A.R.** (2013) Experimental study of shortite ($\text{Na}_2\text{Ca}_2(\text{CO}_3)_3$) formation and application to the burial history of the Wilkins Peak Member, Green River Basin, Wyoming, USA. *Geochimica et Cosmochimica Acta*, **115**, 31–45.
- Kah, L.C., Stack, K.M., Eigenbrode, J.L., Yingst, R.A. and Edgett, K.S.** (2018) Syndepositional precipitation of calcium sulfate in gale crater, Mars. *Terra Nova*, **30**, 431–439.
- Kelts, K. and Hsü, K.J.** (1978) Freshwater carbonate sedimentation. In: *Lakes: Chemistry, Geology, Physics* (Ed Lerman, A.), pp. 295–323. Springer-Verlag, New York.
- Kurokawa, H., Kurosawa, K. and Usui, T.** (2018) A lower limit of atmospheric pressure on early Mars inferred from nitrogen and argon isotopic compositions. *Icarus*, **299**, 443–459.
- Lapotre, M.G.A., Ewing, R.C., Lamb, M.P., Fischer, W.W., Grotzinger, J.P., Rubin, D.M., Lewis, K.W., Ballard, M.J., Day, M., Gupta, S., Banham, S.G., Bridges, N.T., Des Marais, D.J., Fraeman, A.A., Grant, J.A., Herkenhoff, K.E., Ming, D.W., Mischna, M.A., Rice, M.S., Sumner, D.Y., Vasavada, A.R. and Yingst, R.A.** (2016) Large wind ripples on Mars: a record of atmospheric evolution. *Science*, **353**, 55–58.
- Last, W.M. and Schweyen, T.H.** (1985) Sedimentology and geochemistry of saline lakes of the Great Plains. *Hydrobiologia*, **105**, 245–263.
- Lazar, O.R., Bohacs, K.M., Macquaker, J.H.S., Schieber, J. and Demko, T.M.** (2015) Capturing key attributes of fine-grained sedimentary rocks in outcrops, cores, and thin sections: nomenclature and description guidelines. *J. Sed. Res.*, **85**, 230–246.
- Le Deit, L., Hauber, E., Fueten, F., Pondrelli, M., Pio Rossi, A. and Jaumann, R.** (2013) Sequence of infilling events in Gale crater, Mars: results from morphology, stratigraphy, and mineralogy. *J. Geophys. Res.-Planets*, **118**, 2439–2473.
- Li, Z. and Schieber, J.** (2018) Composite particles in mudstones: examples from the late cretaceous Tununk shale member of the Mancos shale formation. *J. Sed. Res.*, **88**, 1319–1344.
- Li, Z., Schieber, J. and Pedersen, P.K.** (2021) On the origin and significance of composite particles in mudstones: examples from the Cenomanian Dunvegan formation. *Sedimentology*, **68**, 737–754.
- Logan, B.W.** (1987) The MacLeod Evaporite Basin, Western Australia: holocene sediments and geological evolution. *AAPG Mem.*, **44**, 140 pp.
- Lowe, D.R., Bishop, J.L., Loizeau, D., Wray, J.J. and Beyer, R.A.** (2020) Deposition of >3.7 Ga clay-rich strata of the Mawrth Vallis group, Mars, in lacustrine, alluvial, and aeolian environments. *Geol. Soc. Am. Bull.*, **132**, 17–30.

- Lu, Z., Chang, Y., Yin, Q., Ng, C. and Jackson, W.** (2014) Evidence for direct molecular oxygen production in CO₂ photodissociation. *Science*, **346**, 61–64.
- Malin, M.C. and Edgett, K.S.** (2000) Sedimentary rocks of early Mars. *Science*, **290**, 1927–1937.
- Martin, P.E., Farley, K.A., Baker, M.B., Malespin, C.A., Schwenzer, S.P., Cohen, B.A. and Navarro-González, R.** (2017) A two-step K-Ar experiment on Mars: dating the diagenetic formation of jarosite from Amazonian groundwaters. *J. Geophys. Res. Planets*, **122**, 2803–2818.
- Maurice, S., Clegg, S.M., Wiens, R.C., Gasnault, O., Rapin, W., Forni, O., Cousin, A., Sautter, V., Mangold, N., Le Deit, L., Nachon, M., Anderson, R.B., Lanza, N.L., Fabre, C., Payré, V., Lasue, J., Meslin, P.-Y., Léveillé, R.J., Barracough, B.L., Beck, P., Bender, S.C., Berger, G., Bridges, J.C., Bridges, N.T., Dromart, G., Dyar, M.D., Francis, R., Frydenvang, J., Gondet, B., Ehlmann, B.L., Herkenhoff, K.E., Johnson, J.R., Langevin, Y., Madsen, M.B., Melikechi, N., Lacour, J.-L., Le Mouélic, S., Lewin, E., Newsom, H.E., Ollila, A.M., Pinet, P., Schröder, S., Sirven, J.-B., Tokar, R.L., Toplis, M.J., d'Uston, C., Vaniman, D.T. and Vasavada, A.R.** (2016) ChemCam activities and discoveries during the nominal mission of the Mars Science Laboratory in Gale crater, Mars. *J. Anal. Atomic Spect.*, **31**, 863–889.
- Maurice, S., Wiens, R.C., Saccoccia, M., Barracough, B., Gasnault, O., Forni, O., Mangold, N., Baratoux, D., Bender, S., Berger, G., Bernardin, J., Berthé, M., Bridges, N., Blaney, D., Bouyé, M., Caïs, P., Clark, B., Clegg, S., Cousin, A., Cremer, D., Cros, A., DeFlores, L., Derycke, C., Dingler, B., Dromart, G., Dubois, B., Dupieux, M., Durand, E., d'Uston, L., Fabre, C., Faure, B., Gaboriaud, A., Gharsa, T., Herkenhoff, K., Kan, E., Kirkland, L., Kouach, D., Lacour, J.-L., Langevin, Y., Lasue, J., Le Mouélic, S., Lescure, M., Lewin, E., Limonadi, D., Manhes, G., Mauchien, P., McKay, C., Meslin, P.-Y., Michel, Y., Miller, E., Newsom, H.E., Ortner, G., Paillet, A., Parès, L., Parot, Y., Pérez, R., Pinet, P., Poitrasson, F., Quertier, B., Sallé, B., Sotin, C., Sautter, V., Séran, H., Simmonds, J.J., Sirven, J.-B., Stiglich, R., Striebig, N., Thocaven, J.-J., Toplis, M.J. and Vaniman, D.** (2012) The ChemCam instrument suite on the Mars science laboratory (MSL) rover: science objectives and mast unit description. *Space Sci. Rev.*, **170**, 95–166.
- McSween, H.Y., Ruff, S.W., Morris, R.V., Bell, J.F., Herkenhoff, K., Gellert, R., Stockstill, K.R., Tornabene, L.L., Squyres, S.W., Crisp, J.A. and Christensen, P.R.** (2006a) Alkaline volcanic rocks from the Columbia Hills, Gusev crater, Mars. *J. Geophys. Res. Planets*, **111**, E9.
- McSween, H.Y., Wyatt, M.B., Gellert, R., Bell, J.F., Morris, R.V., Herkenhoff, K.E., Crumpler, L.S., Milam, K.A., Stockstill, K.R., Tornabene, L.L. and Arvidson, R.E.** (2006b) Characterization and petrologic interpretation of olivine-rich basalts at Gusev crater, Mars. *J. Geophys. Res. Planets*, **111**, E02S10.
- Mees, F., Casteneda, C., Herrero, J. and van Ranst, E.** (2012) The nature and significance of variations in gypsum crystal morphology in dry lake basins. *J. Sed. Res.*, **82**, 37–52.
- Meslin, P.Y., Gasnault, O., Forni, O., Schröder, S., Cousin, A., Berger, G., Clegg, S.M., Lasue, J., Maurice, S., Sautter, V., Le Mouélic, S., Wiens, R.C., Fabre, C., Goetz, W., Bish, D., Mangold, N., Ehlmann, B., Lanza, N., Harri, A.-M., Anderson, R., Rampe, E., McConnochie, T.H., Pinet, P., Blaney, D., Léveillé, R., Archer, D., Barracough, B., Bender, S., Blake, D., Blank, J.G., Bridges, N., Clark, B.C., DeFlores, L., Delapp, D., Dromart, G., Dyar, M.D., Fisk, M., Gondet, B., Grotzinger, J., Herkenhoff, K., Johnson, J., Lacour, J.-L., Langevin, Y., Leshin, L., Lewin, E., Madsen, M.B., Melikechi, N., Mezzacappa, A., Mischna, M.A., Moores, J.E., Newsom, H., Ollila, A., Perez, R., Renno, N., Sirven, J.-B., Tokar, R., de la Torre, M., d'Uston, L., Vaniman, D., Yingst, A. and MSL Science Team** (2013) Soil diversity and hydration as observed by ChemCam at Gale crater, Mars. *Science*, **341**, 1238670.
- Middleton, G.V. and Southard, J.B.** (1984) Mechanics of sediment movement. *SEPM Short Course Notes*, **3**, 142 pp.
- Miller, M.F. and Labandeira, C.C.** (2002) Slow crawl across the salinity divide: delayed colonization of freshwater ecosystems by invertebrates. *GSA Today*, **12**, 4–10.
- Milliken, R.E., Grotzinger, J.P. and Thomson, B.J.** (2010) Paleoclimate of Mars as captured by the stratigraphic record in Gale crater. *Geophys. Res. Lett.*, **37**, L04201.
- Ming, D.W., Mittlefehldt, D.W., Morris, R.V., Golden, D.C., Gellert, R., Yen, A., Clark, B.C., Squyres, S.W., Farrand, W.H., Ruff, S.W., Arvidson, R.E., Klingelhöfer, G., McSweeney, H.Y., Rodionov, D.S., Schröder, C., de Souza, P.A., Jr. and Wang, A.** (2006) Geochemical and mineralogical indicators for aqueous processes in the Columbia Hills of Gusev crater, Mars. *J. Geophys. Res. Planets*, **111**, E02S12.
- Miniti, M.E., Malin, M.C., Van Beek, J.K., Caplinger, M., Maki, J.N., Ravine, M., Calef, F.J., III, Edgar, L.A., Harker, D., Herkenhoff, K.E., Kah, L.C., Kennedy, M.R., Krezowski, G.M., Kronyak, R.E., Lipkaman, L., Nixon, B., Rowland, S.K., Schieber, J., Schroeder, J.F., Stack, K.M., Williams, R.M.E. and Yingst, R.A.** (2019) Distribution of primary and secondary features in the Pahrump Hills outcrop (Gale crater, Mars) as seen in a Mars descent imager (MARDI) "sidewalk" mosaic. *Icarus*, **328**, 194–209.
- Mitchum, R.M. Jr and Vail, P.R.** (1977) Seismic stratigraphy and global changes of sea level, part 7: seismic stratigraphic interpretation procedure. In: *Seismic Stratigraphy – Applications to Hydrocarbon Exploration* (Ed. Payton, C.E.). *AAPG Mem.*, **26**, 135–143.
- Müller, R., Nyström, J.P. and Wright, V.P.** (2004) Pedogenic mud aggregates and paleosol development in ancient dryland river systems: criteria for interpreting alluvial mudrock origin and floodplain dynamics. *J. Sed. Res.*, **74**, 537–551.
- Müller, G. and Irion, G.** (1969) "salt biscuits" – a special growth structure of NaCl in salt sediments of the Tuz Golu ("salt Lake"), Turkey. *J. Sed. Res.*, **39**, 1604–1607.
- Nanson, G.C., Rust, B.R. and Taylor, G.** (1986) Coexistent mud braids and anastomosing channels in an arid-zone river: Cooper Creek, Central Australia. *Geology*, **14**, 175–178.
- Oppenheimer, C., Fischer, T. and Scaillet, B.** (2014) Volcanic degassing: process and impact, chapter 4.4. In: *Treatise on Geochemistry* (Ed Rudnick, R.L.), 2nd edn, pp. 111–179. Elsevier, Amsterdam.
- Pain, C.F., Clarke, J.D.A. and Thomas, M.** (2007) Inversion of relief on Mars. *Icarus*, **190**, 478–491.
- Palucis, M.C., Dietrich, W.E., Hayes, A.G., Williams, R.M.E., Gupta, S., Mangold, N., Newsom, H., Hardgrove, C., Calef, F., III and Sumner, D.Y.** (2014) The origin and evolution of the Peace Vallis fan system that drains to the Curiosity landing area, Gale crater, Mars. *J. Geophys. Res. Planets*, **119**, 705–728.
- Parfitt, R.L. and Kimble, J.M.** (1989) Conditions for formation of allophane in soils. *Soil Sci. Soc. Am. J.*, **53**, 971–977.

- Phillips, R.J., Zuber, M.T., Solomon, S.C., Golombek, M.P., Jakosky, B.M., Banerdt, W.B., Smith, D.E., Williams, R.M.E., Hyena, B.M., Aharonson, O. and Hauck, S.A., II** (2001) Ancient geodynamics and global-scale hydrology on Mars. *Science*, **291**, 2587–2591.
- Pietras, J.T., Carroll, A.R. and Rhodes, M.K.** (2003) Lake basin response to tectonic drainage diversion: Eocene Green River formation, Wyoming. *J. Paleolimnol.*, **30**, 115–125.
- Plummer, P. and Gostin, V.A.** (1981) Shrinkage cracks: desiccation or synaeresis? *J. Sediment. Res.*, **51**, 1147–1156.
- Potter, P.E., Maynard, J.B. and Pryor, W.A.** (1980) *Sedimentology of Shale: Study Guide and Reference Source*, p. 310. Springer-Verlag, New York.
- Raiswell, R.** (1971) The growth of Cambrian and Liassic concretions. *Sedimentology*, **17**, 147–171.
- Rampe, E.B., Blake, D.F., Bristow, T.F., Ming, D.W., Vaniman, D.T., Morris, R.V., Achilles, C.N., Chipera, S.J., Morrison, S.M., Tu, V.M., Yen, A.S., Castle, N., Downs, G.W., Downs, R.T., Grotzinger, J.P., Hazen, R.M., Treiman, A.H., Peretyazhko, T.S., Des Marais, D.J., Walroth, R.C., Craig, P.I., Crisp, J.A., Lafuente, B., Morookian, J.M., Sarrazin, P.C., Thorpe, M.T., Bridges, J.C., Edgar, L.A., Fedo, C.M., Freissinet, C., Gellert, R., Mahaffy, P.R., Newsom, H.E., Johnson, J.R., Kah, L.C., Siebach, K.L., Schieber, J., Sun, V.Z., Vasavada, A.R., Wellington, D., Wiens, R.C. and The MSL Science Team** (2020) Mineralogy and geochemistry of sedimentary rocks and eolian sediments in Gale crater, Mars: a review after six earth years of exploration with Curiosity. *Geochemistry*, **80**, 125605.
- Rampe, E.B., Kraft, M.D., Sharp, T.G., Golden, D.C., Ming, D.W. and Christensen, P.R.** (2012) Allophane detection on Mars with thermal emission spectrometer data and implications for regional-scale chemical weathering processes. *Geology*, **40**, 995–998.
- Rampe, E.B., Ming, D.W., Blake, D.F., Bristow, T.F., Chipera, S.J., Grotzinger, J.P., Morris, R.V., Morrison, S.M., Vaniman, D.T., Yen, A.S., Achilles, C.N., Craig, P.I., Des Marais, D.J., Downs, R.T., Farmer, J.D., Fendrich, K.V., Gellert, R., Hazen, R.M., Kah, L.C., Morookian, J.M., Peretyazhko, T.S., Sarrazin, P., Treiman, A.H., Berger, J.A., Eigenbrode, J., Fairén, A.G., Forni, O., Gupta, S., Hurowitz, J.A., Lanza, N.L., Schmidt, M.E., Siebach, K., Sutter, B. and Thompson, L.M.** (2017) Mineralogical trends in mudstone deposits from the Murray formation, Gale crater, Mars. *Earth Planet. Sci. Lett.*, **471**, 172–185.
- Renaut, R.W. and Gierlowski-Kordesch, E.H.** (2010). Lakes. In: *Facies Models 4* (Eds James, N.P. and Dalrymple, R.W.). *Geological Association of Canada, GEOText*, **6**, 541–575.
- Rosen, M.R.** (1994) The importance of groundwater in playas: a review of playa classifications and the sedimentology and hydrology of playas. In: *Paleoclimate and Basin Evolution of Playa Systems* (Ed. Rosen, M.R.), *Geol. Soc. Am. Spec. Paper*, **289**, 1–18.
- Rubin, D.M.** (1987) Cross-bedding, bedforms, and paleocurrents. *SEPM Concepts in Sedimentology and Paleontology*, **1**, 187 pp.
- Rust, B.R. and Nanson, G.C.** (1989) Bedload transport of mud as pedogenic aggregates in modern and ancient rivers. *Sedimentology*, **36**, 291–306.
- Scheller, E.L., Swindle, C., Grotzinger, J., Barnhart, H., Bhattacharjee, S., Ehlmann, B.L. and Smith, B.P.** (2021) Formation of magnesium carbonates on Earth and implications for Mars. *J. Geophys. Res. Planets*, **126**, e2021JE006828.
- Schieber, J.** (2011) Reverse engineering mother nature—shale sedimentology from an experimental perspective. *Sediment. Geol.*, **238**, 1–22.
- Schieber, J.** (2016) Experimental testing of the transport-durability of shale lithics and its implications for interpreting the rock record. *Sediment. Geol.*, **331**, 162–169.
- Schieber, J.** (2018) How small is it? Pushing MAHLI to the limit in the search for mudstones at Gale crater, Mars. 49th Lunar and Planetary Science Conference, The Woodlands, Texas, USA, March 19–23, 2018, Abstract No. 1100.
- Schieber, J., Bish, D., Coleman, M., Reed, M., Hausrath, E.M., Cosgrove, J., Gupta, S., Minitti, M.E., Edgett, K.S. and Malin, M.** (2017) Encounters with an unearthly mudstone: understanding the first mudstone found on Mars. *Sedimentology*, **64**, 311–358.
- Schieber, J., Miclaus, C., Seserman, A., Liu, B. and Teng, J.** (2019) When a mudstone was actually a “sand”: results of a sedimentological investigation of the bituminous marl formation (Oligocene), eastern Carpathians of Romania. *Sed. Geol.*, **384**, 12–28.
- Schieber, J., Minitti, M.E., Sullivan, R., Edgett, K.S., Malin, M.C., Parker, T. and Calef, F.** (2020) Engraved on the rocks—Aeolian abrasion of Martian mudstone exposures and their relationship to modern wind patterns in Gale crater, Mars. *Depos. Rec.*, **6**, 625–647.
- Schieber, J. and Shao, X.** (2021) Detecting detrital carbonate in shale successions – Relevance for evaluation of depositional setting and sequence stratigraphic interpretation. *Marine Petrol. Geol.*, **130**, 105130.
- Schieber, J., Southard, J.B. and Schimmelmann, A.** (2010) Lenticular shale fabrics resulting from intermittent erosion of water-rich muds—interpreting the rock record in the light of recent flume experiments. *J. Sed. Res.*, **80**, 119–128.
- Schieber, J., Sumner, D., Bish, D., Stack, K., Minitti, M., Yingst, A., Edgett, K., Malin, M., Grotzinger, J. and MSL Science Team** (2015) The Pahrump succession in Gale Crater—a potential evaporite bearing lacustrine mudstone with resemblance to Earth analogs. 46th Lunar and Planetary Science Conference, Abstract No. 2153.
- Schwenzer, S.P., Abramov, O., Allen, C.C., Bridges, J.C., Clifford, S.M., Filiberto, J., Kring, D.A., Lasue, J., McGovern, P.J., Newsom, H.E., Treiman, A.H., Vaniman, D.T., Wiens, R.C. and Wittmann, A.** (2012) Gale crater: formation and post-impact hydrous environments. *Planet. Space Sci.*, **70**, 84–95.
- Smith, M.E. and Carroll, A.R.** (2015) Stratigraphy and Paleolimnology of the Green River formation, Western USA. *Synth. Limnogeol.*, **1**, Springer, 355 pp.
- Smith, M.E., Carroll, A.R. and Scott, J.J.** (2015) Stratigraphic expression of climate, tectonism, and geomorphic forcing in an underfilled lake basin: Wilkins peak member of the Green River formation. In: *Stratigraphy and Paleolimnology of the Green River Formation, Western USA* (Eds Smith, M.E. and Carroll, A.R.), *Syntheses in Limnogeology*, **1**, 61–102.
- Smoot, J.P. and Lowenstein, T.K.** (1991) Depositional environments of non-marine evaporites. In: *Evaporites, Petroleum, and Mineral Resources* (Ed. Melvin, J.L.), *Developments in Sedimentology*, **50**, 189–347.
- Stack, K.M., Grotzinger, J.P., Lamb, M.P., Gupta, S., Rubin, D.M., Kah, L.C., Edgar, L.A., Fey, D.M., Hurowitz, J.A., McBride, M., Rivera-Hernández, F., Sumner, D.Y., Van Beek, J.K., Williams, R.M.E. and Yingst, R.A.** (2019)

- Evidence for plunging river plume deposits in the Pahrump Hills member of the Murray formation, Gale crater, Mars. *Sedimentology*, **66**, 1768–1802.
- Strother, P.K., Battison, L., Brasier, M.D. and Wellman, C.H.** (2011) Earth's earliest non-marine eukaryotes. *Nature*, **473**, 505–509.
- Tabazadeh, A. and Turco, R.P.** (1993) Stratospheric chlorine injection by volcanic eruptions: HCl scavenging and implications for ozone. *Science*, **260**, 1082–1086.
- Thompson, L.M., Berger, J.A., Spray, J.G., Fraeman, A.A., McCraig, M.A., O'Connell-Cooper, C.D., Schmidt, M.E., VanBommel, S., Gellert, R., Yen, A. and Boyd, N.I.** (2020) APXS-derived compositional characteristics of the Vera Rubin ridge and Murray formation, Gale crater, Mars: geochemical implications for the origin of the ridge. *J. Geophys. Res. Planets*, **125**, e2019JE006319.
- Thomson, B.J., Bridges, N.T., Milliken, R.E., Baldridge, A., Hook, S.J., Crowley, J.K., Marion, G.M., de Souza Filho, C.R., Brown, A.J. and Weitz, C.M.** (2011) Constraints on the origin and evolution of the layered mound in Gale crater, Mars using Mars Reconnaissance Orbiter Data. *Icarus*, **214**, 413–432.
- Thornber, M.R., Bettenay, E. and Russell, W.G.R.** (1987) A mechanism of aluminosilicate cementation to form a hardpan. *Geochim. Cosmochim. Acta*, **51**, 2303–2310.
- Trichet, J.** (1963) Description d'une Forme d'Accumulation de Gypse par Voie Eolienne dans le Sud Tunisien. *Soc. Geol. France Bull.*, **5**, 617–621.
- Trichet, J.** (1967) Etude des Facies d'une Dune Gypseuse, Sud d'Oran, Algérie. *Soc. Geol. France Bull.*, **9**, 865–875.
- Tye, R.S. and Coleman, J.M.** (1989) Depositional processes and stratigraphy of fluvially dominated lacustrine deltas: Mississippi delta plain. *J. Sed. Res.*, **59**, 973–996.
- van Breemen, N. and Buurman, P.** (2002) Dense and cemented horizons: fragipan, duripan, and tepestate. In: *Soil Formation* (Eds van Breemen, N. and Buurman, P.), 2nd edn, pp. 329–344. Springer, Dordrecht.
- Van Wagoner, J.C., Posamentier, H.W., Mitchum, R.M., Vail, P.R., Sarg, J.F., Loutit, T.S. and Hardenbol, J.** (1988) An overview of the fundamentals of sequence stratigraphy and key definitions. In: *Sea-Level Changes: An Integrated Approach* (Eds Wilgus, C.K., Hastings, B.S., Posamentier, H., van Wagoner, J., Ross, C.A. and Kendall, C.G. St. C.), SEPM Spec. Publ., **42**, 39–46.
- VanBommel, S.J., Gellert, R., Berger, J.A., Campbell, J.L., Thompson, L.M., Edgett, K.S., McBride, M.J., Minitti, M.E., Pradler, I. and Boyd, N.I.** (2016) Deconvolution of distinct lithology chemistry through oversampling with the Mars science laboratory alpha particle X-ray spectrometer. *Xray Spectrom.*, **45**, 155–161.
- Vaniman et al.** (2004) Magnesium sulphate salts and the history of water on Mars. *Nature*, **431**, 663–665.
- Wakelin-King, G.A. and Webb, J.A.** (2007) Threshold-dominated fluvial styles in an arid-zone mud-aggregate river: the uplands of Fowlers Creek, Australia. *Geomorphology*, **85**, 114–127.
- Warren, C.J. and Rudolph, D.L.** (1997) Clay minerals in basin of Mexico lacustrine sediments and their influence on ion mobility in groundwater. *J. Contam. Hydrol.*, **27**, 177–198.
- Warren, J.K.** (1985) On the significance of evaporite lamination. In: *6th Symposium on Salt* (Eds Schreiber, B.C. and Hamer, H.C.), pp. 161–170. The Salt Institute, Alexandria, VA.
- Warren, J.K.** (2006) *Evaporites: Sediments, Resources and Hydrocarbons*. Springer-Verlag, Berlin, 1035 pp.
- Weiler, Y., Sass, E. and Zak, I.** (1974) Halite oolites and ripples in the Dead Sea, Israel. *Sedimentology*, **21**, 623–632.
- Weitz, C.M., Bishop, J.L., Baker, L.L. and Berman, D.C.** (2014) Fresh exposures of hydrous Fe-bearing amorphous silicates on Mars. *Geophys. Res. Lett.*, **41**, 8744–8751.
- Wiens, R.C., Maurice, S., Barracough, B., Saccoccia, M., Barkley, W.C., Bell, J.F., III, Bender, S., Bernardin, J., Blaney, D., Blank, J., Bouye, M., Bridges, N., Bultman, N., Cais, P., Clanton, R.C., Clark, B., Clegg, S., Cousin, A., Cremers, D., Cros, A., DeFlores, L., Delapp, D., Dingler, R., D'Uston, C., Dyar, M.D., Elliott, T., Enemark, D., Fabre, C., Flores, M., Forni, O., Gasnault, O., Hale, T., Hays, C., Herkenhoff, K., Kan, E., Kirkland, L., Kouach, D., Landis, D., Langevin, Y., Lanza, N., LaRocca, F., Lasue, J., Latino, J., Limonadi, D., Lindensmith, C., Little, C., Mangold, N., Manhes, G., Mauchien, P., McKay, C., Miller, E., Mooney, J., Morris, R.V., Morrison, L., Nelson, T., Newsom, H., Ollila, A., Ott, M., Pares, L., Perez, R., Poitrasson, F., Provost, C., Reiter, J.W., Roberts, T., Romero, F., Sautter, V., Salazar, S., Simmonds, J.J., Stiglich, R., Storms, S., Striebig, N., Thocaven, J.-J., Trujillo, T., Ulibarri, M., Vaniman, D., Warner, N., Waterbury, R., Whitaker, R., Witt, J. and Wong-Swanson, B.** (2012) The ChemCam instrument suite on the Mars science laboratory (MSL) rover: body unit and combined system tests. *Space Sci. Rev.*, **170**, 167–227.
- Williams, R.M.E., Grotzinger, J.P., Dietrich, W.E., Gupta, S., Sumner, D.Y., Wiens, R.C., Mangold, N., Malin, M.C., Edgett, K.S., Maurice, S., Forni, O., Gasnault, O., Ollila, A., Newsom, H.E., Dromart, G., Palucis, M.C., Yingst, R.A., Anderson, R.B., Herkenhoff, K.E., Le Mouélic, S., Goetz, W., Madsen, M.B., Koefoed, A., Jensen, J.K., Bridges, J.C., Schwenthaler, S.P., Lewis, K.W., Stack, K.M., Rubin, D., Kah, L.C., Bell, J.F., Farmer, J.D., Sullivan, R., Van Beek, T., Blaney, D.L., Pariser, O., Deen, R.G. and MSL Science Team** (2013) Martian fluvial conglomerates at gale crater. *Science*, **340**, 1068–1072.
- Wright, V.P. and Marriott, S.B.** (2007) The dangers of taking mud for granted: lessons from lower old red sandstone dryland river systems of South Wales. *Sed. Geol.*, **195**, 91–100.
- Xiao, L., Huang, J., Christensen, P.R., Greeley, R., Williams, D.A., Zhao, J. and He, Q.** (2012) Ancient volcanism and its implication for thermal evolution of Mars. *Earth Planet. Sci. Lett.*, **323–324**, 9–18.
- Yawar Z., Schieber J., Sullivan R., Minitti M. and Edgett K.** (2019) On the eolian transport durability of sand-size mudstone clasts — the potential for Martian sand dunes that are composed of fine grained aggregates and implications for interpreting mudstone strata at Gale Crater, Mars. 50th Lunar and Planetary Science Conference, The Woodlands, Texas, USA, March 18–22, 2019, Abstract No. 1999.
- Yawar Z., Schieber J., Minitti M., Van Beek, J., Calef, F., Edgett, K. and Malin, M.** (2018) With the Nose to the Ground—Exploring the Pahrump Hills Outcrop with MARDI for New Perspectives on the Mudstones of the Murray Formation at Gale Crater, Mars. 49th Lunar and Planetary Science Conference, The Woodlands, Texas, USA, March 19–23, 2018, Abstract No. 1101.
- Zuffa, G.G.** (1980) Hybrid arenites: their composition and classification. *J. Sediment. Petrol.*, **50**, 21–29.

Manuscript received 10 April 2022; revision accepted 13 June 2022